CONTENT
Vol. 12. No. 4-2026

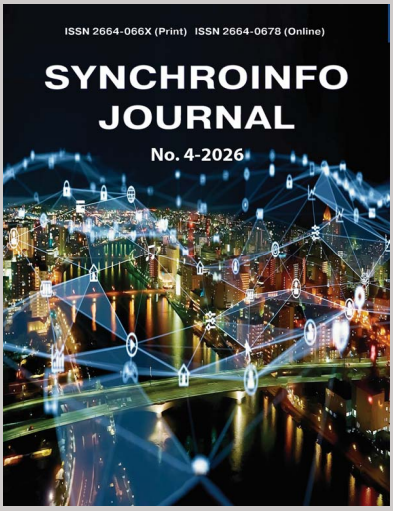
Ali Salah Mahdi Khafaga
VISION-ASSISTED PROACTIVE HANDOVER AND RESOURCE ALLOCATION IN HYBRID LIFI/RF 6G NETWORKS USING EDGE AI **2**

Q. F. Ngo, O. V. Varlamov
OUTPHASING POWER AMPLIFIER EFFICIENCY **19**

Happy Ondobo Steve, Vitaly B. Kreindelin
DEVELOPMENT OF A MACHINE LEARNING ALGORITHM FOR RISK ASSESSMENT IN INTERNET OF THINGS (IOT) SYSTEMS **32**

Sy. D. Vu
INTERACTION BETWEEN DETECTION AND TRACKING UNITS FOR SIGNAL FREQUENCIES AND TIME DELAYS (ILLUSTRATED BY A SATELLITE RADIO SYSTEM) **39**

Angelina Bott
ARTIFICIAL INTELLIGENCE IN THE URBAN ENVIRONMENT: EXAMPLES OF TECHNOLOGY APPLICATIONS. Part I **68**



Published bi-monthly since 2015

ISSN 2664-0678 (Online)
ISSN 2664-066X (Print)

Publisher
Institute of Radio and Information Systems (IRIS), Vienna, Austria

Deputy Editor in Chief

Albert Waal
Dr.-Ing., RF Mondial GmBH, Hannover, Germany

Editorial board

Corbett Rowell
Doctor of Science, Rohde & Schwarz, Munich, Germany

Julius Golovatchev
PhD, INCOTELOGY GmbH, Pulheim, Germany

Oleg V. Varlamov
Doctor of Science, IRIS Association, Vienna, Austria

Svetlana S. Dymkova
PhD, IRIS Association, Vienna, Austria

Michael J. Sharpe
PhD, ETSI/SPR Director Committee Support Centre, European Telecommunications Standards Institute (ETSI), Nice Area, France

Andrey V. Grebennikov
Ph.D., Sumitomo Electric Europe, Elstree, United Kingdom

Eric F. Dulkeith
Doctor of Science, Senior Executive, Detecon Inc., San Francisco, USA

Marcelo S. Alencar
Doctor of Science, Federal University of Campina Grande, Brazil

German Castellanos-Dominguez
Ph.D., National University of Colombia, Manizales, Colombia

Ali H. Harmouch
Doctor of Science, University of Business and Technology, Jeddah, Saudi Arabia

Valery O. Tikhvinskiy
Doctor of Science, International Information Technology University, Almaty, Kazakhstan

Bayram Ibrahimov
Doctor of Science, Azerbaijan Technical University, Baku, Azerbaijan

Kristina Knox
Doctor of Philosophy, PhD at The University of Queensland, Australia

Anastasia Mozhaeva
Doctoral Candidate (Computer Vision) The University of Waikato, Hamilton, New Zealand

Boudal Niang
Doctor of Philosophy, Multinational Graduate School of Telecommunications, Dakar, Senegal

Address:
1170 Wien, Austria, Hernalser Hauptstrasse 49/22
media-publisher.eu/synchroinfo-journal

© Institute of Radio and Information Systems (IRIS), 2026

SYNCHROINFO JOURNAL

www.media-publisher.eu/synchroinfo-journal

VISION-ASSISTED PROACTIVE HANDOVER AND RESOURCE ALLOCATION IN HYBRID LIFI/RF 6G NETWORKS USING EDGE AI

Ali Salah Mahdi Khafaga [1]

[1] Department of Computer Networks and Software, Al-Furat Al-Awsat Technical University, Babil, Iraq; ali.khafaja@atu.edu.iq
https://orcid.org/0000-0001-5792-1511
https://www.scopus.com/authid/detail.uri?authorId=59499331800

ABSTRACT

Light fidelity (LiFi) offers large unlicensed bandwidth for indoor 6G access, but its line-of-sight links are interrupted whenever a person walks between a luminaire and a device, or when the device tilts out of the receiver field of view. Handover schemes in hybrid LiFi/RF networks react only after the link is lost and therefore leave users without service for the detection and execution time of the handover. In this paper, we use the cameras that already monitor many smart buildings to anticipate these outages. An edge-AI pipeline tracks every person, converts the scene geometry into link-level features, fuses them with the measured signal-to-noise ratio, and predicts the probability that each LiFi link becomes unusable within the next second. A deep reinforcement learning agent, pre-trained from demonstrations and fine-tuned online, uses this forecast to select the access point of every user, while proportional-fair time sharing allocates resources inside each cell. In a room with six users and up to fifteen walking pedestrians, the learned vision-radio predictor raises the area under the ROC curve for 200-ms outage prediction from 0.79 (Kalman/Monte-Carlo forecast) to 0.89, and the proposed controller reduces link-interruption time by 42-47% with respect to a standard event-A3 handover, with no loss in mean throughput. Without retraining, the controller also reduces interruption by 53% when the pedestrians follow real trajectories from the ETH/UCY datasets.

KEYWORDS: *LiFi, hybrid LiFi/WiFi networks, handover, blockage prediction, computer vision, edge AI, deep reinforcement learning, 6G*.

DOI: 10.36724/2664-066X-2026-12-4-2-18

Received: 20.04.2026
Accepted: 22.06.2026

Citation: Ali Salah Mahdi Khafaga, "A. Vision-Assisted Proactive Handover and Resource Allocation in Hybrid LiFi/RF 6G Networks Using Edge AI," *Synchroinfo Journal* **2026**, vol. 12, no. 4, pp. 2-18.

Licensee IRIS, Vienna, Austria.

This article is an open access article distributed under the terms and conditions of the Creative Commons Attribution (CC BY) license (https://creativecommons.org/licenses/by/4.0/).

Copyright: © 2026 by the authors.

1 Introduction

LiFi turns ceiling luminaires into access points (APs) and adds hundreds of megahertz of license-free spectrum to indoor networks [1]; the IEEE 802.11bb amendment now standardizes light communications in wireless local area networks [2]. Because each LiFi cell is small and relies on a line-of-sight (LoS) path, practical deployments combine LiFi with a radio-frequency (RF) network such as WiFi in a hybrid LiFi/WiFi network (HLWNet) [3]. In such a network, WiFi guarantees coverage and LiFi carries most of the traffic.

The optical link, however, is fragile. A person who walks between a luminaire and a device blocks the LoS path within tens of milliseconds, the body of the user can block the luminaires behind them, and a natural change of the device tilt can move an AP outside the receiver field of view (FOV) [4]. Conventional handover (HO) schemes in HLWNets, including the LTE-style event-A3 rule and learning-based variants [5-8], decide from radio measurements only. They detect an outage after it has happened and then spend a further HO execution time of hundreds of milliseconds before the user is served again. For latency-sensitive traffic, it is these interruptions, rather than the average rate, that users notice.

A camera, by contrast, can see a blocker approaching before the link is lost. Charan *et al.* showed that cameras at mmWave base stations can predict blockage and trigger a proactive hand-off [9], and later work has extended vision-aided beam and blockage prediction using real-world multi-modal datasets [10-12]. LiFi has been studied as a sensing modality together with cameras [13], but, to the best of our knowledge, vision has not been used to drive handover in hybrid LiFi/RF networks. These mmWave results do not carry over directly to LiFi. In mmWave the obstacle crosses a long, roughly horizontal beam. In LiFi the beam is short and steep, so only people very close to the user can block it; the user's own body is a frequent blocker; and the orientation of a hand-held device matters as much as the position of the people around it.

In this paper we address this gap. Our main contributions are as follows.

- **LiFi-specific vision-to-channel mapping.** We derive the *blocking zone* of a LiFi link, the part of the LoS segment low enough to be cut by a human body, and turn the tracked scene into link-level features: the clearance of every person from this zone now and extrapolated over the next second, self-blockage geometry, and the field-of-view margin implied by the estimated device tilt.
- **Learned bimodal outage predictor.** A lightweight network fuses the vision features with the measured signal-to-noise ratio (SNR) history and outputs, for every user–AP link, a monotone curve of outage probabilities over a 1-s horizon and the expected outage fraction. Training with randomized perception quality makes it robust to detector noise, missed detections and latency.
- **Joint proactive handover and resource allocation.** We formulate access-point selection with proportional-fair (PF) time allocation as a constrained stochastic control problem, show that PF allocation reduces to equal time sharing for a given association, and solve the association with a Double-DQN agent that is pre-trained from an outage-aware expert rule and fine-tuned with reinforcement learning.
- **Reproducible evaluation.** A frame-level simulator with measured orientation statistics, self-blockage, make-before-break handover and real pedestrian trajectories (ETH/UCY [14, 15]) compares the proposal with reactive, event-A3, vision-free DRL, physics-based vision and oracle schemes, and quantifies prediction accuracy, the throughput-reliability trade-off, robustness and complexity.

The rest of the paper is organized as follows. Section 2 reviews related work. Section 3 presents the system model and the problem formulation. Section 4 describes the vision pipeline and the outage predictors, and Section 5 the handover controllers. Section 6 details the evaluation set-up, Section 7 discusses the results, Section 8 the limitations, and Section 9 concludes the paper.

2 Related work

2.1 Handover and Load Balancing in HLWNets

Handover in HLWNets is either horizontal (HHO), between two LiFi APs, or vertical (VHO), between LiFi and WiFi, and both incur signaling overhead that interrupts the service [3]. Wang and Haas combined load balancing with handover to account for this overhead [5]. Learning-based schemes have since been proposed: Frómeta Fonseca *et al.* classify the trajectory type of a user and use Q-learning for the HO decision, improving throughput by 59% over a smart HO baseline [6]; a dueling DQN jointly reduces delay and HO frequency [7]; and a sequential proximal policy optimization method improves sum throughput in user association [8]. Blockage has been handled with diversity receivers and rule-based resource allocation [16]. All of these use radio-side information only, so they cannot anticipate a blockage that has not yet affected the signal.

2.2 Device Orientation in LiFi

Soltani *et al.* measured how people hold their phones and showed that the polar angle follows a Laplace distribution for static users and a Gaussian distribution for walking users, with a significant impact on the LoS channel gain and on handover rate [4]. Existing HO schemes treat orientation as a random variable, whereas a camera can estimate it for each user individually.

2.3 Vision-Aided Wireless Communications

Vision-aided blockage prediction has been demonstrated for mmWave links with bimodal deep learning that combines RGB images and beam power [9], supported by real-world datasets [10]. Recent work reports over 98% accuracy three frames ahead for mmWave blockage [11] and vision-aided mobility management for terahertz links [12]. Camera, LiFi and RF data have also been fused for indoor sensing [13]. Our work differs in three ways: it targets the steep, short LiFi geometry including self-blockage and tilt; it predicts a probability *curve* over the horizon instead of a binary label; and it closes the loop with a controller that explicitly trades interruption against throughput in a multi-user hybrid network.

3 System model and problem formulation

3.1 Network and Geometry

We consider an indoor room of size L x W x H served by a set $A = \{1,\ldots,A\}$ of ceiling LiFi APs and one WiFi AP, indexed by 0 (Fig. 1). Neighbouring LiFi APs use orthogonal bands, so inter-cell interference is neglected. A set of users carries hand-held devices; a further set of non-connected pedestrians moves in the room. Time is slotted with the camera frame period $\Delta = 1/30^{o}$s, and decisions are taken every $D_s = 2$ frames.

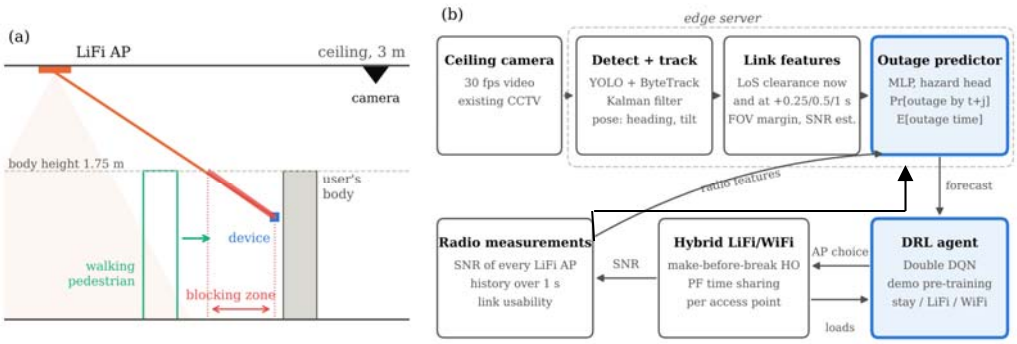


Fig. 1. (a) Side view of a LiFi link: only the segment of the LoS path lower than the body height (the blocking zone) can be cut by a person, so the relevant blockers are the user's own body and people within about a metre of the device. (b) Edge-AI pipeline: tracked people are turned into link features, fused with radio measurements, and the predicted outage curve drives the DRL handover agent.

Each person is modelled as a vertical cylinder of radius r_b and height h_b. User u stands at ground position $\mathbf{p}_u(t)$ facing direction $\phi_u(t)$ and holds the device at height hd, a distance δ in front of the body, i.e. $\mathbf{d}_u(t) = \mathbf{p}_u(t) + \delta\,[\cos\phi_u, \sin\phi_u]^T$.

3.2 LiFi Channel

The LoS channel gain between AP a at height H and the device of user u is [17]

$$G_{u,a} = \frac{(m+1)A_{\mathrm{PD}}}{2\pi d_{u,a}^2}\ \cos^m(\varphi_{u,a})\,T_s\,g(\psi_{u,a})\cos(\psi_{u,a}),\quad 0 \le \psi_{u,a} \le \Psi_c, \tag{1}$$

And $G_{u,a} = 0$ otherwise, where $m = -\ln 2/\ln(\cos\Phi_{1/2})$ is the Lambertian order, A_{PD} the photodiode area, $d_{u,a}$ the distance, $\varphi_{u,a}$ the irradiance angle, Ts the filter gain, $g(\Psi) = n^2_c/\sin^2\Psi_c$ the concentrator gain and Ψ_c the FOV. The incidence angle follows from the device normal

$$\cos\psi_{u,a} = \frac{\mathbf{n}_u^T(\mathbf{x}_a - \mathbf{x}_u)}{\|\,\mathbf{x}_a - \mathbf{x}_u\,\|},\qquad \mathbf{n}_u = \begin{bmatrix}\sin\theta_u\cos\omega_u\\ \sin\theta_u\sin\omega_u\\ \cos\theta_u\end{bmatrix}, \tag{2}$$

where x denotes 3-D positions, θ_u is the polar tilt and $\omega_u = \phi_u + \pi$ because the screen faces the user. Following the measurements in [4], θ_u is a Gaussian process with mean 29.67° and standard deviation 7.78° while walking (41.39°, 7.68° while static) and an AR(1) correlation with coherence time τ_θ.

The electrical SNR and the achievable rate of DC-biased optical OFDM are [18]

$$\gamma_{u,a} = \frac{\left(\kappa P_{\mathrm{opt}} G_{u,a}\right)^2}{N_0 B_{\mathrm{L}}},\qquad R_{u,a} = \frac{B_{\mathrm{L}}}{2}\log_2\left(1 + \frac{e}{2\pi}\gamma_{u,a}\right), \tag{3}$$

where k is the PD responsivity, P_{opt} the optical power, N_0 the noise power spectral density and B_L the LiFi bandwidth. A link is usable when it is not blocked and $10\log_{10}\gamma_{u,a} \geq \gamma_{\min}$.

3.3 Blocking Zone and Self-Blockage

Let s_a and e_u be the ground projections of AP a and device u. Along the LoS segment the height decreases linearly from H to h_d, so a body of height h_b can only intersect the fraction

$$s \in [s_0, 1], \qquad s_0 = \frac{H - h_b}{H - h_d}, \tag{4}$$

of the segment closest to the device. With H = 3°m, h_b = 1,75°m and h_d = 1,2 °m, s_0 = 0,69: only the last 31% of the horizontal projection, typically less than one metre, can be blocked. Link (u, a) is blocked at time t if any person k, including user u itself, satisfies

$$\beta_{u,a}(t) = \mathbb{1}\left\{\min_k \operatorname{dist}(\mathbf{c}_k(t), [\mathbf{s}_a + s_0(\mathbf{e}_u - \mathbf{s}_a), \mathbf{e}_u]) < r_b\right\}, \tag{5}$$

where c_k is the body centre and *dist* the point-to-segment distance. Including $k = u$ captures self-blockage of the APs behind the user. Equation (4) is the main geometric difference from mmWave blockage, where the beam is long and nearly horizontal.

3.4 WiFi Channel

The WiFi AP uses bandwidth B_R at 2.4 GHz with the IEEE 802.11 TGn path-loss model (breakpoint 5 m) [19]. Its single-user throughput is $R_{u,0} = \eta B_R \min\{\log_2(1 + \gamma_u^{RF}), c_{\max}\}$, where $c_{\max}$ caps the spectral efficiency at the highest modulation and coding scheme and η accounts for MAC overhead.

3.5 Handover and Resource Allocation

Let $x_{u,a}(t) \in \{0,1\}$ indicate that user u is associated with AP $a \in \{0\} \cup \mathcal{A}$, and $\tau_{u,a}(t) \in [0,1]$ the fraction of time AP a serves user u. A HO from a to a' takes T_{HHO} if both are LiFi APs and T_{VHO} otherwise. We assume make-before-break execution: the old link keeps serving the user until the HO completes, so a HO started early enough causes no interruption. If the serving LiFi link is lost, every scheme falls back to a reactive HO after a detection delay of T_{det}.¶

For a given association, the time allocation inside each cell maximizes the PF utility.¶

Lemma 1: For AP a serving the set $\mathcal{U}_a(t)$ of users with usable links, $\max_\tau \sum_{u \in \mathcal{U}_a} \log(\tau_{u,a} R_{u,a})$ subject to $\sum_u \tau_{u,a} \le 1$ is solved by $\tau^\star_{u,a} = 1/|\mathcal{U}_a(t)|$.¶

Proof: The objective equals $\sum_u \log \tau_{u,a} + \sum_u \log R_{u,a}$; the second term does not depend on τ, and maximizing $\sum_u \log \tau_{u,a}$ on the simplex gives equal shares by symmetry and concavity (KKT).¶

The rate of user u is then $r_u(t) = \sum_a x_{u,a}(t)\, R_{u,a}(t)/|\mathcal{U}_a(t)|$, and resource allocation is coupled to association through the loads $|\mathcal{U}_a|$.¶

3.6 Problem Formulation

We define the link-interruption indicator $\rho_u(t) = \mathbb{1}\{r_u(t) = 0\}$, which is one while the serving LiFi link is unusable and the user has not yet been handed over. The joint handover and resource-allocation problem is

$$\begin{aligned} \text{P1:} \max_{\{x(t)\}} \quad & \mathbb{E}\left[\sum_{t}\sum_{u\in\mathcal{U}}\left(\frac{r_u(t)}{R_{\text{ref}}} - \lambda\, o_u(t) - c_{\text{HO}}\, h_u(t)\right)\right] \\ \text{s.t.} \quad & \sum_{a} x_{u,a}(t) = 1, \quad x_{u,a}(t) \in \{0,1\}, \\ & \tau_{u,a}(t) = \tau^{*}_{u,a}(t) \text{ (Lemma 1)}, \\ & \text{HO execution constraints with } T_{\text{HHO}}, T_{\text{VHO}}, \end{aligned} \tag{6}$$

where $h_u(t)$ indicates a HO started by user u at time t, R_{ref} = 100 Mb/s normalizes throughput, and γ sets the cost of one unit of interruption time relative to throughput. P1 is a mixed-integer stochastic control problem whose state includes the future motion of every person in the room. It cannot be solved by per-slot optimization because the effect of a decision appears only after the HO execution time. We therefore (i) forecast link outages from vision and radio data (Section 4) and (ii) solve P1 as a Markov decision process (Section 5).

4 Vision-assisted outage prediction

4.1 Edge Perception

A ceiling camera feeds an edge server running a person detector [20] and a multi-object tracker [21]. Detections are projected to the floor plane through a calibrated homography, and pose keypoints give the facing direction of every person and the arm/hand pose of each user, from which the device tilt is estimated. In this study, the pipeline is modelled at the level of its outputs: floor positions with Gaussian error σ_p, independent missed detections with probability p_{miss}, a processing latency of L_v frames, heading error 10° and tilt error 5°. We assume that track identities are maintained and that the network knows which tracked person carries which device, for example from LiFi uplink positioning. All three perception parameters are swept in Section 7.

Each person is tracked with a constant-velocity Kalman filter with state $\mathbf{z}_k = [\mathbf{c}_k^T, \dot{\mathbf{c}}_k^T]^T$, transition $\mathbf{z}_k(t+1) = \mathbf{F}\mathbf{z}_k(t) + \mathbf{w}_k$ and process noise driven by a random acceleration of standard deviation σ_a. The filter output is propagated over the latency L_v to the current time.

4.2 Physics-Based Monte-Carlo Forecast

As a model-based reference, we draw K samples from the Kalman posterior of every person and of the device tilt, propagate them over the horizon J decision steps with the motion model, and evaluate (1)-(5) for every sample. The forecast for link (u,a) is

$$\hat{P}_{u,a}(j) = \frac{1}{K}\sum_{k=1}^{K} \mathbb{1}\left\{\exists\, i \le j:\ \bar{v}_{u,a}^{(k)}(i) = 1\right\}, \tag{7}$$

where $\bar{v}_{u,a}^{(k)}(i)$ indicates that the link is unusable in sample k at step i. This is the probability that the link fails at least once within j steps, together with the expected outage fraction $\hat{\eta}_{u,a}$ over the horizon. A deterministic variant uses the posterior mean only.

4.3 Learned Bimodal Predictor

In practice, the Monte-Carlo forecast is only as good as its motion model. Real people stop, turn and sway in ways that a constant-velocity model cannot capture, and the tilt process is only partly predictable. We therefore learn the outage curve directly. For every link and decision step, the input vector concatenates

- *vision features*: user speed and turn rate; distance and bearing of the AP relative to the facing direction; estimated tilt, FOV margin $\psi_{u,a} - \Psi_c$ and SNR from (1)–(3); number of people within 1.5 m; and the clearance of the user's own body and of the closest other person from the blocking zone (5), evaluated now and on constant-velocity extrapolations at $+0.25$, $+0.5$ and $+1$ s;
- *temporal context*: the change of the vision features over the last 133 and 267 ms;
- *radio features*: the measured SNR of the link, its change over the last 67–533 ms, and recent usability flags;
- *prior*: the Monte-Carlo forecast (7).

A three-layer perceptron with 192 units per layer maps this 77-dimensional input to per-step hazards $h_j \in (0,1)$ and marginal outage probabilities m_j. The cumulative forecast

$$\hat{P}_{u,a}(j) = 1 - \prod_{i=1}^{j} (1 - h_i) \tag{8}$$

is monotone in j by construction, and $\hat{q}_{u,a} = \frac{1}{J}\sum_j m_j$. The network is trained with the binary cross-entropy of $\hat{P}(j)$ against the realized first-outage indicator, masked to links that are usable at the decision time, plus one half of the cross-entropy of m_j.

Two design choices were needed to make the predictor usable in practice. First, it is trained on episodes with randomized perception quality (σ_p up to 0.3 m, p_{miss} up to 0.4, L_v up to 6 frames) in addition to nominal episodes, so that a degraded camera does not invalidate it. Second, the forecasts used to train the controller are produced out of fold (each training episode is predicted by a model that did not see it), which avoids training the controller on over-confident in-sample predictions.

5 Proactive handover control

5.1 Outage-Aware Expert Rule

Let s be the serving AP of user u, n_a the number of users on AP a and $\tilde{R}_{u,a} = R_{u,a}/(n_a + \mathbb{1}\{a \neq s\})$ the rate share the user would obtain. The value of a candidate AP over the forecast horizon is

$$V_{u,a} = \tilde{R}_{u,a}\left(1 - \hat{q}_{u,a}\right) - \lambda R_{\text{ref}}\hat{q}_{u,a}, \tag{9}$$

with $\hat{q}_{u,0} = 0$ for WiFi. Let g be the alternative with the largest value and j_g the number of decision steps needed to complete a HO to it. The rule starts a proactive HO when

$$\hat{P}_{u,s}(j_g) > \epsilon \quad \text{and} \quad V_{u,g} > V_{u,s}, \tag{10}$$

that is, when the serving link is likely to fail before a HO could complete and the alternative is worth it. Otherwise it applies event A3 (hysteresis and time-to-trigger), refusing targets that are themselves predicted to fail; WiFi users return to the LiFi AP with the largest value among those predicted to stay usable through a VHO. With the learned forecast this rule is called *Vision-Learned*; with (7) it is called *Vision-MC*.

5.2 Deep Reinforcement Learning Agent

The rule fixes the trade-off through two hand-tuned thresholds, whereas the DRL agent learns it from experience. P1 is cast as a semi-Markov decision process shared by all users.

- *State* $\mathbf{o}_u$ (16 features): association type; current, best-alternative and WiFi rate shares; loads of the serving, best and WiFi APs; previous rate share; time since the link was lost; forecast $\hat{P}_{u,s}$ at the HHO, VHO and full horizons and $\hat{q}_{u,s}$; and $\hat{P}_{u,b}$, $\hat{q}_{u,b}$ of the best alternative b.
- *Action* $a_u \in \{$stay, HO to b, HO to WiFi$\}$, taken only when no HO of user u is executing.
- *Reward*: the per-slot term of (6), accumulated and discounted over the slots that elapse until the user can act again, $r = \sum_{i=0}^{k-1} \gamma^i \rho_{t+i}$, with the next state discounted by γ^k.

A Double DQN [22, 23] with two hidden layers of 128 units approximates $Q(o, a)$ with target

$$y = r + \gamma^k Q_{\bar{\theta}}\left(\mathbf{o}', \operatorname{argmax}_{a'} Q_\theta(\mathbf{o}', a')\right). \tag{11}$$

When trained as a plain DQN, the agent learned to chase throughput but did not learn to avoid interruptions: the costly events are rare and appear only after the HO execution time, so the reward signal is sparse. We therefore follow deep Q-learning from demonstrations [24]: the agent first learns from the Vision-Learned rule with the TD loss plus the large-margin loss

$$\mathcal{L}_{\mathrm{E}} = \max_a [Q(\mathbf{o}, a) + \ell(a_{\mathrm{E}}, a)] - Q(\mathbf{o}, a_{\mathrm{E}}), \tag{12}$$

where a_{E} is the expert action and $\ell(a_{\mathrm{E}}, a) = 0.8$ for $a \neq a_{\mathrm{E}}$; it is then fine-tuned with ϵ-greedy interaction while one quarter of every mini-batch is still drawn from the demonstrations. The checkpoint with the best objective on separate validation episodes is kept. The resulting agent is called *DRL-Vision*; a vision-free agent trained the same way from event-A3 demonstrations serves as the *DRL (no vision)* baseline. Algorithm 1 summarizes one decision step.

Algorithm 1: Vision-assisted proactive handover (one decision step)

Track all persons; estimate heading and tilt of every user
for each user u and LiFi AP a
Build vision, temporal and radio features of link (u, a)
Predict $\hat{P}_{u,a}(1{:}J)$ by (8) and $\hat{q}_{u,a}$
end for
for each user u not executing a HO
if serving LiFi link lost for T_{det} : reactive HO to best usable AP
else $a_u \leftarrow \operatorname{argmax}_a Q_\theta(\mathbf{o}_u, a)$; start HO if $a_u \neq$ stay
end if
end for
Allocate time inside each cell by Lemma 1

6 Evaluation set-up

Table 1

Simulation Parameters

Parameter	Value
Room, LiFi APs	$8 \times 8 \times 3$ m, 2×2 grid at 2/6 m
WiFi AP	corner, 2.4 GHz, 20 MHz, 20 dBm
LED semi-angle, P_{opt}	$60°$, 3 W per AP
PD area, FOV, n_{c}, κ	1 cm^2, $80°$, 1.5, 0.53 A/W
N_0, B_{L}, $\gamma_{\min}$	10^{-21} A^2/Hz, 40 MHz, 10 dB
Body r_{b}, h_{b}; device h_{d}, δ	0.2 m, 1.75 m; 1.2 m, 0.3 m
Users / pedestrians	6 / 0–15
Walking speed, pauses	0.6–1.4 m/s, 1–8 s
Tilt statistics	from [4], $\tau_\theta = 0.5$ s
T_{HHO}, T_{VHO}, T_{det}	200 ms, 500 ms, 67 ms
A3 hysteresis, TTT	3 dB, 200 ms
Camera; σ_{p}, p_{miss}, L_{v}	30 fps; 6 cm, 0.05, 1 frame
Horizon J, MC samples K	1 s (15 steps), 32
λ, ϵ, c_{HO}, γ	2, 0.3, 0.1, 0.95

Table 1 lists the parameters. Every episode lasts 30 s. In Scenario A, users and pedestrians follow a random-waypoint model with pauses and a slow heading wobble. In Scenario B, the six users are static (seated or standing at random positions and orientations) and the pedestrians are real people: an 8 x 8 m window and a 30-s interval are cut from one of six ETH/UCY scenes [14, 15] (taken from the Trajectron++ release [25]), and their tracks are interpolated to 30 fps. All learned components are trained only on Scenario A; Scenario B is a zero-shot test.We compare eight schemes: *Reactive* (outage-triggered HO only), *STD-LTE (A3)*, *DRL (no vision)*, *Vision-Det* (deterministic Kalman forecast), *Vision-MC*, *Vision-Learned*, *DRL-Vision*, and an *Oracle* that applies the rule with perfect knowledge of future outages.

All schemes share the same channel realizations and the same reactive fallback, so differences are paired. Training uses 48 nominal and 48 perception-randomized episodes, model selection uses 6 separate episodes, and every test uses its own seeds (20 episodes per density, 10 per sweep point, 30 in Scenario B). We report the mean user throughput, the link-interruption time (fraction of time with r_u = 0), HOs per user per minute, the false-alarm ratio (proactive HOs away from a link that would not have failed within T_{HO} = 0,5 s), and 95% confidence intervals.

7 Results and discussion

7.1 Outage Prediction Accuracy

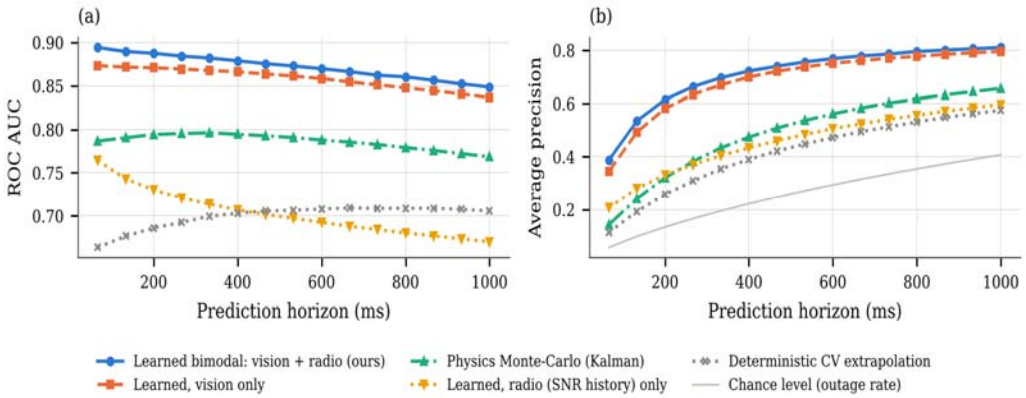


Figure 2. Accuracy of link-outage forecasts versus horizon (Scenario A, 0–15 pedestrians, 30 test episodes, links usable at the decision time). (a) Area under the ROC curve. (b) Average precision; the grey line is the outage rate, i.e. the precision of a random predictor.

Table 2

Outage-Prediction Ablation (ROC AUC / Average Precision)

Predictor	**200 ms**	**533 ms**	**1 s**
Deterministic Kalman	0.69 / 0.26	0.71 / 0.45	0.71 / 0.58
Monte-Carlo Kalman	0.79 / 0.32	0.79 / 0.54	0.77 / 0.66
Learned, radio only	0.73 / 0.33	0.70 / 0.48	0.67 / 0.60
Learned, vision only	0.87 / 0.58	0.86 / 0.74	0.84 / 0.80
Learned, vision + radio, no MC prior	0.88 / 0.59	0.87 / 0.74	0.84 / 0.80
Learned, vision + radio	0.88 / 0.60	0.87 / 0.75	0.84 / 0.80
+ perception randomization (final)	**0.89 / 0.62**	**0.87 / 0.76**	**0.85 / 0.81**
Outage rate (chance AP)	0.13	0.27	0.41

Figure 2 and Table 2 compare the forecasts. The deterministic Kalman extrapolation is the weakest, because a single trajectory either crosses the blocking zone or not and it ignores tilt uncertainty. Sampling the posterior (Monte-Carlo) raises the AUC at 200 ms from 0.69 to 0.79.

The learned predictor gains a further 0.10 in AUC and almost doubles the average precision (0.32 to 0.62), which matters because outages are rare at short horizons. According to the ablation, most of this gain comes from the vision features: radio-only learning reaches only 0.73, whereas vision-only learning reaches 0.87.

The radio history adds a small but consistent improvement, which we attribute mainly to tilt-induced FOV losses, which appear in the SNR trend before the link drops. Removing the Monte-Carlo prior does not change the accuracy, so the Kalman sampling can be dropped at deployment; training with randomized perception quality improves every horizon.

7.2 Network Performance Versus Crowd Density

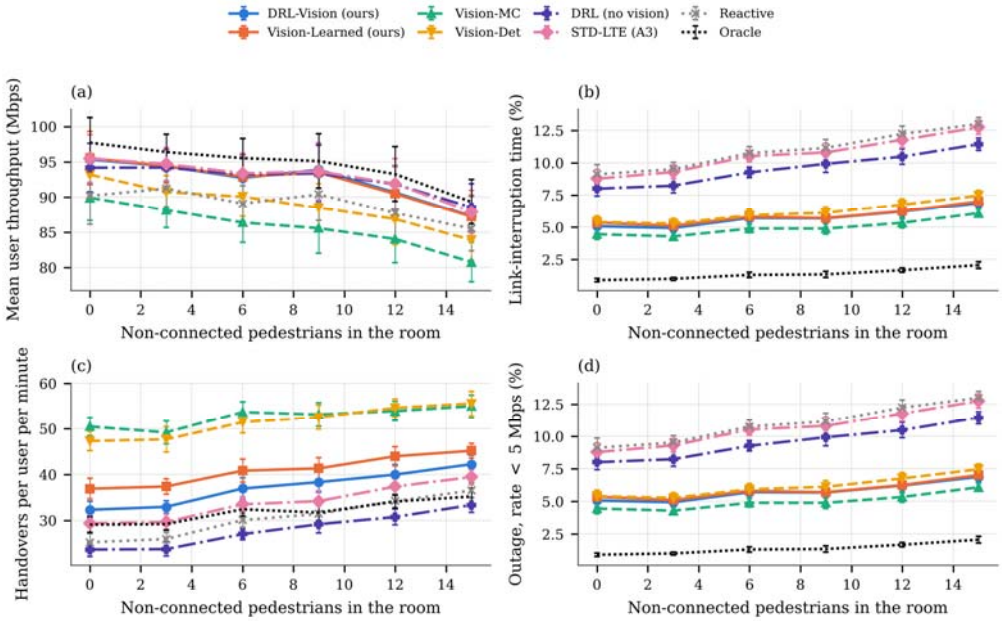


Figure 3. Scenario A, six users and 0–15 non-connected pedestrians (20 episodes per point, 95% confidence intervals). (a) Mean user throughput. (b) Link-interruption time. (c) Handovers per user per minute. (d) Outage probability (rate below 5 Mb/s).

Table 3

Scenario A With Nine Pedestrians (Mean ± 95% Confidence Interval Over 20 Episodes)

Scheme	Throughput (Mb/s)	Interruption (%)	No. of interruptions	Median length (ms)	HO/user/min	False alarms (%)	On WiFi (%)
Reactive	90.4 ± 3.8	11.15 ± 0.65	1522	233	31.4	–	21
STD-LTE (A3)	93.7 ± 4.0	10.81 ± 0.70	1480	233	34.2	–	22
DRL (no vision)	93.4 ± 4.0	9.93 ± 0.65	1345	233	29.2	60	29
Vision-Det	88.5 ± 3.4	6.12 ± 0.47	1086	167	52.5	43	34
Vision-MC	85.6 ± 3.5	4.89 ± 0.43	838	167	53.2	49	40
Vision-Learned	93.5 ± 3.9	5.71 ± 0.42	1000	167	41.3	26	31
DRL-Vision	**93.9 ± 3.7**	**5.69 ± 0.42**	1018	167	38.3	27	31
Oracle	95.1 ± 3.8	1.36 ± 0.24	387	100	31.7	12	32

Figure 3 and Table 3 report the network-level results. Interruption grows with crowd density for every scheme, because each additional person is a potential blocker; at zero pedestrians the outages are caused by self-blockage and tilt alone. The two radio-only baselines behave alike: event A3 improves throughput over the purely reactive scheme by moving users to stronger APs, but neither can act before a link is lost, and both leave users without service for about 11% of the time. The vision-free DRL agent saves less than one percentage point.

All vision-assisted schemes reduce interruption considerably, although at different costs. Vision-MC achieves the lowest interruption among the realizable schemes (4.9%) but loses 8.6% of throughput, because half of its proactive handovers are false alarms that move users to the slower WiFi network (40% of the time). The learned forecast halves the false-alarm ratio (26-27%). As a result, Vision-Learned and DRL-Vision reduce interruption by 39-47% and 42-47%, respectively, across all densities while keeping throughput within the confidence interval of STD-LTE. At nine pedestrians, DRL-Vision reduces interruption from 10.81% to 5.69% (p = 9 x 10^{-5}, paired Wilcoxon test) and changes throughput by +0,3% (p = 0,55). It also uses 7% fewer handovers than the rule with the same forecast (38.3 vs. 41.3 per minute), although it still hands over 12% more often than STD-LTE.

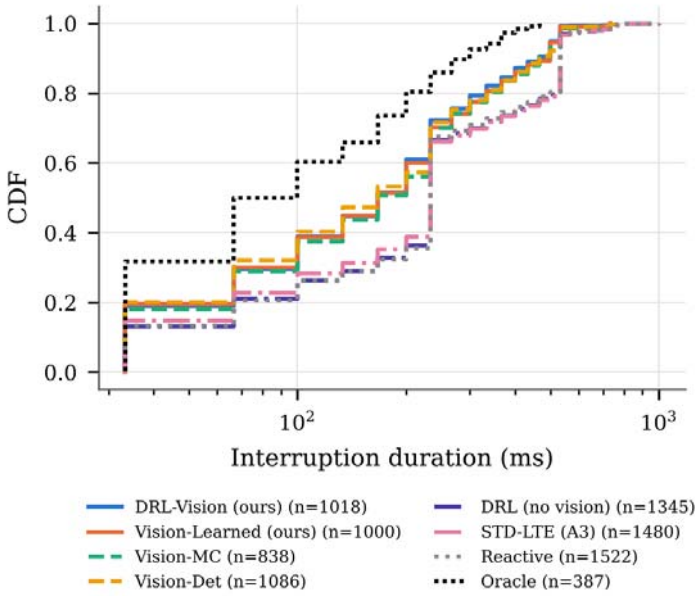


Figure 4. CDF of the duration of individual interruptions (nine pedestrians); *n* is the number of interruptions over 20 episodes.

Figure 4 shows how the interruptions themselves change. Proactive schemes have fewer interruptions (1018 instead of 1480) and shorter ones: the median duration falls from 233 ms, the detection plus horizontal-HO time of a reactive switch, to 167 ms. The remaining long interruptions are blockages that the forecast missed or that started while a handover was executing.

7.3 Throughput–Reliability Trade-Off

Because a single operating point can hide a trade-off, we also swept the parameters of every scheme (Fig. 5). No setting of STD-LTE brings interruption below 9.4%: without foresight, faster triggering only exchanges throughput for more ping-pong. The vision-assisted schemes reach operating points that are not available to radio-only control. The frontier of the learned forecast dominates both Kalman-based forecasts and every STD-LTE configuration: it reaches 96.1 Mb/s, above the best STD-LTE throughput (95.7 Mb/s), and it can bring interruption down to 2.6% if about 9% of throughput is sacrificed.

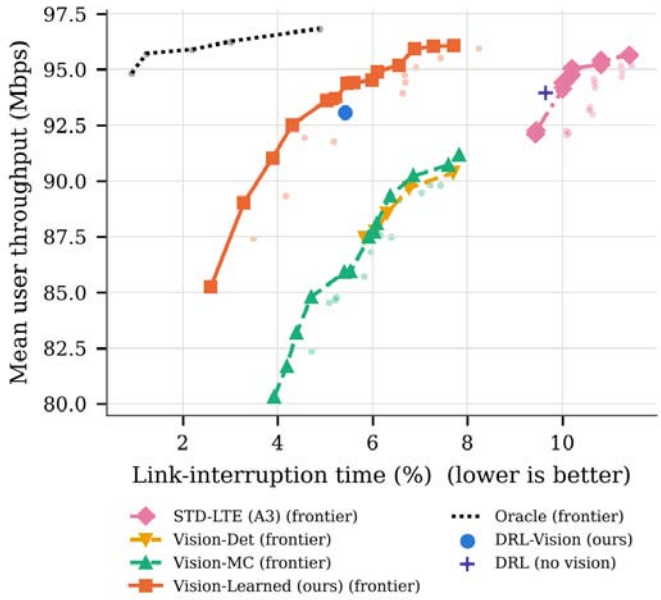


Figure 5. Throughput versus interruption on validation episodes (nine pedestrians). Each rule-based scheme is swept over $\epsilon \in \{0.1, \ldots, 0.7\}$ and $\lambda \in \{0, \ldots, 4\}$; STD-LTE over 27 combinations of hysteresis, time-to-trigger and detection delay. Lines connect Pareto-optimal points.

DRL-Vision, trained for one value of λ, lies within about 1 Mb/s of this frontier without any threshold tuning. It does not move beyond the frontier of the tuned rule, so in this study the main source of the gain is the forecast rather than the learning-based controller. The gap to the Oracle frontier (below 1% interruption at 95 Mb/s) shows how much further improvement is possible from better prediction.

7.4 Robustness to Perception Errors

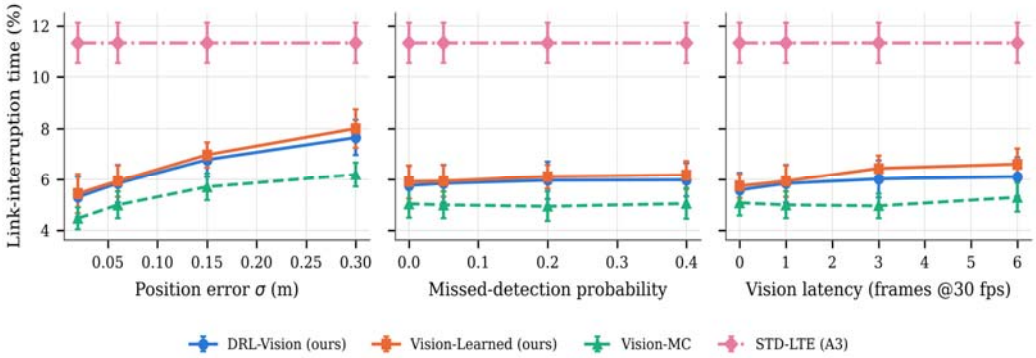


Figure 6. Interruption time versus perception quality (nine pedestrians, 10 episodes per point): floor-position error, missed-detection probability, and pipeline latency.

Table 4

Forecast ROC AUC at 200 ms Under Perception Shift

Test condition	MC Kalman	Learned	Learned + rand.
Nominal	0.80	0.88	**0.89**
σ_p = 0,15 m	0.75	0.85	**0.87**
σ_p = 0,30 m	0.71	0.81	**0.84**
pmiss = 0,4	0.78	0.87	**0.88**
L_v = 6 frames (200 ms)	0.76	0.86	**0.87**
Real trajectories (ETH/UCY)	0.84	0.93	**0.94**

In a real deployment, the camera pipeline will be noisier than in our nominal set-up. Figure 6 shows that missed detections up to 40% and latencies up to 200 ms raise the interruption of DRL-Vision by at most 0.3 percentage points. Position error matters more: at σ_p = 0,30 m, comparable to the radius of a body, interruption rises from 5.8% at the nominal 6 cm to 7.7%, still 32% below STD-LTE. The physics-based forecast degrades less in relative terms because its uncertainty model widens with the measurement noise, whereas the network has to learn this effect. Table 4 shows that training with randomized perception quality recovers part of the loss at the prediction level (AUC 0.81 to 0.84 at 0.3 m). Under all the conditions we tested, the learned forecast remained the more accurate of the two.

7.5 Sensitivity to Handover Execution Time

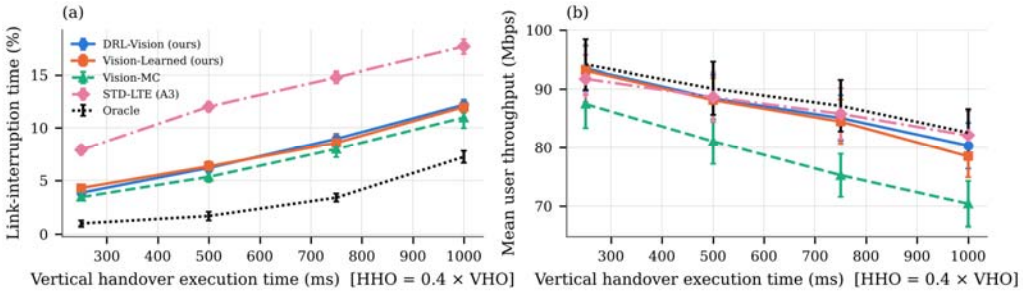


Figure 7. Effect of the handover execution time (nine pedestrians, 10 episodes per point; $T_{HHO} = 0{,}4T_{VHO}$). (a) Interruption time. (b) Throughput

The HO execution time in HLWNets depends on the protocol stack and is uncertain, so Figure 7 scales it from T_{VHO} = 250 ms to 1 s. Interruption grows for every scheme because a longer execution needs a longer, less accurate forecast and leaves less margin. DRL-Vision cuts interruption by 51% at 250 ms (7.9% to 3.8%) and by 31% at 1 s (17.7% to 12.2%), and keeps throughput within 2.2% of STD-LTE. Vision-MC loses up to 14% of throughput at long execution times because its false alarms become more expensive.

7.6 Zero-Shot Test With Real Pedestrian Trajectories

Table 5

Scenario B: Static Users, Real ETH/UCY Pedestrians
(30 Episodes, Mean 12.4 Pedestrians in the Room)

Scheme	Throughput (Mb/s)	Interruption (%)	HO/user/min
Reactive	104.7 ± 7.3	3.46 ± 0.74	10.6
STD-LTE (A3)	106.5 ± 7.3	3.57 ± 0.79	12.7
DRL (no vision)	109.4 ± 7.5	2.81 ± 0.66	8.9
Vision-Det	105.0 ± 7.5	1.74 ± 0.48	31.0
Vision-MC	103.4 ± 7.5	1.30 ± 0.28	35.5
Vision-Learned	107.6 ± 7.8	1.76 ± 0.41	16.3
DRL-Vision	107.8 ± 7.4	1.70 ± 0.36	14.2
Oracle	108.1 ± 7.7	0.60 ± 0.14	10.9

Scenario B tests whether models trained on synthetic motion transfer to real crowds and to a different usage pattern, with static users and pedestrians whose number in the room varies from 1 to 32 (median 5.7). Interruption is lower than in Scenario A because static users suffer no self-blockage changes. Table 5 shows that, without retraining, DRL-Vision reduces interruption by 53% relative to STD-LTE (p = 3 x 10^{-6}) with a +1,2% change in throughput (p = 0,75), and the learned forecast reaches an AUC of 0.94 (Table 4). Vision-MC again achieves the lowest interruption, but at the cost of 2.9% throughput (p = 0,015) and 2.5 times as many handovers as DRL-Vision.

7.7 Complexity

On one core of a general-purpose CPU, Kalman tracking of all persons takes 0.13 ms per frame. Building the link features and evaluating the predictor (94 878 parameters) for the 24 user-AP links takes 0.8 ms per decision step, and the DQN (19 075 parameters) a negligible further amount. The Monte-Carlo forecast with 32 samples takes 6.6 ms per decision and can be omitted, since it does not improve the learned predictor. The added computation is therefore small compared with the 67 ms decision period; the person detector dominates the edge workload and is accounted for through the latency L_v.

8 Limitations and future work

Several limitations of this study should be noted.

- *Emulated perception.* The detector and tracker are modelled by their output errors rather than run on video. The robustness sweeps bound the effect of these errors, but an end-to-end evaluation with recorded or rendered video, real detector failures and identity switches is needed.
- *Device association.* We assume that the network knows which tracked person carries which device. Practical options include LiFi uplink positioning and matching camera motion with inertial sensor data.
- *Channel model.* We consider the LoS channel with orthogonal LiFi bands. Diffuse reflections would soften some blockages, and inter-cell interference would couple the association decisions more strongly.
- *Controller.* The DRL agent matches but does not exceed a well-tuned rule using the same forecast. Its value here is that it learns the operating point from the reward.

Learning a joint policy for all users and extending the action space to per-user time allocation are natural next steps.

- *Privacy.* Processing at the edge and exporting only floor positions and pose angles reduces the exposure of video. A deployment would still require a privacy assessment.

9 Conclusion

We have shown that the cameras already installed in many smart buildings can be used to make LiFi handover proactive. The central element is a link-level forecast that respects LiFi geometry, including the short blocking zone, self-blockage and device tilt, and that is learned from vision and radio features. This forecast raised the 200-ms outage-prediction AUC from 0.79 for a Kalman/Monte-Carlo model to 0.89. Used by a DRL handover agent with proportional-fair resource allocation, it reduced link-interruption time by 42-47% across crowd densities, with no loss of throughput and with fewer false alarms than physics-based forecasting. The gain held, without retraining, with real pedestrian trajectories (53% lower interruption). The remaining gap to the oracle suggests that improving the prediction, rather than the controller, is the most promising direction for future work.

REFERENCES

[1] H. Haas, L. Yin, Y. Wang, and C. Chen, “What is LiFi?” *J. Lightw. Technol.*, vol. 34, no. 6, pp. 1533–1544, 2016, doi: 10.1109/JLT.2015.2510021.

[2] “IEEE standard for information technology–Telecommunications and information exchange between systems–Local and metropolitan area networks–Specific requirements–Part 11: Wireless LAN medium access control (MAC) and physical layer (PHY) specifications–Amendment 6: Light communications,” *IEEE Std 802.11bb-2023*, 2023.

[3] X. Wu, M. D. Soltani, L. Zhou, M. Safari, and H. Haas, “Hybrid LiFi and WiFi networks: A survey,” *IEEE Commun. Surveys Tuts.*, vol. 23, no. 2, pp. 1398–1420, 2021, doi: 10.1109/COMST.2021.3058296.

[4] M. D. Soltani, A. A. Purwita, Z. Zeng, H. Haas, and M. Safari, “Modeling the random orientation of mobile devices: Measurement, analysis and LiFi use case,” *IEEE Trans. Commun.*, vol. 67, no. 3, pp. 2157–2172, Mar. 2019.

[5] Y. Wang and H. Haas, “Dynamic load balancing with handover in hybrid Li-Fi and Wi-Fi networks,” *J. Lightw. Technol.*, vol. 33, no. 22, pp. 4671–4682, 2015, doi: 10.1109/JLT.2015.2480969.

[6] D. Frómeta Fonseca, B. Genovés Guzmán, G. L. Martena, R. Bian, H. Haas, and D. Giustiniano, “Prediction-model-assisted reinforcement learning algorithm for handover decision-making in hybrid LiFi and WiFi networks,” *J. Opt. Commun. Netw.*, vol. 16, no. 2, pp. 159–170, 2024, doi: 10.1364/JOCN.495234.

[7] S. Karimkhan and H. Shokrzadeh, “Reinforcement learning-based dueling DQN for access point selection and handover management in mobile hybrid LiFi/WiFi networks,” *Wireless Pers. Commun.*, 2026, doi: 10.1007/s11277-026-12215-w.

[8] P. Hou and N. Cen, “Deep reinforcement learning-based user association in hybrid LiFi/WiFi indoor networks,” *arXiv preprint* arXiv:2503.01803, 2025.

[9] G. Charan, M. Alrabeiah, and A. Alkhateeb, “Vision-aided 6G wireless communications: Blockage prediction and proactive handoff,” *IEEE Trans. Veh. Technol.*, vol. 70, no. 10, pp. 10193–10208, 2021, doi: 10.1109/TVT.2021.3104219.

[10] A. Alkhateeb, G. Charan, T. Osman, A. Hredzak, J. Morais, U. Demirhan, and N. Srinivas, “DeepSense 6G: A large-scale real-world multi-modal sensing and communication dataset,” *IEEE Commun. Mag.*, vol. 61, no. 9, pp. 122-128, 2023, doi: 10.1109/MCOM.006.2200730.

[11] S. Karunasena, E. Khordad, T. Drummond, and R. Senanayake, “Deep learning-based computer vision for beam selection and proactive blockage prediction,” *arXiv preprint* arXiv:2605.04514, 2026.

[12] Y. Ahn, J. Kim, S. Kim, and B. Shim, “Computer vision-aided proactive mobility management for 6G terahertz communications,” in *Proc. IEEE Global Commun. Conf. (GLOBECOM)*, 2023, pp. 1513-1518, doi: 10.1109/GLOBECOM54140.2023.10437835.

[13] S. Naser, O. Alhussein, and S. Muhaidat, “Towards multi-modal and cross-modal integration in LiFi-based sensing,” *Sci. Rep.*, vol. 16, Art. no. 6038, 2026, doi: 10.1038/s41598-026-36891-7.

[14] S. Pellegrini, A. Ess, K. Schindler, and L. van Gool, “You’ll never walk alone: Modeling social behavior for multi-target tracking,” in *Proc. IEEE Int. Conf. Comput. Vis. (ICCV)*, 2009, pp. 261-268.

[15] A. Lerner, Y. Chrysanthou, and D. Lischinski, “Crowds by example,” *Comput. Graph. Forum*, vol. 26, no. 3, pp. 655-664, 2007.

[16] S. Chatterjee, D. Sabui, and B. Roy, “Mobility aware blockage management of a multi-user multi-cell hybrid Li-Fi Wi-Fi system with freeform diversity receiver,” *Opt. Commun.*, vol. 560, Art. no. 130487, 2024, doi: 10.1016/j.optcom.2024.130487.

[17] J. M. Kahn and J. R. Barry, “Wireless infrared communications,” *Proc. IEEE*, vol. 85, no. 2, pp. 265-298, 1997.

[18] S. Dimitrov and H. Haas, “Information rate of OFDM-based optical wireless communication systems with nonlinear distortion,” *J. Lightw. Technol.*, vol. 31, no. 6, pp. 918–929, 2013.

[19] V. Erceg et al., “TGn channel models,” *IEEE 802.11 document 03/940r4*, 2004.

[20] J. Redmon, S. Divvala, R. Girshick, and A. Farhadi, “You only look once: Unified, real-time object detection,” in *Proc. IEEE Conf. Comput. Vis. Pattern Recognit. (CVPR)*, 2016, pp. 779-788.

[21] Y. Zhang et al., “ByteTrack: Multi-object tracking by associating every detection box,” in *Proc. Eur. Conf. Comput. Vis. (ECCV)*, 2022, pp. 1-21.

[22] V. Mnih et al., “Human-level control through deep reinforcement learning,” *Nature*, vol. 518, pp. 529-533, 2015.

[23] H. van Hasselt, A. Guez, and D. Silver, “Deep reinforcement learning with double Q-learning,” in *Proc. AAAI Conf. Artif. Intell.*, vol. 30, 2016, pp. 2094-2100.

[24] T. Hester et al., “Deep Q-learning from demonstrations,” in *Proc. AAAI Conf. Artif. Intell.*, vol. 32, 2018, pp. 3223-3230.

[25] T. Salzmann, B. Ivanovic, P. Chakravarty, and M. Pavone, “Trajectron++: Dynamically-feasible trajectory forecasting with heterogeneous data,” in *Proc. Eur. Conf. Comput. Vis. (ECCV)*, 2020, pp. 683-700.

SYNCHROINFO JOURNAL

www.media-publisher.eu/synchroinfo-journal

OUTPHASING POWER AMPLIFIER EFFICIENCY

Quoc Fung Ngo [1], Oleg V. Varlamov [1,2,*]

[1] Moscow Technical University of Communications and Informatics, Moscow, Russia;
[2] Institute of Radio and Information Systems (IRIS), Vienna, Austria; vov@mtuci.ru
* Correspondence: vov@mtuci.ru

ABSTRACT

This article examines the operating characteristics of channel generators in outphasing high-efficiency radio-frequency power amplifiers. It demonstrates the advantage of using Voltage Mode Class D (VMCD) switching generators with filter loads (FL) on field-effect (FET) transistors – MOSFETs, VDMOS, LDMOS, and GaN HEMTs. Based on equivalent circuits and currents and voltages diagrams, basic expressions are derived for calculating output power, power loss, efficiency, and maximum currents when operating with matched and mismatched (complex) loads. The presence of inverse currents is demonstrated, and their maximum values, achievable with a 45-degree phase shift, are determined, which are necessary for selecting the component base.

DOI: 10.36724/2664-066X-2026-12-4-19-31

Received: 15.04.2026
Accepted: 27.06.2026

KEYWORDS: *outphasing power amplifier; energy efficiency; switching generator; Voltage Mode Class D; filter loads; field-effect transistor; equivalent circuits; mismatched loads; inverse currents.*

Citation: Q.F. Ngo, O.V. Varlamov, "Outphasing power amplifier efficiency," *Synchroinfo Journal* **2026**, vol. 12, no. 4, pp.19-31.

Licensee IRIS, Vienna, Austria.

This article is an open access article distributed under the terms and conditions of the Creative Commons Attribution (CC BY) license (https://creativecommons.org/licenses/by/4.0/).

Copyright: © 2026 by the authors.

1 Introduction

High-efficiency radio-frequency power amplifiers built using the outphasing method (OPA) [1, 2] with channel power direct summation [3, 4] have good prospects for use in modern telecommunications systems. They exhibit sufficient linearity [5-7] to amplify signals with high crest factors, such as OFDM, for digital television [8] and radio broadcasting [9, 10], satellite applications [11-13], and others. Unlike other "synthetic" high-efficiency amplification methods (envelope elimination and restoration - EER, envelope tracking - ET), OPA does not contain a powerful modulation path [14, 15], which reduces efficiency and limits the amplified frequency band and antenna matching requirements [16, 17]. Therefore, the OPA is a good base element for the combined use of "synthetic" high-efficiency amplification methods [18-20]. However, a detailed examination of the OPA energy characteristics associated with power losses of various origins has not yet been conducted.

Based on the analysis of methods for two out-of-phase generators powers combining, conducted in [21] an important conclusion was reached: when generators in the switching (overvoltage) mode series summing, this mode is maintained with increasing phase shift between the driving signals up to 180^0, ensuring high generator efficiency. Therefore, it is proposed to design the final stages of outphasing transmitters using a series direct summation method. At the same time, as shown in [22], the change in the load delivered to the generators is very significant, caused by both the mutual phasing of the generators and the mismatch of the OPA's final load. This raises the problem of selecting, among known oscillator circuits, those switching generator variants that are least sensitive to load mismatch. After this, it is necessary to conduct a detailed analysis of the operating mode of the selected generator when used in the OPA's output stage, which will allow us to evaluate the power characteristics of the transmitter as a whole and develop recommendations for the channel amplifiers final stages design. This article is devoted to solving this problem.

2 Selecting Switching Oscillator for OPA Output Stage

Voltage Mode Class D (VMCD) oscillators with resistive (RL) and filter loads (FL) [23, 24] possess the required properties – operating as a voltage generator and maintaining their properties even with significant phase misalignment (up to 180 degrees) of the summed signals. Of these two types of switching oscillators, the VMCD with filter loads circuit is immediately preferable to the resistive load option, since the latter suffers from high harmonic power losses in the ballast resistance of the diplexer (filter plug), connected between the oscillator and the load to provide resistive loading of the oscillator for the first and higher harmonics [23].

At the same time, the construction of OPA output stages using VMCD FL switching generators is advisable only when the latter are built on field-effect (FET) transistors - MOSFET, VDMOS, LDMOS, GaN HEMT. This is due to two reasons. Firstly, as will be shown in the following sections, during outphasing (when operating on a resistive or complex load), the current pulses in the transistors become asymmetrical and bipolar, i.e. there are time intervals during which negative (inverse) current flows. Bipolar transistors ensure its flow significantly worse than FETs, and even the inclusion of special diodes [23] in parallel with the transistors output electrodes does not completely eliminate the consequences of this drawback. Secondly, in bipolar transistors, due to the relatively long carrier absorption time in the base-collector junction, when the transistor leaves the saturation state, overlap (expansion of the collector current pulses) occurs, which, in turn, leads to the appearance of shoot-through currents during time intervals when both switches are closed [22]. This phenomenon becomes especially noticeable when generators are operating on highly variable loads, which occurs during outphasing.

VMCD FL generators based on field-effect transistors, as follows from the fundamentals of the theory of their operation, should be free from the listed disadvantages. Thus, when field-effect transistors operate in the switching mode, there is no accumulation of charges and, therefore, the main reason for the occurrence of through currents is eliminated (strictly speaking, through currents in FET transistors can sometimes still occur, but for a completely different reason). In addition, field-effect transistors are switches with double-sided conductivity and allow the passage of inverse currents, which virtually eliminates the risk of surge currents and voltages and eliminates the need to bypass the output electrodes of transistors with additional diodes. Thus, VMCD FL generators based on field-effect MOSFET or GaN [25] transistors must maintain operability and high energy

characteristics with large changes in equivalent loads when operating in the OPA final stage.

Next, the operating mode of the VMCD FL generator is examined in detail when used in the OPA final stage, the features of this mode in the case of a large load mismatch are considered, and its energy characteristics are assessed.

3 Operation of the OPA Final Stage with a Matched Load

Let's consider the operation of push-pull switching oscillators VMCD FL (Fig. 1). When the switch is closed, a half-wave of the harmonic load current flows through it. It should be noted that the voltages at the transistor output electrodes differ from the voltages at the switches by the amount of the voltage drop across the resistor r_{sat}. When the switch is closed, the voltage drops across the switch itself is zero, and the voltage across the transistor is $U_{sat}(t) = r_{sat} * i_L(t)$. When the switch is open, almost the entire supply voltage $U(t) = E - U_{sat}(t)$ drops across the switch, and the current through it is zero. Fig. 2a) shows the current and voltage waveforms at the switches of the one OPA generator when operating with a resistive load R_L.

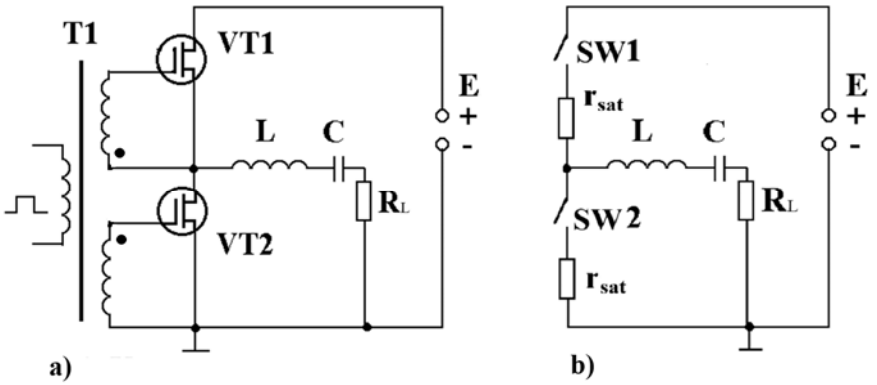


Figure 1. a) push-pull switching VMCD FL generator circuit;
b) simpli ed equivalent circuit

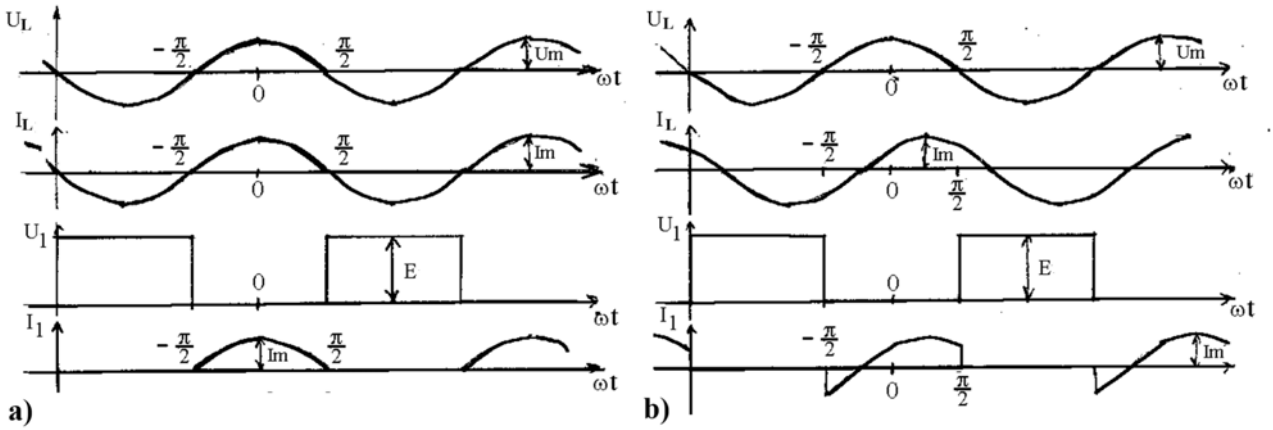


Figure 2. Current and voltage diagrams for one VMCD FL generator operating on resistive (a) and complex (b) loads

In the OPA final stage, two switching VMCD FL generators operate on a common load, which is reflected in the equivalent circuit shown in Figure 3. Here, each generator is represented by two switches (in one arm, switches 1.1 and 1.2, in the other, respectively, 2.1 and 2.2), with the saturation resistance of the transistors r_{sat} connected in series with each of them. Relative to the common filter load (L, C, R_L), the generators are connected in series. In the case of common-mode driving (when $2\varphi = 0$), the operating mode of both

generators is the same as that of a single generator (see the circuit in Fig. 1 and the diagrams in Fig. 2a). In this case, in the circuit in Figure 3, the diagonally located switches (switches 1.1, 2.2 and switches 1.2, 2.1) are switched in pairs in phase. In this case, the current and voltage diagrams for each of the switches of both generators coincide with the diagrams illustrating the operation of a single VMCD FL generator (Fig. 2a). The only difference lies in the magnitude of the reduced load resistances for each generator, which will be half the total load R_L (due to the fact that in the circuit under consideration, the generator powers are serially summed).

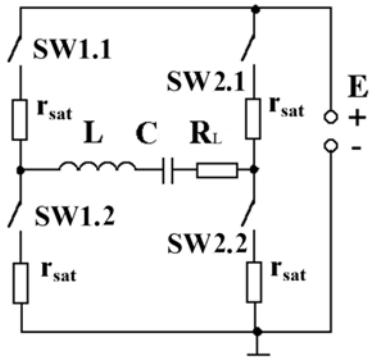


Figure 3. Output stage equivalent circuit of linear power amplifier using the outphasing method

With out-of-phase driving, the output voltage pulses and, accordingly, the first harmonics of the voltages on the switches $U_{SW}(t)$ of both generators (on switches 1.1 and 2.2 and, similarly, on switches 1.2 and 2.1) are shifted in phase relative to each other by the value 2φ, varying from 0 to 180 degrees according to the law determined by the OPA channel signal generator (Exciter) [26]. In this case, the pulse voltages and, accordingly, the first harmonics of the voltages on the switches relative to the output pulse voltage (voltages on the circuits L, C, RL) and its first harmonic are shifted by the value -φ for switches 1.1 and +φ for switches 2.2 (see Fig. 4).

In each switch, as at 2φ=0, the current $i_{sw}(t)$ flows for half the period. However, if at 2φ=0 this current is unipolar cosine pulses with a cutoff angle of 90^0 (as in the case of a single VMCD FL generator, see Fig. 2,a), then at 2φ>0 the switch current pulses $i_{sw}(t)$ are cosine segments of the same duration (φ), but with a phase shift φ. Thus, as can be seen from Figure 4, the pulses $i_{sw}(t)$ contain intervals where the current is negative (inverse). With increasing φ, the duration of these intervals increases and at $2\varphi \geq 180^0$ it approaches the duration of the intervals where the current is positive. In this case, the constant component in the current pulses decreases and at $2\varphi = 180^0$ it vanishes. At the same time, the output voltage pulses become infinitely short and the amplitude of the output signal is also zero. The corresponding current and voltage diagrams are shown in Figure 5. Thus, an analysis of Figure 4 and Figure 5 shows that with an increase in φ, the durations of the positive and negative output voltage pulses (voltages in the L, C, and R_L circuits) decrease and tend to zero at $2\varphi \rightarrow 180^0$. In this case, although the output voltage swing $U_{out}(t)$ remains unchanged and equal to 2E, the amplitude of the first harmonic voltage on the R_L load and the current in it tend to zero.

An interesting feature of the OPA output stage is that during intervals when the upper or lower pair of switches are closed, the load circuit is short-circuited by these switches, and the load current flows due to the energy stored in the output filter reactive elements. During these intervals, the power supply is disconnected from the load and delivers no power (no current flows through it). These features ensure OPA high efficiency with any phase shifts of the channel signals.

4 Operation of the OPA Final Stage with a Complex Load

As shown in the previous sections, with a complex load mismatch of a single VMCD FL generator (see Fig. 1), the load current lags or leads the phase of the voltages first harmonic on the switches. In this case, the current pulses in the switches become asymmetrical (see Fig. 2,b) and contain both positive and negative current sections (inverse current sections).

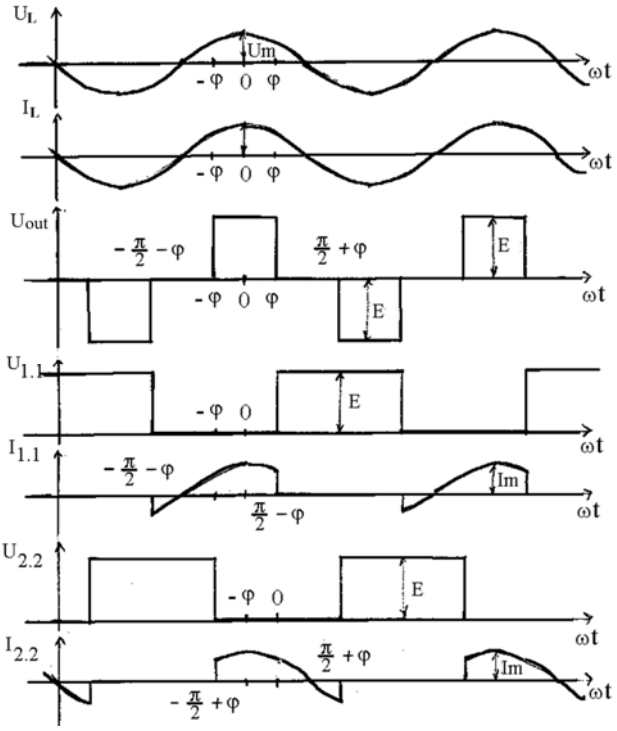


Figure 4. Current and voltage diagrams for VMCD FL generators operating on a resistive load during outphasing (φ>0)

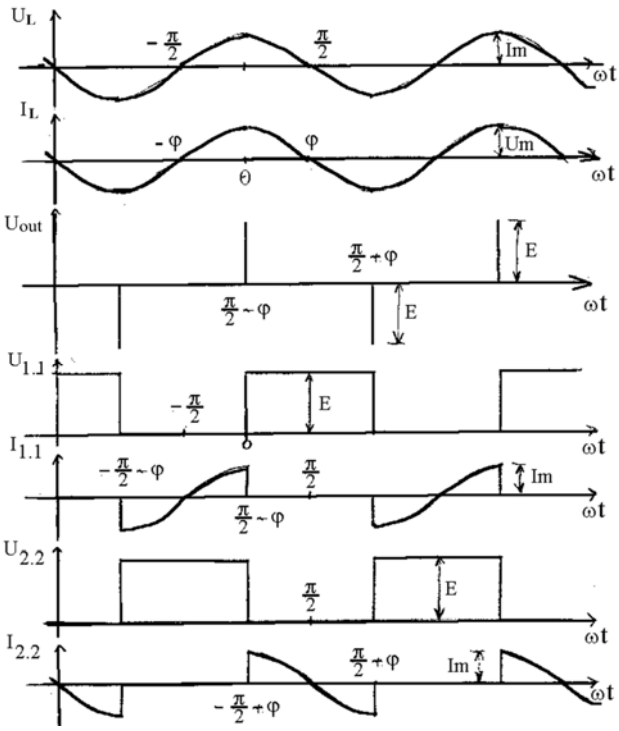


Figure 5. Current and voltage diagrams in the case of antiphase VMCD FL generators operation on a resistive load

In the OPA final stage (see the diagram in Fig. 3), with in-phase operation of two VMCD FL generators (2φ=0) and a common load mismatch, as with a single VMCD FL generator operating with a complex load, negative sections appear in the current pulses in the switches (inverse currents). When comparing the waveforms in Figure 2,b with those in Figure 4 shows that, while with a resistive load and outphasing, the phase shifts between the midpoints of the pulses and the first harmonics of the voltages on different switches and the maximum current in the load are equal in magnitude but opposite in sign. With a complex load and in-phase operation (2φ=0), the phase shifts are identical in both magnitude and sign in both generators. It follows that with outphasing and a complex load, the current pulses in the switches should have different shapes in different generators.

Thus, Figures 6 and 7 show the current and voltage waveforms on the switches under a complex load – inductive and capacitive, respectively. Depending on the sign of X_L, the current lags or leads the first harmonic of the total voltage, i.e., it has a certain phase shift χ relative to it and the current in the matched load. Note that the shape of the voltage pulses on the switches, as well as the shape of the total voltage from the two generators $U_{out}(\omega t)$, remains unchanged at $X_L \neq 0$, since we assume that the switching mode of the VMCD FL generators is maintained.

Figure 8 shows the pulse waveforms of currents and voltages on the switches for a very interesting special case, when the current in the load is in phase with the voltage on the switches of one of the VMCD FL generators, and the voltage on the switches of the other VMCD FL generator will be 90^0 out of phase (will be in quadrature) from the current in the load (i.e., for the case when $\varphi + \chi = \pi / 2$ or $-\varphi + \chi = 0$). In this case, the first generator works on a purely resistive load, and the second on a purely reactive one. When considering the waveforms for this case (see Fig. 8), it is easy to see that, indeed, for the current pulses of one of the switches, the sine (quadrature) component of the first harmonic vanishes (these pulses represent harmonic pulses with a cutoff angle of $\theta = 90^0$), while for the other, the cosine (in-phase) component vanishes.

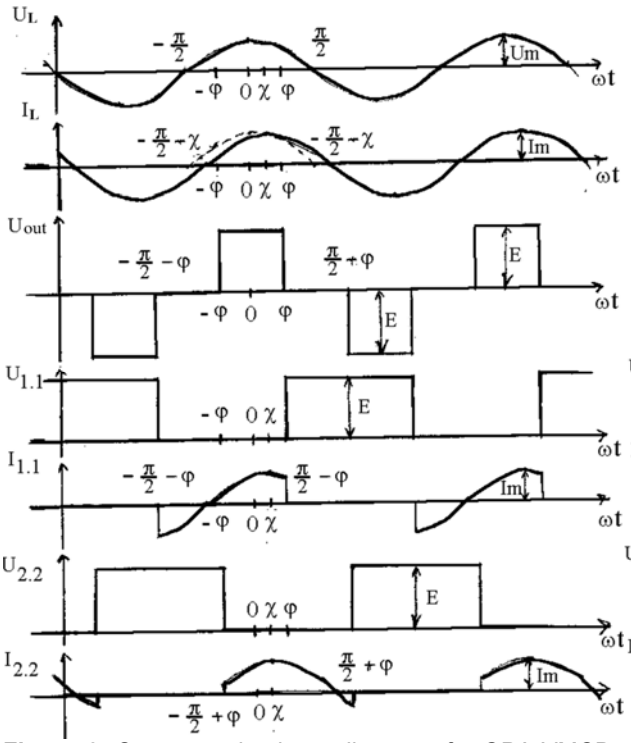


Figure 6. Current and voltage diagrams for OPA VMCD FL generators operating on a complex inductive load

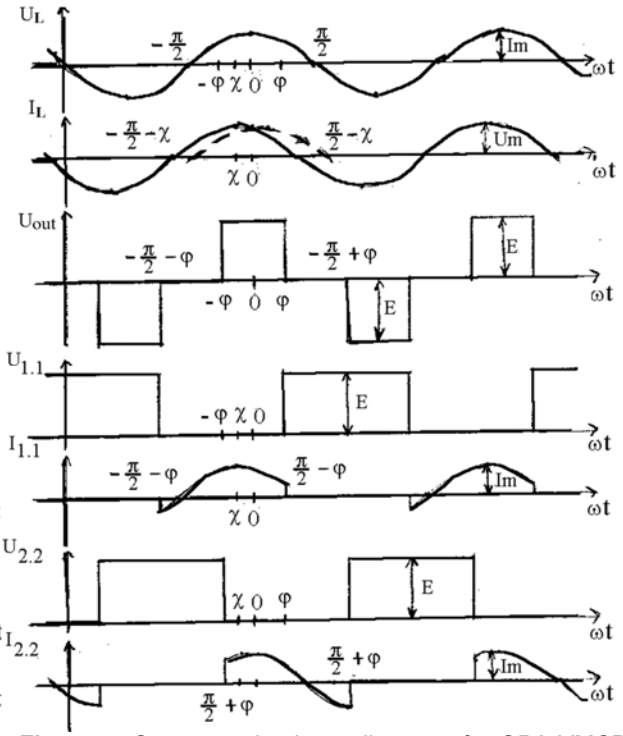


Figure 7. Current and voltage diagrams for OPA VMCD FL generators operating on a complex capacitive load

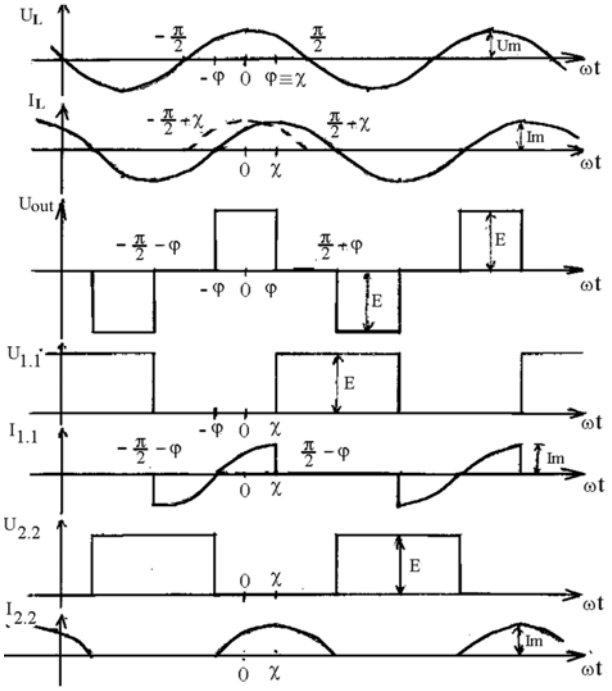


Figure 8. Current and voltage diagrams for OPA VMCD FL generators operating with a complex load – a special case

This indicates that one of the generators operates with a purely resistive load, while the other operates with a purely reactive load. In this case, the generator whose cosine (in-phase) component of the current pulses in the switches vanishes will not consume power from the power source, since in such pulses (see Fig. 8), the DC component is zero, meaning that the current consumed by the generator from the power source will also be zero. As φ increases, the DC component of the currents in the switches of this generator becomes negative. The current and power consumed by this generator also become negative, and it returns (recuperates) oscillatory power to the power supply. This, in turn, reduces the total power consumed and the power in the shared load of the two generators.

For such modes, as will be shown in Section 7, the efficiency of the OPA is virtually unchanged; the active device modes (currents and voltages at the drains of the output transistors) do not exceed their values at the point of maximum output power (common-mode mode) and are determined solely by the degree of mismatch in the shared load, as for a single VMCD FL generator [24].

5 Power Characteristics of the OPA Output Stage Operating with a Complex Load

To calculate OPA output stage power characteristics, we find expressions for the DC components of the currents in the switches, as well as the first harmonics of the voltages across them, according to the equivalent circuit in Figure 3, using the current and voltage diagrams in Figures 4...8. When deriving the relationships, we will limit ourselves to the analysis for switches 1.1 and 2.2 in the circuit in Figure 3, since the relationships for the other two switches will be similar. Expressions for the DC components of the currents in switches I_{0SW} of the generators are obtained by expanding the pulses of these currents in a Fourier series. Similarly, expressions for determining the amplitudes of the first harmonics of the voltages across switches U_{1SW} can be derived. In this case, we will assume that $Z_L \neq R_L$, which corresponds to the operation of two generators on a complex load (for the special case of a matched resistive load $Z_L = R_L$, it will be necessary to substitute $X_L = 0$ and $\chi = 0$ into the resulting relations).

The DC component of the current pulses in the switches is determined as follows:

$$I_{0SW} = 1/\pi \int_{-\pi/2\pm\varphi}^{\pi/2\pm\varphi} I_m \cos(\omega t + \chi) d\omega t\,, \tag{1}$$

Where I_m is the amplitude of the first harmonic of the load current (defined below).

After integrating (1), we obtain the desired expression for I_{0SW}.

$$I_{0SW} = \frac{I_m \cos(\chi \pm \varphi)}{\pi}. \tag{2}$$

The amplitude of the first harmonic contained in a rectangular pulse $u_{G1}(t)$ with a peak-to-peak amplitude E is determined as follows:

$$U^*_{G1i} = 1/\pi \int_{-\pi/2}^{\pi/2} u_{Gi}(t)\cos(\omega t)dt + 1/\pi \int_{-\pi/2}^{\pi/2} u_{Gi}(t)\sin(\omega t)dt\,, \tag{3}$$

$$U^*_{G1i} = 2\frac{E}{\pi}(\cos\varphi \pm J\sin\varphi)\,. \tag{4}$$

The "plus" sign in formulas (2) and (4) corresponds to switch SW1.1, and the "minus" sign corresponds to switch SW2.2.

As can be seen from (4), the amplitude of the first harmonic of the generator voltage is constant and independent of phase shifts, which becomes evident from an analysis of the time dependences of the voltages on the switches (see Fig. 4). At the same time, as can be seen from (2), the magnitudes of the DC components of the currents in the switches of different generators depend differently on the phase shift due to the complex load mismatch χ and, in general, are not equal in magnitude. This important circumstance will be discussed in more detail below in Section 7.

Expressions for voltage and current:

$$U_L = 4\frac{E}{\pi}\cos\varphi, \tag{5}$$

$$I_L^* = \left(4E\cos\varphi \bullet e^{-j\chi}\right) / \pi\sqrt{\left[\left(R_L + 2r_{sat}\right)^2 + X_L^2\right]}, \tag{6}$$

$$I_m = \left(4E\cos\varphi\right) / \pi\sqrt{\left[\left(R_L + 2r_{sat}\right)^2 + X_L^2\right]}. \tag{7}$$

Output power:

$$P_L = \left(8E^2\cos^2\varphi \bullet R_L\right) / \pi^2\left[\left(R_L + 2r_{sat}\right)^2 + X_L^2\right]. \tag{8}$$

Active power loss (per transistor):

$$P_{r_{sat}} = \left(8E^2\cos^2\varphi \bullet r_{sat}\right) / \pi^2\left[\left(R_L + 2r_{sat}\right)^2 + X_L^2\right]. \tag{9}$$

Voltage amplitude at the transistor saturation resistance:

$$U_{r_{sart}} = \left(4E\ \cos\ \varphi \bullet r_{sat}\right) / \pi\ \sqrt{\left[\left(R_L + 2r_{sat}\right)^2 + X_L^2\right]}. \tag{10}$$

The constant component of the currents in the switches, substituting (7) into (2):

$$I_{0SW} = \left(4E\cos\varphi \bullet \cos(\chi \pm \varphi)\right) / \pi^2\sqrt{\left[\left(R_L + 2r_{sat}\right)^2 + X_L^2\right]}. \tag{11}$$

Power consumed from the power supply:

$$\begin{aligned} P_0 &= 2E(I_{0SW1.1} + I_{0SW2.2}) = \\ &= \left(\left(4E^2\cos\varphi\right) / \pi^2\sqrt{\left[\left(R_L + 2r_{sat}\right)^2 + X_L^2\right]}\right) \times . \\ &\times \left(\cos(\chi + \varphi) + \cos(\chi - \varphi)\right) \end{aligned} \tag{12}$$

In case of resistive load:

$$P_0 = \left(8E^2\cos^2\varphi\right) / \pi^2\left(R_L + 2r_{sat}\right). \tag{13}$$

OPA output stage efficiency in the case of $Z_L = R_L$ and the commutation losses absence is determined from (3.8) and (3.13) as:

$$\eta = \frac{\mathrm{R}_L}{(\mathrm{R}_L + 2\cdot \mathrm{r}_{sat})} = \frac{1}{(1 + \frac{2\cdot \mathrm{r}_{sat}}{\mathrm{R}_L})} \tag{14}$$

Expression (14) differs from the expression that determines the efficiency of a single VMCD FL generator in [24] only by a factor of “2”. This is because the load current in the equivalent circuit in Figure 3 flows through two series-connected transistors (switches) with equal saturation resistances.

Thus, expressions (2), (4)...(14), describing currents, voltages and powers depending on the phase shift φ, make it possible to calculate the static modulation characteristics (SMC) of the OPA final stage, described by the equivalent circuit in Figure 3, and evaluate its energy performance.

6 Inverse Currents in the OPA Output Stage

When selecting transistors for VMCD FL switching generators, in addition to frequency limitations, it is important to consider that inverse currents flow through the transistors in OPA when the generators are out of phase. This section identifies the most dangerous point in the OPA output stage SMC, where the inverse current reaches its maximum value.

The ability of field-effect transistors to pass inverse currents significantly simplifies generators circuits with filter loads in the OPA output stages. At the same time, it is essential to be able to calculate the maximum value of these currents in order to select the appropriate transistors and ensure their safe operation.

As shown above, when two switching generators operate simultaneously in the OPA final stage, inversion sections appear in the switching current waveforms, with the maximum share of inversion current occurring when the generators operate in antiphase with a matched (resistive) load (see Fig. 5). At the same time, as the phase shift changes from 0 to 180 degrees, the amplitude of the currents (equal in magnitude to the load current amplitude) decreases according to the cosine law, according to (7), while the share of inversion current in the switches increases with increasing phase shift. Thus, the problem arises of finding the phase shift at which the maximum instantaneous value of inversion current is achieved, and then calculating this value.

Let us find the value of the phase angle φ for switch K2.2 in the equivalent circuit of Figure 3 for the case of the OPA operating with a matched load. Obviously, for the other three switches, the desired value will be the same. As can be seen from Figure 4, the inverse current reaches its maximum instantaneous value at the moment of time $\omega t = (\pi / 2) + \varphi$ and, accordingly, the current in the switch at this moment of time is equal to:

$$\mathrm{I}_{SW\,\frac{\pi}{2}+\varphi} = \mathrm{I}_{\mathrm{m}} \cdot \cos\left(\frac{\pi}{2}+\varphi\right). \quad (15)$$

Substituting the expression for the current amplitude (7) into (15) and assuming the load is matched, we obtain:

$$\mathrm{I}_{SW\,\frac{\pi}{2}+\varphi} = \frac{4 \cdot \mathrm{E} \cdot \cos\varphi \cdot \cos\left(\frac{\pi}{2}+\varphi\right)}{\pi^2 \cdot (\mathrm{R}_L + 2 \cdot \mathrm{r}_{sat})} = \frac{-2 \cdot \mathrm{E} \cdot \sin 2\varphi}{\pi^2 \cdot (\mathrm{R}_L + 2 \cdot \mathrm{r}_{sat})}. \quad (16)$$

Differentiating expression (16) with respect to φ and equating it to zero yields the expression

$$\frac{-4 \cdot \mathrm{E} \cdot \cos 2\varphi}{\pi^2 \cdot (\mathrm{R}_L + 2 \cdot \mathrm{r}_{sat})} = 0. \quad (17)$$

From the solution of which we find the value of the phase angle φ at which the inverse current reaches its maximum:

$$\varphi = \frac{\pi}{4}. \quad (18)$$

Taking the second derivative of expression (16) at this point and verifying that it is positive

$$\frac{8\cdot E\cdot\sin\frac{2\pi}{4}}{\pi^2\cdot(R_L+2\cdot r_{sat})}=\frac{8\cdot E}{\pi^2\cdot(R_L+2\cdot r_{sat})}>0, \quad (19)$$

we assume that we indeed have the current maximum.

Substituting (18) into (7), we obtain an expression for determining the maximum inverse current when the OPA operates with a matched load:

$$I_{INV_{max}}=\frac{2\cdot\sqrt{2}\cdot E}{\pi^2\cdot(R_L+2\cdot r_{sat})}. \quad (20)$$

Similarly, an expression can be derived for determining this value for the case of a complex load. Here it is necessary to take into account that the point of the minimum value of the current pulse will be shifted relative to this point in the case of a resistive load along the ωt axis by the value of the load phase χ and the current itself will have a phase shift of the same value (see diagrams in Fig. 6-8). Carrying out transformations similar to those described above, we obtain

$$\varphi=\frac{\pi}{4}-\chi. \quad (21)$$

Substituting (21) into expression (7), we can obtain an expression for I_{INVmax}. It should be noted that in the case of a complex load, this value turns out to be different for each of the two generators of the OPA final stage, depending on the sign of χ for each of them (see Fig. 6-8). As will be shown below (see Section 7), the emerging difference in the operating modes of channel generators is not dangerous if the transistors (MOSFET or GaN HEMT) are correctly selected for the maximum power mode for a given mismatch of the OPA total load.

7 Features of OPA Operation with Large Load Mismatches

Let's return to the operating mode of the OPA output stage, described by expression (11) and illustrated in Figure 8 when, due to a reactive load mismatch, the currents consumed by the generators are unequal. Using (11), normalized (relative to the point φ=0) dependences of these currents on the value of 2φ are plotted (Fig. 9) for a fixed value of $\chi=\pi/4$. These theoretical curves correspond to the special case considered above, which is illustrated by the diagrams in Figure 8. In this case, the voltage of one of the generators is in-phase with the load current, while that of the other is orthogonal to it.

At 2φ=0, the currents are equal, and with increasing φ, the consumed current of the second generator (for which the sign of φ coincides with the sign of χ) begins to grow and reaches a maximum at the point 2φ=45^0, where $2\varphi=\chi \; or \; \varphi=\chi/2$, after which it begins to fall. The consumed current of the first generator, for which the sign of φ is opposite to the sign of χ, decreases monotonically over the entire interval from 2φ=0 to $2\varphi=\chi$. At 2φ=90^0 (i.e. when $\varphi=\chi$, the output current and voltage of the second generator are in phase), the consumed current of the second generator takes the same value as at 2φ=0, which corresponds to operation on a purely resistive load, and the consumed current of the first generator becomes zero, which corresponds to its operation on a purely reactive load. In this case, for the second generator $\chi-\varphi=0$, and for the first, $\chi-\varphi=90^0$, which makes the active component of the reduced load impedance and the consumed current of the first generator zero according to expression (11). With a further increase in φ, the consumed current for the second generator becomes negative and the generator operates on a load whose resistive part is negative. The consumed power for the first generator also becomes negative in this case, i.e. the generator recuperates part of the total oscillatory energy into the power source. Due to this, the efficiency of the OPA, defined as the ratio of the output power to the consumed power, will be close to unity throughout the entire SMC (from 2φ=0 to 2φ=180^0).

Then, with increasing φ, the negative consumed current of the first generator initially increases in magnitude, reaching its maximum at $2\varphi = 3\chi / 2$, $(2\varphi = 135^0)$, and then decreases and turns to zero at $2\varphi=180^0$. The consumed current of the second generator in the section from $2\varphi=90^0$ to $2\varphi=180^0$ monotonically decreases to zero. The theoretical dependencies plotted in Figure 9 have been experimentally confirmed.

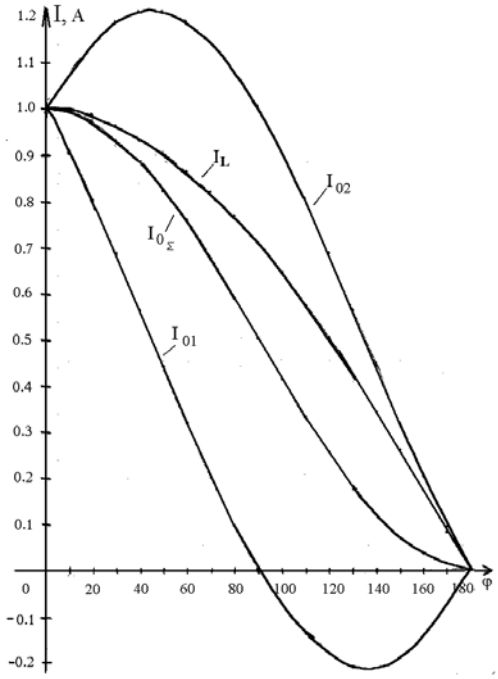


Figure 9. Theoretical dependencies of generator currents

As can be seen from Figure 9, the total current consumed by both generators has a maximum at the common-mode point (φ = 0) and decreases monotonically with increasing phase shift. It should be noted that the transistor pulse currents (in the form of half-wave cosine wave sections with different phases) have identical maximum values for all four transistors of both channels, since a common load current flows through the transistors. The load current amplitude is determined by the supply voltage E, the phase shift of the channel signals φ, and the absolute value of the load impedance, according to (7). Accordingly, all four transistors of the OPA output stage are, from a safety standpoint, in completely identical conditions: they have identical maximum currents and voltages at the drains, identical dissipated powers (and even identical ratios between the commutative and resistive components of power loss).

At the same time, when OPA designing, it is of course necessary to take into account the possible magnitude of the load mismatch (antenna-feeder path) [27]. As follows from Figure 9, the maximum transistor loading occurs during in-phase operation of the channels (φ =0), when the output, consumed, and dissipated powers in the transistors are at their maximum; at this point, the transistor pulse currents are also at their maximum. Accordingly, the calculation of the OPA output stage mode, ensuring the safe operation of the active devices, can be carried out using traditional [24] methods.

Conclusions

An analysis of the channel generators operating characteristics in outphasing high-efficiency radio-frequency power amplifiers demonstrated the advantage of using Voltage Mode Class D (VMCD) switching generators with filter loads (FL) based on field-effect (FET) transistors – MOSFET, VDMOS, LDMOS, and GaN HEMT. Based on equivalent circuits and currents and voltages diagrams, basic expressions were derived

for calculating output power, power loss, efficiency, and maximum currents when operating with matched and mismatched (complex) loads. The presence of inverse currents was demonstrated, and their maximum values, achievable with a 45-degree phase shift, were determined, which are necessary for component selection. Further work will focus on accounting for switching losses.

REFERENCES

[1] H. Chireix, “High power outphasing modulation,” *Proc. IRE*. 1935, no. 23, pp. 1370-1392.

[2] S.A. Hetzel, A. Bateman, J.P. McGeehan, “Linc transmitter,” *Electronics letters*. 9th May 1991. Vol. 27, no. 10, pp. 133-137.

[3] Q. F. Ngo and O. V. Varlamov, “Outphasing Transmitter Circuit with Switching Generators Direct Summation: Static Mode Analysis,” *2025 Wave Electronics and its Application in Information and Telecommunication Systems (WECONF)*, St. Petersburg, Russian Federation, 2025, pp. 1–9, doi: 10.1109/WECONF65186.2025.11017168.

[4] Q. F. Ngo, N. S. Bekushev, V. N. Gromorushkin, O. V. Varlamov, “Outphasing transmitter circuit with switching generators direct summation design features,” *T-Comm*, 2025, vol. 19, no. 2, pp. 4–14. DOI: 10.36724/2072-8735-2025-19-2-4–14.

[5] V. N. Gromorushkin and O. V. Varlamov, “Dynamic Operation Modes of Outphasing Transmitters with Switching Generators Direct Summation,” *2025 Wave Electronics and its Application in Information and Telecommunication Systems (WECONF)*, St. Petersburg, Russian Federation, 2025, pp. 1–7, doi: 10.1109/WECONF65186.2025.11017153.

[6] O. V. Varlamov and V. N. Gromorushkin, “Mismatched Load Operation of Outphasing Transmitters with Switching Generators Direct Summation,” *2025 Wave Electronics and its Application in Information and Telecommunication Systems (WECONF)*, St. Petersburg, Russian Federation, 2025, pp. 1–5, doi: 10.1109/WECONF65186.2025.11017139.

[7] Q.F. Ngo, V.N. Gromorushkin, O.V. Varlamov, “Outphasing transmitters with switching generators direct summation: dynamic modes and mismatched load operation,” *T-Comm*, 2025, vol. 19, no. 3, pp. 13–23. DOI: 10.36724/2072-8735-2025-19-3-13–23.

[8] O. V. Varlamov, “Experimental Study of a Synchronous DVB-T2 Network in the Yaroslavl Region. Problems with Some Manufacturers' Receivers,” *2020 International Conference on Engineering Management of Communication and Technology (EMCTECH)*, Vienna, Austria, 2020, pp. 1 - 4, Doi: 10.1109/EMCTECH49634.2020.9261562.

[9] O. Varlamov, V. Varlamov, and A. Dolgopyatova, "Digital Radio Broadcasting Network in the Arctic Region", *2019 24th Conference of Open Innovations Association (FRUCT)*, Moscow, Russia, 2019, pp. 457-462. DOI: 10.23919/FRUCT.2019.8711933.

[10] O. V. Varlamov, and A. A. Bychkova, "Basis of Technical Design and Development a Single-Frequency DRM Digital Broadcasting Network for Venezuela", *2021 Systems of Signal Synchronization, Generating and Processing in Telecommunications (SYNCHROINFO*, 2021, pp. 1-7, doi: 10.1109/SYNCHROINFO51390.2021.9488396.

[11] A.A. Losev, “Development and analysis of technical solutions for a satellite repeater power amplifier built using the outphasing method,” Ph.D. Thesis, MTUCI, Moscow, Russia, 2017.

[12] A. Pastukh, V. Tikhvinskiy, S. Dymkova, and O. Varlamov, “Challenges of Using the L-Band and S-Band for Direct-to-Cellular Satellite 5G-6G NTN Systems,” *Technologies*, vol. 11, no. 4, p. 110, Aug. 2023, Doi: 10.3390/technologies11040110.

[13] V. Tikhvinskiy, A. Pastukh, S. Dymkova, O. Varlamov, “Compatibility Analysis Between RedCap Non-Public Networks and 5G NR in TDD FR1 and FR2 Bands,” *Inventions*, 2025. 10 (1), 12. https://doi.org/10.3390/inventions10010012.

[14] O. Varlamov, D. C. Nguyen, and A. Grebennikov, “Broadband and Efficient Envelope Amplifier for Envelope Elimination and Restoration/Envelope Tracking Higher-Efficiency Power Amplifiers,” *Sensor*s, vol. 22, no. 23, p. 9173, Nov. 2022, Doi: 10.3390/s22239173.

[15] O.V. Varlamov, “Powerful broadband DC amplifiers for modulation path of transmitters with separate amplification,” *T-Comm*. 2022. vol. 16, no.11, pp. 4-14. DOI: 10.36724/2072-8735-2022-16-11-4-14

[16] Nguyen, Dang Canh, Victor N. Gromorushkin, and Oleg Varlamov. 2023. “Theoretical Comparison of Different Envelope Elimination and Restoration Transmitter PWM Modulator Configurations to Expand the Possible Antenna Mismatch,” *Sensors* 23, no. 23 : 9466. https://doi.org/10.3390/s23239466.

[17] D.C. Nguyen, O.V. Varlamov, "Simulation model for studying the operation of switching mode envelope elimination and restoration RF power amplifiers for a narrow-band load", *H&ES Research*. 2022. Vol. 14. No 2, pp. 10-18. doi: 10.36724/2409-5419-2022-14-2-10-18.

[18] O.V. Varlamov, D.C. Nguyen, S.E. Grychkin, “Combination of synthetic high-performance RF amplification techniques,” *T-Comm*. 2021. vol. 15, no.9, pp. 11-16. DOI: 10.36724/2072-8735-2021-15-9-11-16.

[19] Q.F. Ngo, O.V. Varlamov, “Engineering and technical principles of highly effective linear radio transmitters construction for HF manpack radios,” *T-Comm*, 2024, vol. 18, no. 4, pp. 4–14. DOI: 10.36724/2072-8735-2024-18-4-4-14.

[20] Q. F. Ngo and O. V. Varlamov, "Methods for Increasing the Efficiency of Amplitude-Phase Modulated Signals Power Amplifiers," *2024 Systems of Signals Generating and Processing in the Field of on Board Communications*, Moscow, Russian Federation, 2024, pp. 1-8, doi: 10.1109/IEEECONF60226.2024.10496778.

[21] O.V. Varlamov, V.N. Gromorushkin, V.B. Kozyrev, A.V. Melanin, “Addition of the power outputs from push-pull voltage-switching oscillators having a resistive load,” *Radioelectronics and Communications Systems*. 1989, vol. 32. no 7, pp. 30-35.

[22] R.Yu. Ivanyushkin, “Research and development of a high-frequency path of a radio broadcasting MF transmitter built using the outphasing method,” Ph.D. Thesis / Moscow Technical University of Communications and Informatics. Moscow, 2001.

[23] V.B. Kozyrev, V.G. Lavrushenkov, V.P. Leonov, “Transistor generators of harmonic oscillations in the switching mode,” Moscow: Radio and communication, 1985.

[24] O. V. Varlamov and V. N. Gromorushkin, "Class D Switching Power Amplifier with a Filter under Load Mismatch Conditions", *2020 Wave Electronics and its Application in Information and Telecommunication Systems (WECONF)*, Saint-Petersburg, Russia, 2020, pp. 1-6, doi: 10.1109/WECONF48837.2020.9131508.

[25] Q. F. Ngo and O. V. Varlamov, "GaN HEMT Transistors Application Features in Outphasing Transmitters," *2026 Wave Electronics and its Application in Information and Telecommunication Systems (WECONF)*, St. Petersburg, Russian Federation, 2026, pp. 1-6, doi: 10.1109/WECONF69969.2026.11553787.

[26] N. S. Bekushev, Q. F. Ngo and O. V. Varlamov, "Design Methods of Outphasing Transmitter Exciter for Lab Prototyping," *2026 Systems of Signals Generating and Processing in the Field of on Board Communications*, Moscow, Russian Federation, 2026, pp. 1-8, doi: 10.1109/IEEECONF68869.2026.11461172.

[27] O. V. Varlamov, "Power Capacity of HF Automatic Antenna Tuner Switched by PIN Diodes under Load Mismatch Conditions", *2020 Systems of Signal Synchronization, Generating and Processing in Telecommunications (SYNCHROINFO)*, Svetlogorsk, Russia, 2020, pp. 1-5, doi: 10.1109/SYNCHROINFO49631.2020.9166046.

DEVELOPMENT OF A MACHINE LEARNING ALGORITHM FOR RISK ASSESSMENT IN INTERNET OF THINGS (IOT) SYSTEMS

Happy Ondobo Steve [1], Vitaly B. Kreindelin [2]

[1] University of Buea, Buea, Cameroon, happionodobo@gmail.com
[2] MTUCI, Moscow, Russia, vitkrend@gmail.com

ABSTRACT

Machine learning offers a promising approach to automating risk assessment by analyzing patterns in network traffic. This work builds upon existing anomaly and intrusion detection methods while addressing the lack of IoT-specific risk assessment frameworks that incorporate both the likelihood of occurrence and the impact of security incidents. The rapid expansion of the Internet of Things (IoT) has created significant challenges for ensuring the security and resilience of interconnected devices. Traditional security approaches are insufficient to protect against dynamic, evolving cyber threats. This paper proposes an IoT risk assessment framework based on machine learning, integrating both supervised and unsupervised techniques to identify, classify, and mitigate threats. The framework evaluates risks based on likelihood and impact, providing a scalable and adaptive solution suitable for modern IoT networks.

DOI: 10.36724/2664-066X-2026-12-4-32-38

Received: 05.04.2026
Accepted: 17.06.2026

Citation: Happy Ondobo Steve, Vitaly B. Kreindelin, "Development of a machine learning algorithm for risk assessment in Internet of Things (IoT) systems," *Synchroinfo Journal* **2026**, vol. 12, no. 4, pp. 32-38.

KEYWORDS: *IoT security, risk assessment, machine learning, anomaly detection, cybersecurity.*

Licensee IRIS, Vienna, Austria.

This article is an open access article distributed under the terms and conditions of the Creative Commons Attribution (CC BY) license (https://creativecommons.org/licenses/by/4.0/).

Copyright: © 2026 by the authors.

Introduction

The Internet of Things (IoT) connects billions of devices worldwide, transforming sectors such as healthcare, manufacturing, transportation, and smart cities. However, heterogeneity, limited computational power, and a lack of robust security protocols render IoT devices vulnerable to cyberattacks, as highlighted in the OWASP IoT Top Ten Security Threats [1].

Key challenges include the constrained resources of these devices, heterogeneous architectures, and inadequate security protocols. Such vulnerabilities expose IoT environments to risks including malware, denial-of-service attacks (e.g., the Mirai botnet [2]), data breaches, and advanced persistent threats.

Risk assessment is a critical step in securing the Internet of Things, as it enables system administrators to prioritize threats based on their severity. Traditional methods rely heavily on static rules [3]. Machine learning (ML) offers a promising approach to automating risk assessment by analyzing patterns within network traffic [4, 5].

This work builds upon existing anomaly and intrusion detection methods while addressing the current lack of IoT-specific risk assessment frameworks that incorporate both the likelihood of occurrence and the impact of security incidents [6].

Several studies have explored the integration of machine learning into IoT security. Signature-based detection methods are effective against known threats but fail to address unknown ones. Behavioral and anomaly-based detection methods improve detection capabilities, yet they are prone to a high rate of false positives [4]. Platforms such as Endpoint Detection and Response (EDR), Extended Detection and Response (XDR), and Security Information and Event Management (SIEM) provide monitoring and detection, but – as noted by NIST – they lack configurations specifically tailored to IoT environments [7].

Recent research highlights the potential of machine learning algorithms, including Random Forest, Support Vector Machines, and Neural Networks, for detecting IoT anomalies. For instance, the N-BaIoT study demonstrated the effectiveness of deep autoencoders in identifying botnet attacks [5], while hybrid deep learning models have shown promise for intelligent threat detection [8]. Nevertheless, few studies focus specifically on risk assessment that incorporates both the probability of an attack and its potential impact on IoT systems [6]. Furthermore, emerging technologies like Federated Learning offer privacy-preserving solutions, enabling collaborative model training without the need to share raw data [9].

Statement of the problem

The purpose of this paper is to develop and evaluate an algorithm for risk assessment in IoT systems based on machine learning. The algorithm must be able to:

- Rel ably detect both known and previously unknown cyber threats.
- Reduce the number of false positives that can overwhelm system administrators.
- Create a meaningful risk assessment that combines the likelihood of an attack and its potential consequences.
- Efficiently scale to support large and complex IoT environments.

Addressing these issues will allow us to focus on the most serious risks, improve system resilience, and reduce the overall vulnerability of IoT ecosystems, consistent with the risk management goals of the NIST Cybersecurity Framework [10].

Let's consider the proposed methodology and algorithm development.

Methodology

The proposed framework operates in three stages: data preprocessing, threat detection, and risk assessment. Let us examine these stages in more detail (Fig. 1).

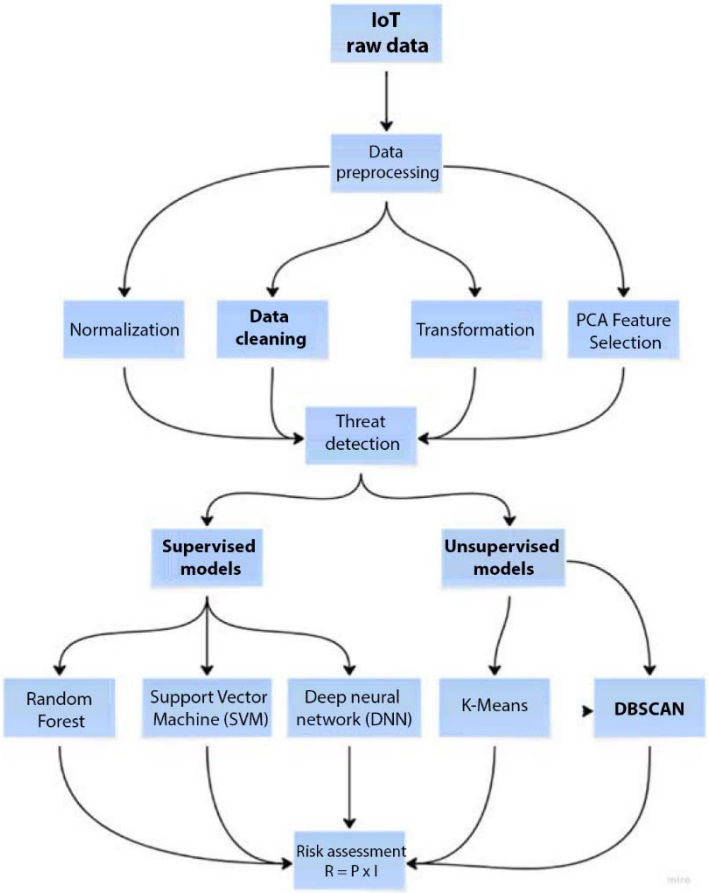


Fig. 1. Overall architecture of an IoT risk assessment system

1. Data Preprocessing: IoT traffic and device logs are normalized, cleaned, and transformed into structured features. Feature selection methods, such as Principal Component Analysis (PCA), are applied to reduce dimensionality. To ensure relevance, we will utilize datasets specifically designed for IoT security research, such as the IoT Network Intrusion Dataset [11].

2. Threat Detection: Both supervised and unsupervised models are deployed, following a hybrid approach outlined in recent research [8]. Supervised classifiers (Random Forest, Support Vector Machines, Deep Neural Networks) detect known threats using labeled datasets. Unsupervised clustering (K-Means, DBSCAN) identifies anomalies and emerging risks without prior labeling [5].

3. Risk Assessment (R = P × I) is calculated using specific metrics for both probability (P) and impact (I). This two-factor assessment enables system administrators to prioritize mitigation efforts – moving beyond simple detection toward actionable analysis, as advocated by industry leaders such as Palo Alto Networks Unit 42 [12].

• Probability (P): This represents the confidence level of our machine learning model's prediction, scaled from 0.0 to 1.0. For example, if a Random Forest classifier is 95% confident that an event is a DDoS attack, then P = 0.95.

• Impact (I): This is a predefined score (e.g., from 1 to 10) based on the type of threat and the criticality of the target device. For example:

– malw re on a smart light bulb: Low Impact (I = 2).

– data exfiltr tion from the health monitoring system: High impact (I = 9).

Calculation example

A brute-force attack attempt (P = 0.88) on a critical industrial control sensor (I = 10) would result in a risk score of R = 0.88 × 10 = 8.8 (high risk). The same attack on a non-critical environmental sensor (I = 3) would yield R = 0.88 × 3 = 2.64 (low risk). Such a detailed assessment enables administrators to effectively prioritize their responses.

Figure 1 illustrates the overall architecture of the IoT risk assessment system, while Figure 2 details the machine learning workflow. The system architecture is designed as follows:

1. Data Source Layer: Various IoT devices (sensors, actuators, cameras) generate raw network traffic and system logs.

2. Data Collection and Preprocessing Layer: A central gateway or cloud server collects the raw data, which is then normalized, cleaned, and structured for analysis.

3. ML Core Engine: The preprocessed data is fed into a hybrid machine learning model (combining supervised and unsupervised algorithms) to detect threats and calculate the probability (P).

4. Risk and Decision-Making Layer: The output from the machine learning engine is combined with impact metrics (I) from the device registry to calculate the final risk score (R = P × I).

5. Action and Visualization Layer: Prioritized risks and automated mitigation actions (e.g., isolating a device or blocking an IP address) are presented to administrators via a security dashboard for final decision-making.

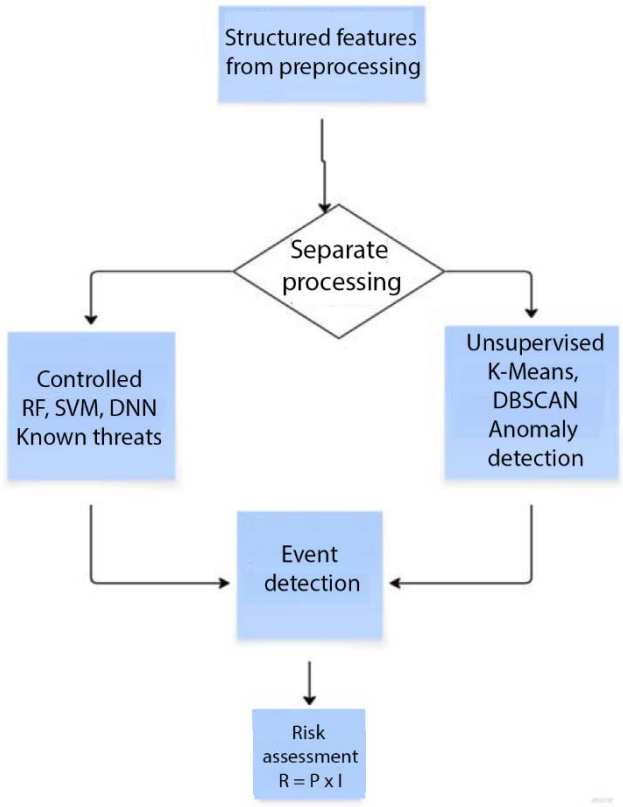


Fig. 2. Workflow of a machine learning algorithm

The IoT risk assessment algorithm is described as follows:

1. Input of pre-pr essed IoT data.

2. Applicati of feature selection for dimensionality reduction.

3. Training of supervised machine learning models using labeled datasets (e.g., NSL-KDD, CICIDS).

4. Execution of un pervised clustering to identify new risks.

5. Generation of a r k score for each event.

6. Provision of recommendations (e.g., isolating a device, enforcing encryption, or activating firewall rules).

Dataset and experimental design

Benchmark datasets for IoT and cybersecurity will be used for evaluation:

• NS -KDD – an intrusion detection dataset containing 125,000 records.

• CIC DS2017 – realistic traffic data including IoT botnet attacks (>3 million records).

• IoT-23 – a specialized dataset for IoT-related malware [11]. Table 1 presents the datasets and their characteristics.

Table 1

Datasets

Dataset	Description	Size
NSL-KDD	Dataset for classical intrusion detection	125,000 records
CICIDS2017	Realistic IoT traffic with botnet attacks	3M+ records
Internet of Things-23	Dedicated dataset on IoT malware traffic	20+ large pcap files

Expected results

Expected performance metrics are shown in Table 2. Deep neural networks are expected to outperform traditional machine learning methods, achieving an accuracy of up to 95%, which is consistent with the findings of Pajouh et al. [8].

Random Forest offers a balance between accuracy and interpretability, while unsupervised methods provide the additional capability to detect new, previously unseen threats. Table 2 presents the accuracy, precision/recall, and F1-score metrics for the models evaluated.

Table 2

Model metrics

Model	Accuracy	Memory Accuracy/Completeness	F1 account
Random forest	93%	91% / 90%	92%
Support Vector Machine	89%	88% / 87%	88%
Deep neural network	95%	94% / 93%	94%
K-means (unsupervised)	-	Detection level 70%	-

Our expected results indicate that a hybrid approach outperforms the use of a single model. The high accuracy of a deep neural network in identifying known threats, combined with the novel threat-detection capability of K-Means, creates a robust, layered defense.

• Comparison with related work: Unlike traditional SIEM systems, which rely on static rules [3], our framework dynamically adapts to new data. Furthermore, while many existing machine learning solutions focus solely on detection [5], our integration of impact-based risk assessment provides a direct, actionable output for system operators, addressing a key challenge in IoT security management [5, 12-15].

• Interpretation of unsupervised results: A lower detection rate (70%) is expected for the unsupervised model, as anomaly detection is inherently a complex task. Its value lies not in perfect accuracy, but in its ability to flag previously unknown attack patterns that supervised models might overlook, thereby providing an essential early-warning system.

Conclusion

This paper presents a comprehensive machine learning-based platform for assessing risks in the Internet of Things (IoT). By combining supervised and unsupervised learning methods, the framework is capable of detecting both known and novel threats while providing actionable risk assessments. The system emphasizes scalability and adaptability – qualities that are crucial in the rapidly evolving IoT landscape.

As part of our future work, we plan to:

• Deploy and test the system on a physical testbed consisting of actual IoT devices.

• Implement federated learning techniques [12] to train models across distributed devices without centralizing sensitive data.

• Develop a user-friendly dashboard that visualizes risk assessments and provides explanations for security teams.

REFERENCES

[1] OWASP Foundation. IoT Top Ten Security Threats. 2018.

[2] R. Sommer, V. Paxson, “Outside the Closed World: On Using Machine Learning for Network Intrusion Detection,” In *2010 IEEE Symposium on Security and Privacy*. 2010.

[3] D. Smith, et al., “Cybersecurity Challenges in IoT: A Risk-B ased Approach,” *Journal of Cybersecurity*. 2023.

[4] A. Dow, “Machine Learning for IoT Security: Techniques and Applications,” *IEEE Transactions on IoT*. 2022.

[5] Y. Meidan, M. Bohadana, Y. Mathov, et al., “N-BaIoT – Network-Based Detection of IoT Botnet Attacks Using Deep Autoencoders,” *IEEE Pervasive Computing*. 2018. https://ieeexplore.ieee.org/document/8324144.

[6] S. Sicari, A. Rizzardi, L. A. Grieco, A. Coen-Porisini, “A Multidimensional Robust and Adaptive Framework for IoT Risk Assessment,” *Computer Communications*. 2020. https://www.sciencedirect.com/science/article/abs/pii/S0140366419318341

[7] National Institute of Standards and Technology (NIST). Considerations for Managing Internet of Things (IoT) Cybersecurity and Privacy Risks (NISTIR 8228). 2019. https://nvlpubs.nist.gov/nistpubs/ir/2019/NIST.IR.8228.pdf

[8] H. H. Pajouh, R. Javidan, R. Khayami, et al., “A Hybrid Deep Learning Model for Intelligent Threat Detection in IoT Systems,” *IEEE Access*. 2022. https://ieeexplore.ieee.org/document/9743117

[9] N. T. Nguyen, D. T. Hoang, D. N. Nguyen, et al., Federated Learning for IoT Security: A Case Study on Botnet Attack Detection,” *IEEE Transactions on Industrial Informatics*. 2023. https://ieeexplore.ieee.org/abstract/document/10020347

[10] National Institute of Standards and Technology (NIST). Cybersecurity Framework (Version 1.1). 2018.

[11] A. Alsaeedi, M. M. Rizvi, K. A. Al-Shqeer, “IoT Network Intrusion Dataset,” *MDPI Data*, 2019, no. 4(4), 141. https://www.mdpi.com/2306-5729/4/4/141

[12] Palo Alto Networks (Unit 42), The Role of AI and ML in IoT Security. 2023. https://unit42.paloaltonetworks.com/ai-machine-learning-iot-security/

13. V. B. Kreindelin, N. A. Legkov, “Protection of Authentication Data for Websites and Web Applications,” *Telecommunications and Information Technologies*. 2022. Vol. 9, No. 1, pp. 6-10.

[14] V. B. Kreindelin, A. D. Avidzba, “Encryption wi-fi protected access,” Technologies of the information society: XI International Industry Scientific and Technical Conference: collection of proceedings, Moscow, March 15-16, 2017. Moscow: Media Publisher, 2017. P. 294.

[15] V. B. Kreindelin, G. A. Vakhromeev, “Most Effective Machine Learning Algorithms for Risk-Based Authentication Systems,” *Telecommunications and Information Technologies*. 2024. Vol. 11, No. 1, pp. 87-92.

SYNCHROINFO JOURNAL

www.media-publisher.eu/synchroinfo-journal

INTERACTION BETWEEN DETECTION AND TRACKING UNITS FOR SIGNAL FREQUENCIES AND TIME DELAYS (ILLUSTRATED BY A SATELLITE RADIO SYSTEM)

Sy. D. Vu [1]

[1] Le Quy Don Technical University, HaNoi, VietNam
daovs@viettel.com.vn

ABSTRACT

In many instances – for example, in satellite radionavigation systems – INFO components are absent, and the communication channel carries only periodic SS signals. We shall examine a more complex type of noise-like signal (NLS) that employs composite pseudorandom sequences (PRS) for its generation. The purpose of this article is to examine the integrated operation of devices designed for the detection (search) of weak, noise-like signals and the tracking of their parameter variations – while maintaining a specified final estimation accuracy – within a quasi-coherent receiver employing a multi-stage, parallel-sequential detection and synchronization procedure. Furthermore, aims to develop and analyze a unified quality criterion for synchronization, specifically in the context of a satellite radio system.

DOI: 10.36724/2664-066X-2026-12-4-39-67

Received: 05.04.2026
Accepted: 17.06.2026

Citation: Sy. D. Vu, "Interaction between detection and tracking units for signal frequencies and time delays (illustrated by a satellite radio system)," *Synchroinfo Journal* **2026**, vol. 12, no. 4, pp. 39-67.

Licensee IRIS, Vienna, Austria.

This article is an open access article distributed under the terms and conditions of the Creative Commons Attribution (CC BY) license (https://creativecommons.org/licenses/by/4.0/).

Copyright: © 2026 by the authors.

KEYWORDS: *signal frequencies, time-delay parameters, satellite radio system, noise-like signals.*

Introduction

The estimation of frequency and time-delay parameters for signals is typically performed within a synchronization channel (SC), using either dedicated synchronization signals (SS) or the information-bearing signals (INFO) of a digital data transmission system. In the case of noise-like signals, the SS components are generally transmitted within the same frequency band as the INFO components and are generated based on periodically repeating pseudorandom sequences (PRS) [1-6]. The allocation of radio channel power between the SS and INFO components can be optimized with regard to the overall efficiency of the radio system [7, 8]. In this scenario, the INFO components – transmitted alongside the SS components within the shared frequency band – can be viewed as additional noise-like interference, significantly exceeding the power of the useful noise-like signal serving as the SS component. In many instances – for example, in satellite radionavigation systems – INFO components are absent, and the communication channel carries only periodic SS signals. The findings presented in this section have been published by the author in [9, 10].

General principles for establishing a synchronization channel in a satellite radio system

It should be noted that the portion of the synchronization channel consisting of a set of correlators (or matched filters) and an energy accumulator can also operate using INFO signals – which may have higher power than the SS signals – since, in a digital communication channel, the set of such INFO signals is always finite and periodic in time. In contrast, phase-locked loops (PLL) and automatic frequency control (AFC) systems can only operate using SS signals [11].

In the following, we will consider periodic binary phase-shift keyed (PSK) signals as synchronization (SS) signals, which, over the duration of their repetition period T_s, are described as

$$s(t) = \sum_{i=0}^{N_э-1} d_i S_0(t - iT_э)\cos(2\pi f_0 t), \quad (1)$$

where N_e – repetition period of a binary pseudorandom sequence (PRS), $d_i \in \{-1,1\}$ – its elementary symbols, $i = 1, \dots, N_e$ – PSP symbol number, $S_0(t)$ – shape function of an elementary pulse of duration T_e, f_0 – its carrier frequency.

The bandwidth occupied by a radio system using noise-like signals is approximately equal to their clock frequency $f_T = 1/T_e$, In various satellite radio systems, this value can range from a few units to tens – and potentially hundreds – of MHz.

Therefore, we shall also examine a more complex type of noise-like signal (NLS) that employs composite pseudorandom sequences (PRS) for its generation. In this configuration, the primary PRS is binary; however, over the duration T_s, the frequency of the corresponding binary phase-shift keyed (PSK) signal shifts repeatedly – governed by a modulating multi-valued PRS – to one of several frequency positions. Thus, we consider signals characterized by discrete frequency hopping, where the phase remains continuous during the phase-shift keying process. Hereafter, we will refer to these as "discrete-frequency phase-shift keyed signals" (DF-PSK NLS). Multi-valued PRSs, such as quaternary Welti E-sequences, can be used to facilitate hopping across four distinct frequency positions [12].

Consequently, the generation of DF-PSK NLS involves the use of binary-quaternary PRSs. It should be noted that, in the receiver, the converter used to generate the second intermediate frequency employs a single local oscillator; this ensures phase continuity across the various frequency segments of the incoming binary PSK signal. Furthermore, to maintain this phase continuity, each of the four frequencies is chosen to be an integer multiple of the signal's clock frequency, f_T. In the transmitter, the initial phases of the elementary pulses of the binary PRS are also set to be identical. As a result, the frequency-shifted segments of the binary PRS share the same initial phases, which are determined by the phase shift of the receiver's local oscillator signal relative to the incoming signal.

The purpose of this section is to examine the integrated operation of devices designed for the detection (search) of weak, noise-like signals and the tracking of their parameter variations – while maintaining a specified final estimation accuracy – within a quasi-coherent receiver employing a multi-stage, parallel-sequential detection and synchronization procedure. Furthermore, this section aims to develop and analyze a unified quality criterion for synchronization, specifically in the context of a satellite radio system.

Generalized block diagram of a synchronization channel for weak noise-like signals

In accordance with the above, it is assumed that the CS initially detects and distinguishes all noise-like CLs simultaneously present at the receiver input, that is, both different CLs in shape, and all their copies, mismatched in frequency and time delay. In this case, the receiver has a bank of possible SLS forms that may appear at its input. For this purpose, a SIS detection device (USIS) is used, which is part of the CS, the structural diagram of which is shown in Figure 1. Thus, the SIS detects and makes an initial rough estimate of the parameters (frequency and time delay) of all noise-like SIS simultaneously present at the receiver input.

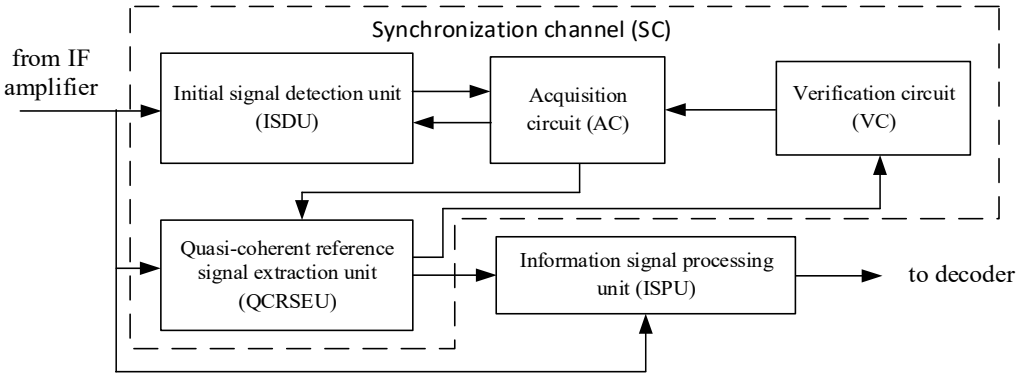


Fig. 1. Generalized block diagram of a receiver for a set of noise-like signals

Information regarding the approximate parameter values of all detected signals is fed into the quasi-coherent reference signal extraction unit (QCRSEU) via an acquisition circuit (AC) (Fig. 1). Within the QCRSEU, more precise estimation and tracking of the time delays and carrier frequencies of all signals detected by the initial signal detection unit (ISDU) are performed. A verification circuit (VC) is employed within the relevant units to identify the tracking status. It triggers a re-initiation of the signal detection procedure if a signal was detected by the ISDU but failed to be acquired by the QCRSEU, or if the tracking of its parameters is lost. Figure 1 also shows a coherent-type information signal processing unit (ISPU), as coherent reference information signals can be generated based on the output of the coherent system (CS).

A more detailed block diagram of a receiver for a set of noise-like signals (NLS) is presented in Figure 2. It shows that the NLS tracking unit consists of a set of phase-locked loops (PLLs) and a set of time-delay tracking loops (TLs), with each PLL interconnected with one of the TLs. Together, they perform joint tracking of the carrier frequency and time delay of one of the detected NLSs.

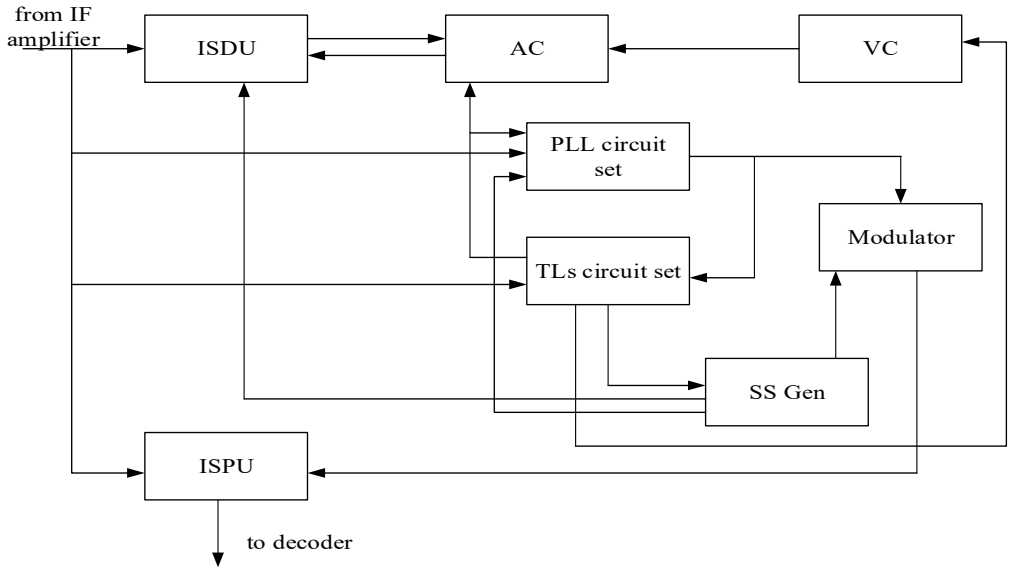


Fig. 2. Circuit diagram of a noise-like SLS receiver with PLL and autoreclose systems

Figure 2 also shows a reference synchronization signal generator (SS Gen), which is effectively part of the set of TLs and contains a library of all possible synchronization signals used by the tracking system. To configure the TLs to track the time delays of the detected NLSs, this generator produces reference signals corresponding only to those waveforms that were identified by the NLS detection unit. Thus, the synchronization of the reference signals produced by this generator is managed by the TLs; the ultimate result is the generation – within the SS Gen – of baseband copies of the received NLSs that are time-synchronized with them.

The library of synchronization signals held within the SS Gen is also used to program the NLS detection unit. Furthermore, these reference signals are used to generate reference information-bearing NLSs at the radio frequency (RF) within a modulator (M), facilitating the coherent processing of information signals. The carrier frequencies of the detected NLSs are supplied to the modulator from the outputs of the voltage-controlled oscillators (VCOs) located within the PLL circuits [13].

For frequency-hopped spread-spectrum signals with phase-shift keying (FHSS-PSK), the block diagram of the tracking system for a single received synchronization signal is shown in Figure 3.

In this case, the UVKOSIS (Wideband Coherent Signal Receiver) consists of one APC (Automatic Phase Control) circuit and four identical PLL (Phase-Locked Loop) circuits, each operating at its own intermediate frequency. The PLL and APC circuits operate with cross-coupling. The UOIS (Information Signal Processing Unit) operates based on the information-bearing signal (INF).

A separate, continuously repeating PN-PSK (pseudonoise phase-shift keyed) synchronization signal is used to synchronize the UVKOSIS. The UVKOSIS begins operation once a signal (SIS) is detected by the UOSIS (Signal Detection Unit); once the UVKOSIS achieves synchronization, the reception of useful information by the UOIS commences. Since the received signal is present at only one of the four frequencies at any given time, the noise immunity of the UVKOSIS and UOIS is enhanced – by improving the signal-to-noise ratio fourfold – as follows: once the PLL and APC circuits have achieved synchronization, gating pulses from a quaternary

E-sequence generator sequentially open one of the four corresponding switches (KI) for a duration equal to the length of the signal’s frequency segments.

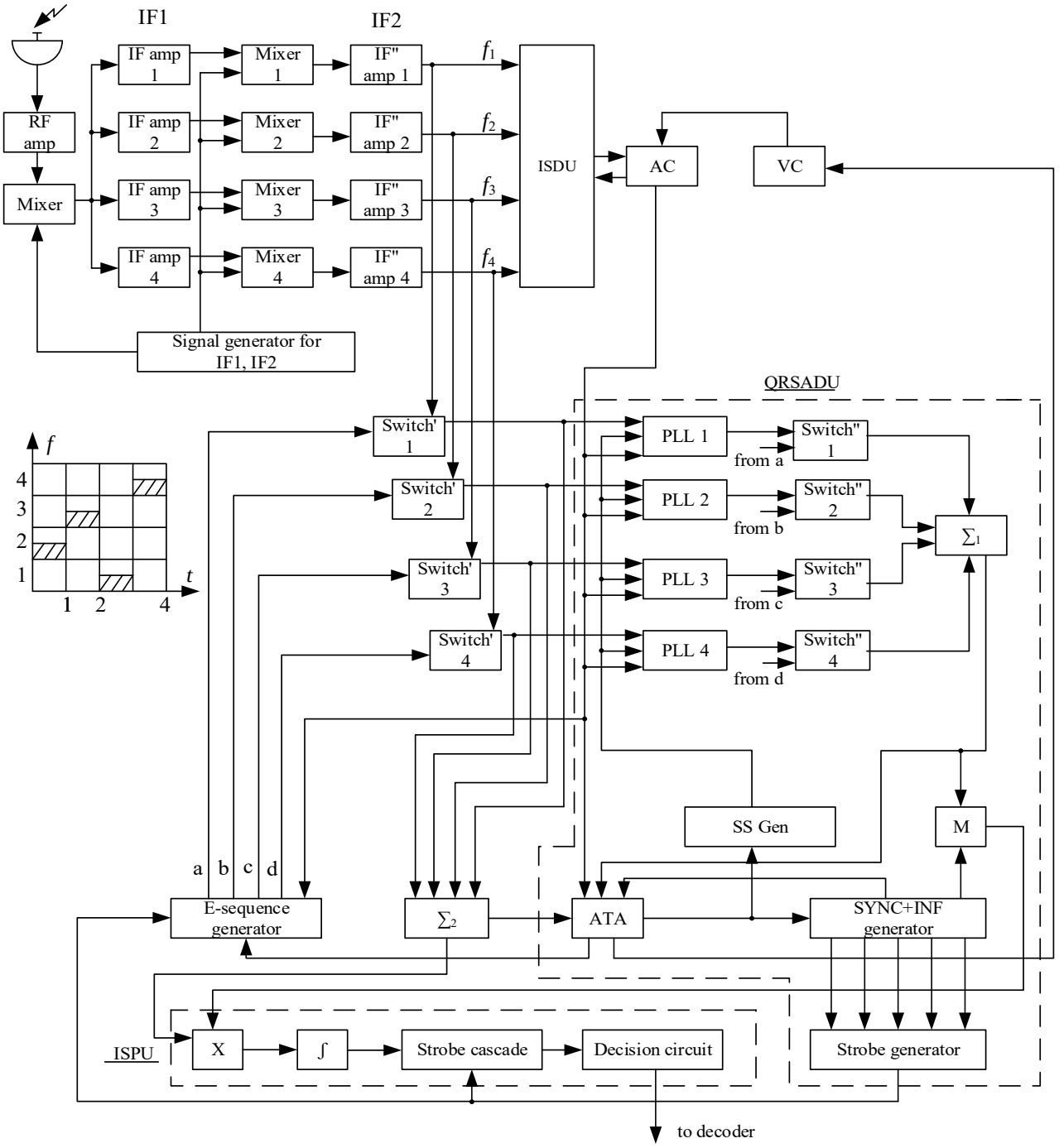


Fig. 3. Block diagram of the synchronization channel for a binary-quaternary PSK communication system: RF amp – radio-frequency amplifier, Mixer – mixer, IF amp – intermediate-frequency amplifier, IF – intermediate frequency, Switch – switch

Detection (search) of noise-like signals

Let us assume that at the receiver input, there are – in the general case – an unknown number *K* of additive copies of one and the same signal $s(t)$, mismatched with respect to one another in terms of time delays, carrier frequencies, and initial phases – that is,

$s(t-t_1-\tau_1, f_1-\Delta f_1, \Delta\varphi_1)$,…, $s(t-t_k-\tau_k, f_k-\Delta f_k, \Delta\varphi_k)$,…, $s(t-t_K-\tau_K, f_K-\Delta f_K, \Delta\varphi_K)$, and also white Gaussian noise, where $k=1,\dots,K$ – copy number SIS, $\tau=[\tau_1,\dots,\tau_k,\dots,\tau_K]$ и $\Delta f=[\Delta f_1,\dots,\Delta f_k,\dots,\Delta f_K]$ – unknown, relatively small and slow shifts in the time delays and carrier frequencies of these signals, relative to their constant and known values $t=[t_1,\dots,t_k,\dots,t_K]$, $f=[f_1,\dots,f_k,\dots,f_K]$, a $\Delta\varphi=[\Delta\varphi_1,\dots,\Delta\varphi_k,\dots,\Delta\varphi_K]$ – random shifts in the initial phases of the oscillations of the corresponding carrier frequencies relative to a zero phase shift.

In the event that $K=1$, estimation of the SIS parameters, i.e., its time offset $\hat{\tau}_1$, frequency $\widehat{\Delta f_1}$ and frequency phase $\widehat{\Delta\varphi_1}$ relatively t_1, f_1 and zero phase shift against the background of additive white Gaussian noise in accordance with the maximum likelihood criterion is described as [14, 15]:

$$\hat{\tau}_1, \widehat{\Delta f_1}, \widehat{\Delta\varphi_1} = \underset{\tau_1,\Delta f_1,\Delta\varphi_1}{argmax}\left(Re\left[\dot{Z}(\tau_1,\ \Delta f_1,\ \Delta\varphi_1)+\xi\right]\right), \quad (2)$$

where ξ – additive noise component at the input of the decision device,

$$\dot{Z}(\tau_1,\ \Delta f_1,\ \Delta\varphi_1) = e^{j\,\Delta\varphi_1}\dot{\chi}(t_1,\tau_1), \quad (3)$$

$$\dot{\chi}(\tau_1,\Delta f_1) = \frac{1}{E_1 T_{\text{нак}}}\int_0^{T_{\text{нак}}} \dot{S}(t)\,\dot{S}^*(t-\tau_1)e^{j2\pi\,\Delta\varphi_1}dt, \quad (4)$$

$\dot{\chi}(\tau_1,\Delta f_1)$ – complex FN SLS, $\dot{S}(t)$ – its complex envelope, E_{1T_w} – his energy, accumulated over time T_w. Thus,

$$\hat{\tau}_1, \widehat{\Delta f_1}, \widehat{\Delta\varphi_1} = \underset{\tau_1,\Delta f_1,\Delta\varphi_1}{argmax}(Re[e^{j\,\Delta\varphi_1}\dot{\chi}(\tau_1,\Delta f_1)]. \quad (5)$$

Next, take into account that the assessment $\Delta\varphi_1$ provides little information and significantly complicates the evaluation algorithm $\tau_1, \Delta f_1$, as a result of which in (2) instead of the real part of the function $\dot{Z}(\tau_1,\Delta f_1,\ \Delta\varphi_1)+\xi$ they consider its modulus, that is $\left|\dot{Z}(\tau_1,\ \Delta f_1,\ \Delta\varphi_1)+\xi\right| = \left|\dot{Z}(\tau_1,\ \Delta f_1,\ \Delta\varphi_1)\right| + \xi_{\chi^2}$ [15, 16]. Then (5) can be rewritten as:

$$\hat{\tau}_1, \widehat{\Delta f_1} = \underset{\tau_1,\Delta f_1}{argmax}(|\dot{\chi}(\tau_1,\Delta f_1)| + \xi_1). \quad (6)$$

As follows from the analysis of the latest formulas, a version of the parameter estimation algorithm $\tau_1, \Delta f_1$ (5) requires assessment and $\Delta\varphi_1$. Its main advantage is that ξ – additive Gaussian white noise. But in algorithm (6), the noise component ξ_1 has a Rayleigh-Rice distribution [16]. This could explain why algorithm (5) outperforms (6) in terms of the accuracy of the estimates for the parameters being sought.

But in reality, the gain is questionable due to an increase in the dimensionality of the function's domain $e^{j\,\Delta\varphi_1}\dot{\chi}(\tau_1,\Delta f_1)$, compared to $|\dot{\chi}(\tau_1,\Delta f_1)|$, and the influence of estimation accuracy $\Delta\varphi_1$ for accuracy $\hat{\tau}_1, \widehat{\Delta f_1}$.

Thus, it is necessary to compute a function in the receiver $|\dot{\chi}(\tau_1, \Delta f_1)|$, a typical view of which for binary PSK SIS is shown in Figure 4. This figure also shows its sections along the time axis $|\dot{\chi}(\tau_1, 0)|$ and along the frequency axis $|\dot{\chi}(0, \Delta f_1)|$. The width of the first of these, up to its first zero values, is $2T_e = 2/f_T$, from which it follows that the accuracy of the delay time estimate for an SLS (signal-like sequence) increases as its spectral width increases. At the same time, as follows from (4), the width of the cross-ambiguity function (CAF) cross-section $|\dot{\chi}(0, \Delta f_1)|$ will amount to $2/T_w$, that is, with an increase T_w The accuracy of estimating the frequency of SLS also increases. Moreover, as follows from (4), with $\Delta f_1 = 0$ функция $\dot{\chi}(\tau_1, 0)$ is the convolution of the complex envelopes of the reference and received complex signals. In the general case, however, the complex envelope of the received complex signal is $\dot{S}(t)$, and a reference composite video signal is generated in the receiver $\dot{S}^*(t - \tau_1)e^{j2\pi\Delta f_1 t}$ for all possible values τ_1 и Δf_1 taking into account t_1 and f_1.

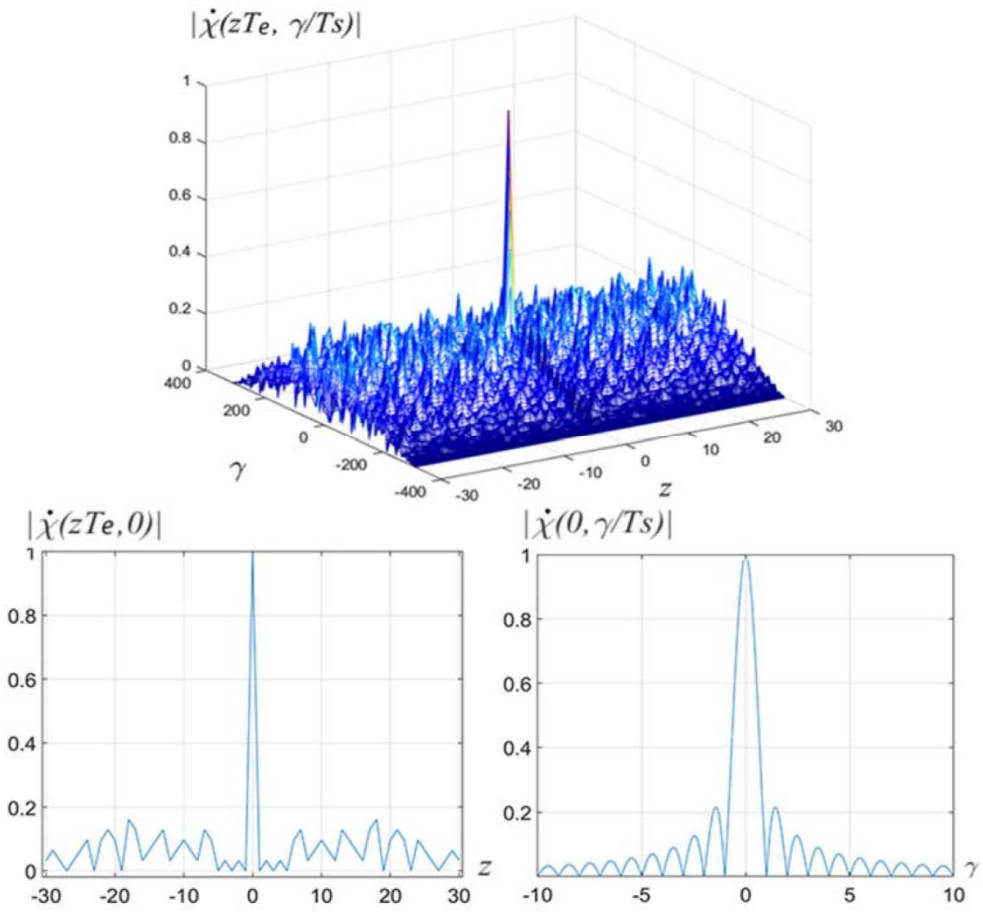


Fig. 4. Typical appearance of a DKF SIS module and its cross-sections in time and frequency

Taking into account the foregoing, assuming that the receiver calculates the digital convolution of the reference and received SLS, let us present the UOSIS for one SIS (that is, UOSIS1) in the form shown in Figure 5. From its analysis it is clear that the reference frequency generator (RFG1) generates a harmonic frequency signal $f_{\text{op1}} = f_1 + \Delta f_1$, and at the output of LPF1 (Fig. 5), a function is formed $Re[\dot{S}(t)\exp(j2\pi\Delta ft + \varphi)$, at the output of LPF2 – function $Im[\dot{S}(t)\exp(j2\pi\Delta ft + \varphi)$, where Δf– the difference between f_{op1} and the carrier frequency of the input signal $s(t)$, φ – a random phase shift between the signals at these frequencies. Subsequently, these signals are sampled in time using an analog-to-digital converter (ADC) with a specific clock frequency $f_T = 1/T_e$, generated by the clock generator (CG). However, according to the Kotelnikov theorem, the sampling frequency of this signal in the time domain must be twice as high f_T.

It should be taken into account that f_T cannot be exactly equal to the clock frequency of the received SCS due to the instabilities of the TG on both the receiving and transmitting sides, which will inevitably lead to so-called slippage, when adjacent SCS samples in any ADC will fall on the same elementary pulse, or one pulse will be missed. Due to the re-sampling of the received SCS with a time shift of $T_e/2$ Slippage cannot occur in ADC1 and ADC2 simultaneously with a similar event in ADC3 and ADC4. Thus, the problem of slippage caused by instability of the timing generator (TG) is partially resolved by resampling the incoming signal (SIS). However, the duration of the signal – the energy of which can be accumulated in the signal processing unit (SUPRS) – T_{w}, is limited by the duration of the time interval between successive slips.

Obviously, this time will correspond to a PN sequence length equal to δ^{-1}, where δ – the maximum relative deviation of the clock generator frequency from its nominal value. In this case, the length of the pseudorandom sequence (PRS) processed by the convolution device can theoretically reach several hundred thousand, since δ in modern radio systems, typically no less than 10^{-5} ... 10^{-6}. Thus, it would seem possible to choose a value T_w such as to ensure a signal-to-noise ratio at the output of the signal processing unit (SPU) sufficient for the detection of a target signal with any specified probability of correct detection $p_{\text{обн}}$ and a false alarm p_{lm}. But in reality, if the frequency mismatch between the signal from the output of RFG1 and the received signal from the SLS is greater than $1/2T_w$, then it will not be detected due to the absence of a signal at the output of the digital convolution device. The value T_w is also limited by the requirements for the complexity or length of time of its calculation.

If the energy of the SLS lasts T_{w} not sufficient for its detection with the specified $p_{\text{обн}}$ and $p_{\text{лт}}$, It is possible to use digital post-detection energy accumulation for a certain number of pulses of this duration within a digital energy accumulator (DEA), as shown in

Figure 5. In this setup, a decision unit (DU1) determines whether the signal exceeds a threshold level – effectively performing an additional quantization of the signal into two levels. Subsequently, a set of counters (Cnt) tallies the number of times the signal exceeds the threshold set by DU1 over a specific time interval, which corresponds to the number of pulses being accumulated T_n. In this case, the number S_c is equal to the length of the pseudorandom sequence (PRS) N, corresponding T_n, and the bit depth of each of them is determined by the number of SIS pulses with a duration of T_{op}, the energy of which must be accumulated. Thus, two methods for accumulating the energy of a complex signal (CS) are considered: computation of its convolution, and non-coherent accumulation using a digital energy accumulator. The efficiency of the latter approach is due to a significant increase in the signal-to-noise ratio at the input of the first processing unit (PU1) compared to the receiver input, resulting from the use of digital convolution of the received CS. It should be noted that non-coherent accumulation does not improve the accuracy of parameter estimation for the received CS; rather, it only enhances the probabilistic characteristics of its detection.

Let us consider the possibility of detecting *K* additive copies of the same complex-valued signal (SIS), which are mismatched in terms of frequency and delay. In doing so, we shall take into account that the width of the cross-section of the signal's ambiguity function (AF) along the frequency axis is equal to $1/T_n$, as a result, it is possible to ensure efficient energy storage of only those SLS whose carrier frequency difference is f_{op1}, that is Δf, no more $1/3T_{\text{w}}$.

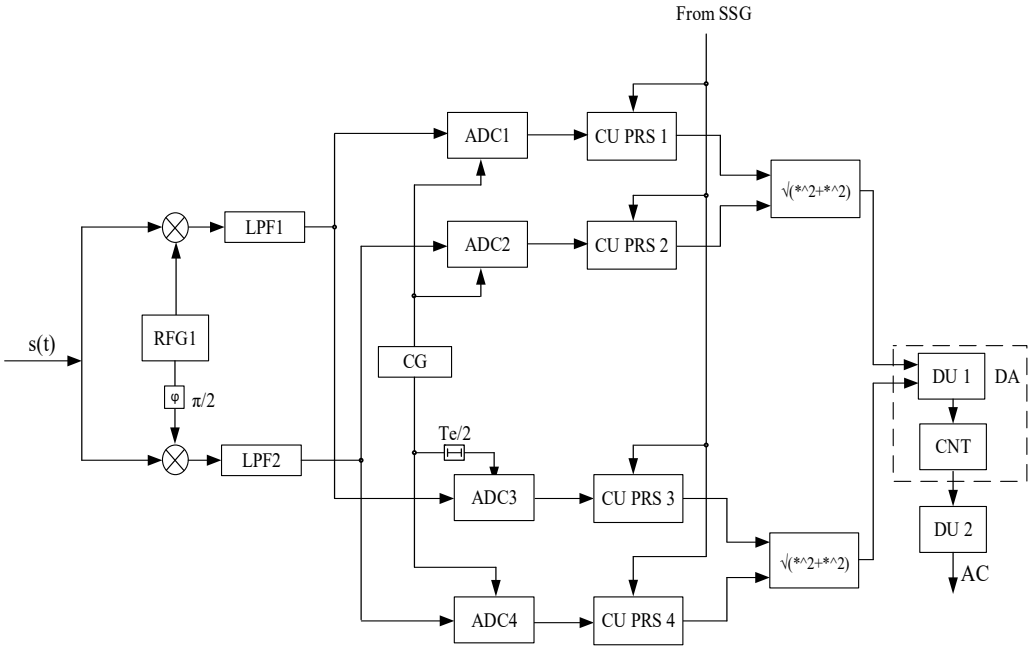


Fig. 5. Functional diagram of the UOSLS

Ultimately, a value should be chosen T_{w} such that within the frequency band $[f_{op1} - 1/3T_w, f_{op1} + 1/3T_w]$. There was either a single copy of the received signal with an unknown time delay, or a collection of such signals with identical carrier frequencies but different time delays. In this case, the non-linear transformation – performed by calculating

the square root of the sum of the squares of the in-phase and quadrature components of the resulting signal – does not lead to significant mutual interference between copies of the same signal. This is because, at any given moment, only one such signal is effectively subjected to this transformation, and mutual interference between the copies is minimized through the appropriate selection of a value T_{w}.

To detect all copies of the spread-spectrum signal that are mismatched in terms of frequency and time delay, it is necessary to either perform sequential retuning f_{op1} with a step $1/3T_{\text{w}}$, or generate reference frequencies in parallel with the same step size, covering the frequency uncertainty range of the signal-of-interest (SoI). The block diagram of the UOSIS for this case is shown in Figure 6. Thus, the UOSIS performs a coarse estimation of the time delays of the SIS carrier frequencies with an accuracy of $1/(3T_{\text{w}})$ and their time delays with precision T_e.

The probabilistic characteristics of detecting a set of complex signals that are mismatched in terms of frequency and time delay can be improved by increasing T_{w}. This circumstance is illustrated in Figure 7, which shows the resulting CCF of four copies of the same signal sequence for two values of the parameter T_{w}. In order to detect SSLs formed on the basis of PSPs that are different in structure, it is necessary to sequentially rebuild the USPSP of a given UOSIS, or in parallel use UOSIS matched with different structured SSLs. The effectiveness of this device largely depends on the length of time it takes to calculate digital convolution in the USPSP. Its accelerated algorithms, based on reducing PSP circulant matrices to the Walsh-Hadamard matrix or its fragments, are known for a large class of PSPs such as MPs and their segments (segments), Gold codes and their segments, Kasami sequences, etc. [7].

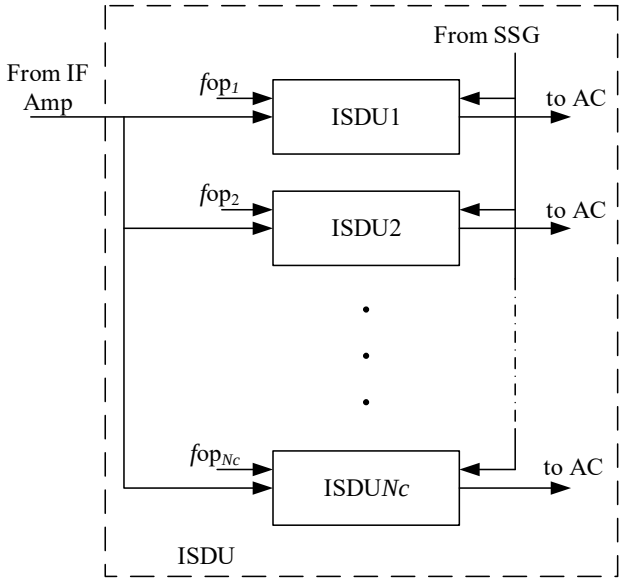
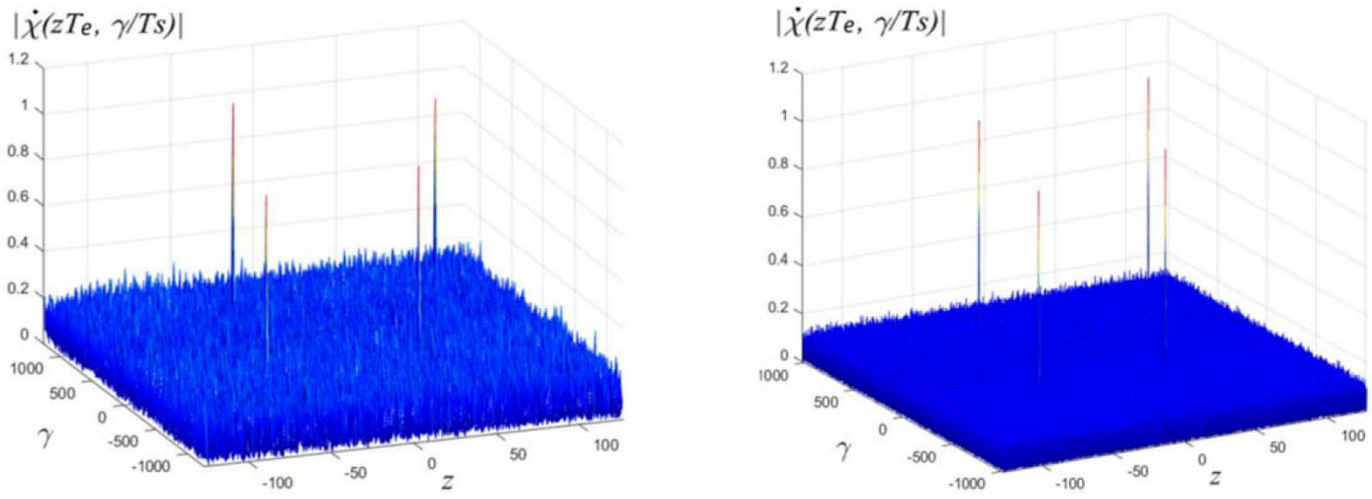


Fig. 6. Block diagram of a system for detecting a set of complex signals (SIS) that are mismatched in terms of frequency and time delay



а) б)

Fig. 7. Resulting cross-correlation functions (CCFs) of four mismatched copies of the same signal for two values of Tw; plot (a) corresponds to a smaller value of Tw than plot (b)

The most significant gain in terms of the number of elementary mathematical operations, equal to N/m, will be achieved when using periodic MPs, compared to the traditional method of calculating the convolution, where N – the length of the PN sequence corresponding to T_{n}, m – PSP memory depth [17]. На практике такой выигрыш по длительности времени вычисления свертки может достигать нескольких десятков секунд.

Given the sufficiently high efficiency of the USPSP (which, in addition to an algorithm for accelerated convolution computation, also depends on the operating speed of the digital signal processors (DSPs) employed), post-detection digital integration of the energy of the received signals may not be necessary.

UOSIS with analog SAW-based matched filters

A version of the UOSIS (universal signal processing unit) for an FHSS-PSK (frequency-hopping spread-spectrum with phase-shift keying) system, utilizing tunable analog matched filters, is shown in Figure 8. Such filters are frequently implemented using surface acoustic wave (SAW) devices [18], which can operate directly at the system's carrier frequencies – up to 1.5 GHz [19] – or at intermediate frequencies if a higher frequency range is employed; these devices can also be easily reprogrammed whenever the pseudorandom sequence (PRS) is changed.

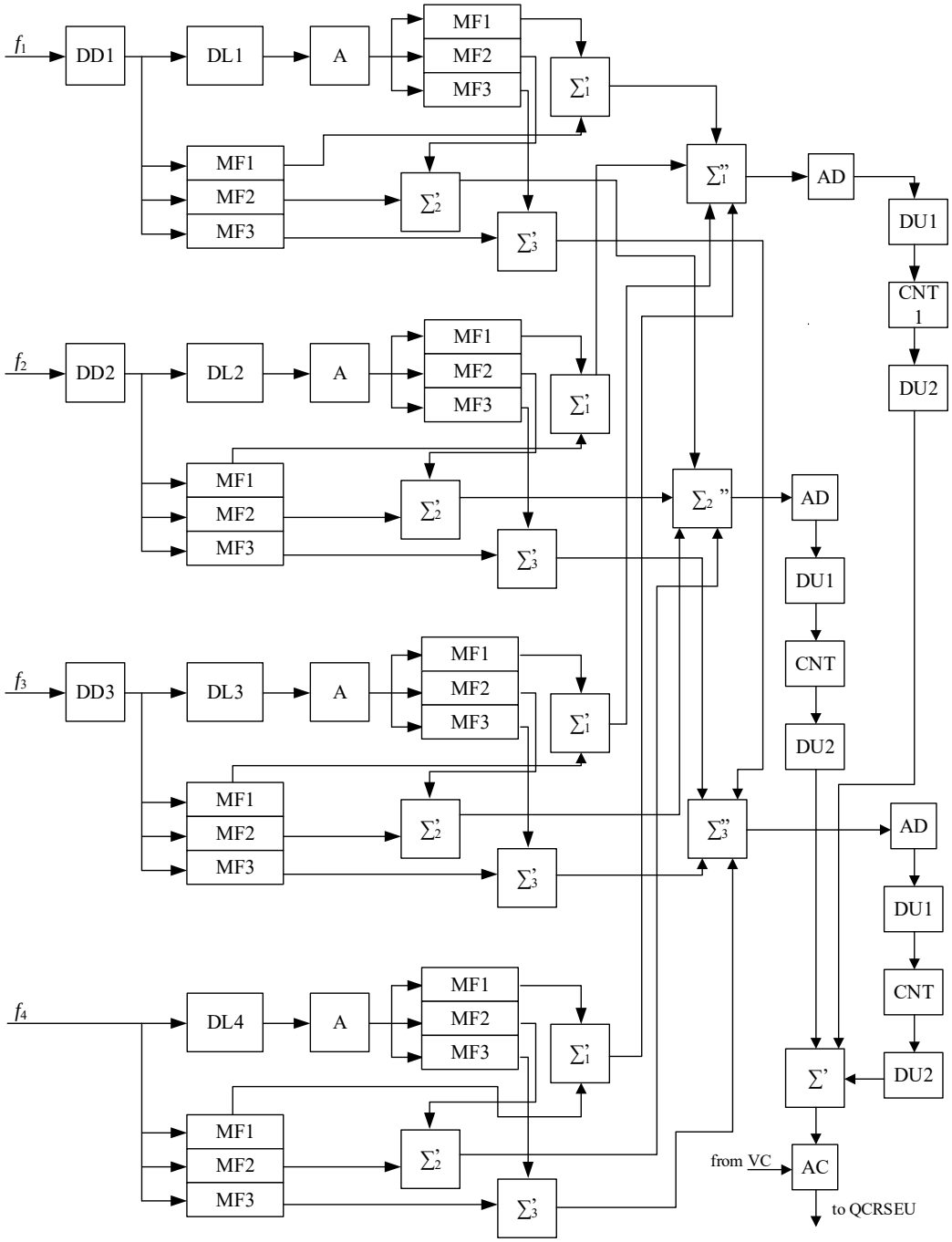


Fig. 8. SAW-based matched filter for DS-FHSS/DSSS-FSK/PSK systems

In this configuration, two sets of SAW-based matched filters are used for each of the four frequencies of the FHSS-PSK system, as the practical size constraints of the filter substrates impose significant limitations on the duration of the spread-spectrum signal. T_{w}, which can be directly processed within them.

Typically, it is possible to process PSK spread-spectrum signals with a bandwidth of no more than a few tens of MHz and a duration of T_{SF}, corresponding to a PRN sequence length of no more than $N = 1024$. Two such FUs can be connected in series. Therefore, in each set of FUs, an SIS with a duration is processed $T_{SF} = T_n/2$. In Figure 8, the signal is fed to the lower matched filter (MF) via a delay line (DL), which is also a surface acoustic wave (SAW) device. A linear amplifier (A) is used after the delay line, as the power loss within the latter amounts to several tens of decibels. Thus, the duration of the complex signal fragment processed by this circuit is equal to $4T_{SF}$, but the meaning T_n, determining its resolving power is equal to $2T_{SF}$, since the responses of two pairs of matched filters (MFs) are summed. Furthermore, Figure 8 corresponds to a case where the frequency uncertainty range of the signal is only three times the bandwidth of any of the matched filters. That is, in this case $N_c = 3$, Therefore, at each of the four intermediate frequencies, three frequency-shifted groups of matched filters (MFs) are connected in parallel, covering the entire frequency uncertainty range of the signal F_n.

One possible approach involves designing matched filters (MFs) and delay lines (DLs) to operate at intermediate frequencies, with the input complex-envelope signal (CES) being frequency-converted to the center frequencies of the MFs' amplitude-frequency responses (AFRs). This allows for searching for the CES over a wider frequency uncertainty range than would be possible within the combined bandwidth of three analog surface acoustic wave (SAW) matched filters; however, the frequency conversion of the input CES introduces additional phase mismatches in the carrier frequency.

To achieve post-detection energy accumulation for the target signal, an amplitude detector (AD) is employed in each of the three frequency-offset channels, which collectively cover the target signal's frequency uncertainty range. At the output of each AD, a first decision unit (DU1) performs binary quantization of the signal, which is then fed into a set of counters (SCh) for binary pulses. The number of counters is equal to 2*N*, and the bit depth of each counter is determined by the number of pulses – each with a duration T_w – whose energy must be accumulated to meet the specified detection performance requirements for the target signal.

If the frequency of the received signal falls within the passband of one of the three matched filters – at a level of 0.7 of the maximum value of its amplitude-frequency characteristic – then it will be detected in unit DU2 with a certain probability p_{o1} at the output of one of the $2N$ Ch, since a signal is most likely to appear there at the moment the main peak of the cross-correlation function (CCF) for the SIS segment – transmitted on one of four frequencies – occurs. However, in DU2, the presence of interference may also lead to a false alarm with a certain probability $p_{\mathit{fm}1}$. The uncertainty in the timing of the detection of an SIS segment – which is transmitted on one of four frequencies and recurs periodically according to a pseudorandom sequence (PRS) of frequency hopping – is $T_e/4$. This sequence is also defined in DU2.

In this case, the responses of the matched filter (MF) corresponding to different frequencies are summed prior to detection. Although these segments of the complex-modulated signal (CMS) – transmitted at various frequencies – arrive at the input of the

signal processing unit from the receiver's frequency converter without any phase discontinuity in the high-frequency oscillation (due to the use of a single local oscillator for all carrier frequencies), it is clear that the losses incurred from such summation decrease as the arithmetic mean of the four frequencies employed becomes increasingly large relative to the total spectral bandwidth of the frequency-hopped, phase-modulated (FH-PM) signal. It should also be noted that, in this scenario, only the real part of the complex ambiguity function (CAF) of the signal is processed, as this is the component that corresponds to the matched filter's response; furthermore, the use of a frequency converter at the input of the matched filter inevitably introduces an unknown phase shift φ of the carrier frequency of the received spread-spectrum signal, as a result of which the matched filter response decreases proportionally $cos\varphi$.

The relatively short lengths of pseudorandom sequences (PRS) that can be processed using surface acoustic wave (SAW) matched filters result in a significantly lower resolution for the corresponding signal detection system compared to a configuration that employs digital PRS processing. The system's overall performance is primarily determined by its digital energy-accumulation unit; in scenarios with low input signal-to-noise power ratios, SAW matched filters can be viewed as components that significantly enhance the effectiveness of a digital energy-based detector.

The variant of the UOSLS considered in this section allows to reduce the width of the uncertainty region of the received SLS in frequency by three times only if $1/(3T_n) \approx F_n/N_c$. Considering that in this case $N_c = 3$ and $T_{\text{ш}} = NT_e$, a $f_T = 1/T_e$, we find that the length of the pseudorandom sequence (PRS) to be processed in a single matched filter (MF) must be at least f_T/F_n.

Then the single-frequency segment of the DSF-PMN SLS will be detected with high probability simultaneously at the output of all three SFs overlapping $F_{\text{неоп}}$. In this case, using three matched filters (MFs) to detect each single-frequency segment makes no sense; a single MF for each segment is sufficient. In this scenario, the operation of the UOSIS will not result in a reduction F_n received by DFS-PSK SLS, but to ensure the accuracy of estimating its time delay on the order of $T_e/4$.

Improving the Accuracy of Estimating SIS Parameters in UVKOSIS

If a set of signal components (SIS) with different structures – each transmitted on its own unique carrier frequency – is detected within the signal-processing unit (UOSIS), a dedicated set of search-mode phase-locked loops (PLLs) and automatic frequency control (AFC) circuits, configured with cross-coupling, must be employed for each detected component. Given that the structure of the correlation-processing unit (UKOSIS) for a set of binary phase-shift keyed (BPSK) signals is relatively straightforward, let us consider the case where a set of frequency-hopped/phase-shift keyed (FHSS-PSK) signals is detected.

In this scenario, the correlation-processing unit for each such signal component comprises four search-mode PLLs operating in conjunction with a single AFC circuit, as illustrated in Figure 9. In addition to the received signal component, the AFC circuit's input also receives a quasi-coherent reference carrier at the intermediate frequency (IF), which is generated by the voltage-controlled oscillator (VCO) within the PLL.

As a result, it is possible to isolate the pseudorandom sequence (PRS) upon which the composite signal (CS) at a given frequency is based – a prerequisite for the operation of the automatic frequency and phase control (AFPC) circuit. Each of the two AFPC channels employs a full-wave rectifier (to generate a video-frequency signal. The output from the full-wave rectifier (FWR) in one of these channels is used not only to derive the AFPC's discrimination characteristic but also serves as an input for the verification circuit (VC), shown in Figure 9. The threshold level within the VC's decision-making unit is determined by accounting for the permissible root-mean-square (RMS) deviation of the reference signal frequency – generated by the phase-locked loop (PLL) system – as well as the temporal offset of the reference PRS (generated by the synchronization and information signal generator) relative to the incoming composite signal.

It should be re-emphasized that the composite signal processing unit can operate based on the information component, while synchronization of the PLL systems is maintained via a periodic synchronization component. For a satellite in a geostationary orbit, maximum noise immunity for the processing unit is achieved when no more than 10% of the total radio transmitter power is allocated to the synchronization component; this allows for a very narrow bandwidth in the PLL loop filter, given the minimal dynamic variation in the composite signal frequency. However, when elliptical or low Earth orbits are involved, the question of the optimal power distribution between the information and synchronization components requires further investigation.

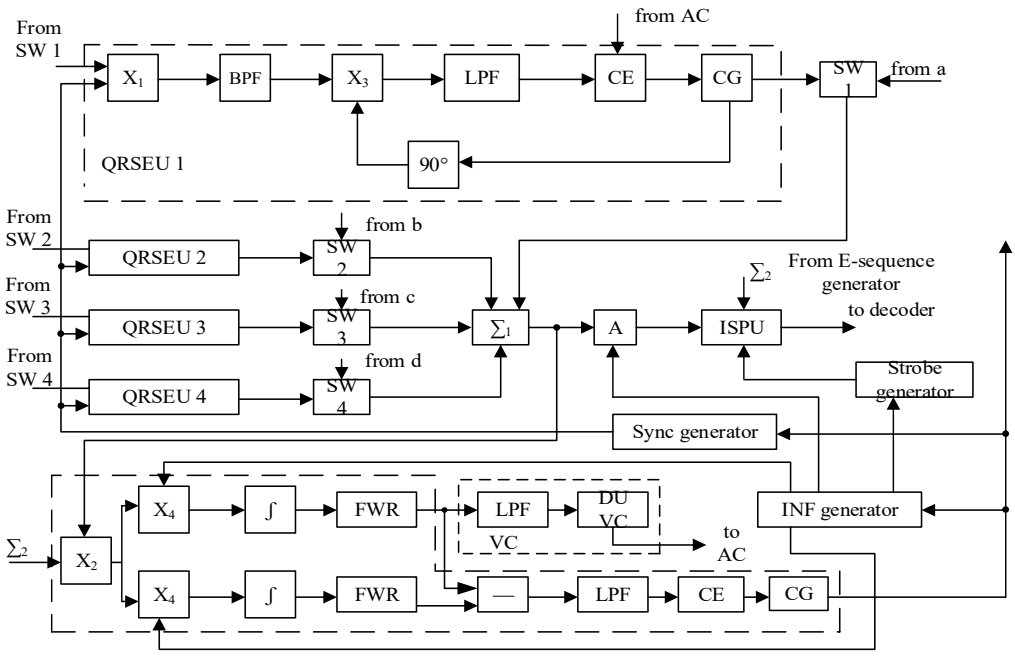


Fig. 9. PLL and AFC circuit diagrams with cross-coupling for an SS-FHSS/PSK system

Multi-stage parallel-sequential search for frequency and time delay of a spread-spectrum signal (SSS)

The first stage of the signal search – In terms of frequency and time delay – is performed within the signal search unit (SSU). In any of the variants considered, the entire uncertainty region for the signal (in terms of frequency and time delay) is effectively partitioned into a set of time-frequency intervals, the number of which is equal to $_{ч} \times 2$, where – the number of elementary pulses of the PSP corresponding to $_{w}$, a $_{ч}$ – the number of frequency intervals. Let us denote the probability of correctly detecting all copies of the composite spread-spectrum signal (CSIS) within the composite spread-spectrum signal detection unit (CSIS-DU) as $_{обн1}$, probability of a false alarm – $_{лт1}$. Thus, at the first stage, the width of the uncertainty region of the SLS in frequency is reduced by . and amounts to $_{2}$ $_{1}/ _{1}$, where $_{1}$ $_{c}$, $_{1}$ $_{л}$. A rough estimate of each of the four carrier frequencies has already been obtained in the UOSIS (coarse synchronization unit), and the value can be refined using a search-mode PLL by discretely tuning the frequency of its VCO and narrowing the bandwidth of its loop filter.

The second stage of searching for the frequency and time-delay parameters of the synchronization signal (SIS) is carried out in the UVKOSIS (fine synchronization unit) by discretely tuning the frequency of the search-mode PLL's VCO across a frequency band with a width of F_2. At the same time, the loop filter bandwidth $\Delta f_{\text{ФАПЧ2}}$ is chosen to be several times smaller F_2, and the total number of frequency intervals being analyzed will be $z_2 = F_2/\Delta f_{\text{ФАПЧ2}}$. Next, an initial VCO frequency is selected within the first frequency interval, which has a specific bandwidth $\Delta f_{\text{ФАПЧ2}}$, and confirmation that the frequency of the received SLS is no more than $\Delta f_{\text{ФАПЧ2}}$ deviates from the selected VCO frequency and the PLL circuit is in synchronization mode, the threshold level is exceeded in $\text{РУ}_{\text{СхП}}$.

But if the threshold is not exceeded and there is no synchronism mode, the VCO frequency value is rebuilt to $\Delta f_{\text{ФАПЧ2}}/2,$ and the next frequency interval with a width of is analyzed $\Delta f_{\text{ФАПЧ2}}$. If no signal of interest (SIS) is detected in any of the frequency intervals, it is considered that a false alarm has occurred within the SIS uncertainty region (UOSIS); the search controller (SkhP) then sends a corresponding signal to the search subsystem (SZ), which re-initiates the first stage of the SIS search, followed by a repetition of the second stage. However, if an SIS is detected in one of the frequency intervals, a third search stage is initiated, during which the total width of the SIS frequency uncertainty region is $F_3 = F_2/z_2$, and the bandwidth of the loop low-pass filter, Δf_{PLL3}, is chosen to be several times smaller F_3. The threshold level increases proportionally in$\text{РУ}_{\text{СхП}}$ with the aim of reducing the probability of a false alarm. It is evident that the second and third stages of the search – as well as any subsequent stages, should they be necessary – are accompanied by a reduction in the bandwidth of the loop filter $\Delta f_{\text{ФАПЧ}}$, which improves the noise immunity of the PLL and the accuracy of the SIS frequency estimation. However, a

reduction in $\Delta f_{\text{ФАПЧ}}$ is constrained by the need to track changes in the frequency of the incoming signal of interest (SOI). Consequently, the required accuracy for estimating the SOI frequency, the minimum bandwidth of the loop filter, and the number of search stages are all predetermined, taking into account the dynamics of the SOI frequency variations.

A complete cycle of SOI detection and parameter estimation – achieved with a specified level of accuracy – corresponds to a scenario where the signal is detected during the final stage of the search within the last frequency interval analyzed by the phase-locked loop (PLL). However, a missed detection or a false alarm can occur at any stage of the search; such an event is identified by the detection verification mechanism, prompting the control system to re-initiate the first stage of the search. Clearly, in this case, the return to the first stage occurs over a shorter time interval than the duration of a full, complete cycle. In other words, the duration of the search cycle is a random variable.

Having designated the total number of stages of the search for the SLS as Z, we will number them using the symbol $i = 1, \dots, Z$. The number of frequency intervals at each stage is determined as z_i, and the width of the frequency uncertainty region for each of them – as F_i. In this case, the loop filter bandwidth at each stage will be Δf_{Fi}, and the duration of the analysis time for each frequency interval T_i, starting from the second stage. Let us denote the total duration of the SIS detection time during the first stage in the UOSIS as T_1. Upon the expiration of the time period T_i, $i = 1, .., Z$ correct detection of the signal will occur with a probability of p_{di}, or its omission with a probability of $1 - p_{di}$, либо ложная тревога с вероятностью $p_{\text{лт}i}$. Note that, starting from the second stage of the value search, $p_{\text{обн}i}$ and $p_{\text{лт}i}$ depend, firstly, on the probability of the PLL system acquiring the frequency of the reference signal $p_{\text{з}i}$ given its presence in this band, and, secondly, the probability of a false acquisition of this frequency $p_{\text{лз}i}$, thirdly, from the probability of correct detection $p_{\text{о.СхП}i}$ and the probability of a false alarm $p_{\text{л.VC}i}$. Obviously $p_{\text{о}i} = 1 - p_{\text{з}i}(1 - p_{\text{о.VC}i})$, $p_{\text{л}mi} = p_{\text{л}si} p_{\text{л}m.VCi}$.

As an illustration of the multi-stage parallel-serial synchronization (SS) search procedure described above, Figure 10 shows the SS uncertainty region with a specific frequency width $F_1 = 10\ \text{kHz}$. The width of the time uncertainty region determines the feasibility of using just three matched filters (MFs) that overlap F_1. Thus, $z_1 = 3$, Furthermore, three detection intervals have been selected for the second stage, namely $z_2 = 3$, as well as $z_3 = 4$. It is assumed that one binary PSK SIS has been detected.

The total number of frequency-time intervals for the parallel-sequential search procedure will be $2N \prod_{i=1}^{Z} z_i$, to denote each of them, we will use (*Z*+1)-dimensional vector $[x_{1t}\ x_{1f}\ x_{2f}\ \dots\ x_{Zf}]$, where $x_{1t} = 1, \dots, 2N$ – time interval number during sequential analysis of time intervals in the first stage of the search, $x_{if} = 1, \dots, z_i$ – number of the frequency interval analyzed at the *i*-th stage of the search, $i = 1, \dots, Z$.

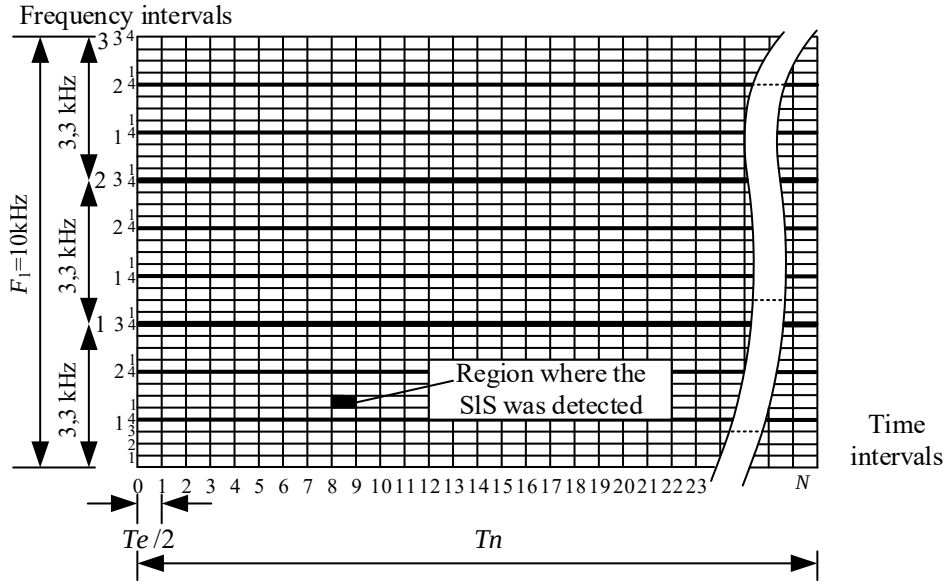


Fig. 10. Illustration of a multi-stage parallel-sequential procedure for joint detection and parameter estimation of complex signals (SIS)

KS Performance Characteristics

Assuming that the signals of interest (SoIs) are present at the receiver input, we consider the primary performance metrics for the receiver's synchronization subsystem (SS) to be the time elapsed before tracking of their carrier frequencies and time delays begins, as well as the probabilistic characteristics of their detection. Analyzing the performance of an SS in the presence of multiple SoIs simultaneously arriving at the input is highly complex; developing a method for such an analysis requires the creation of an appropriate computer model. Therefore, we shall limit our scope to the case of detecting and synchronizing a single SoI.

Duration of the time before tracking of SIS parameters begins

Assume that the signal of interest (SIS) is located in the last time-frequency interval analyzed using the UOSIS and UVKOSIS, with a (*Z*+1)-dimensional index $[2N\ z_1 \ldots z_Z]$, when the time until the start of tracking for such an SLS is at its maximum, compared to its other possible positions in the time-frequency plane. We define the duration of the average maximum search time for such an SLS as follows:

$$\overline{T_{max}} = \overline{T_c N_c}, \tag{7}$$

where $\overline{T_c}$ – average duration of a single search cycle; $\overline{N_c}$ – the average number of such cycles that had to be performed in order to detect an SIS, given pre-specified values for the probabilistic characteristics of this detection.

Meaning $\overline{T_c}$ can be found by summing, over all (Z+1)-dimensional indices of the time-frequency intervals, the products of the time durations – from the start of the cycle to the beginning of the analysis for each interval – and the probabilities that the cycle ends within that interval due to a false alarm, a correct detection, or a missed detection of the signal of interest (SIS); that is,

$$\overline{T_{\text{ц}}} = T_1 + \sum_{x_{1t}=1}^{2N-1} \sum_{x_{2f}=1}^{z_2} \cdots \sum_{x_{Zf}=1}^{z_Z} T_{\text{ц}x_{1t}\, x_{1f}\, x_{2f} \ldots x_{Zf}} p_{\text{пт}x_{1t}\, x_{1f}\, x_{2f} \ldots x_{Zf}} +$$

$$+ T_{\text{ц}2N\ z_1 \ldots z_Z} (p_{\text{обн}.2Nz_1 \ldots z_Z} + p_{\text{пр}.2Nz_1 \ldots z_Z}), \quad (8)$$

where T_1 – duration of the analysis time for the two-dimensional uncertainty region interval of the complex-signal source (SIS) during the first stage of the cycle, $T_{cx_{1t}\, x_{1f}\, x_{2f} \ldots x_{Zf}} = x_{1t}T_1 + x_{1f}T_2 + \cdots + x_{Zf}T_Z$ – the duration of a single cycle in the event of a false detection of an SLSS within a specific time-frequency interval identified by a number $[x_{1t}\, x_{1f}\, x_{2f} \ldots\, x_{Zf}]$ at $x_{1t} = 1, \ldots, 2N$, $x_{if} = 1, \ldots, z_i$, $i = 1, \ldots, Z$, $p_{\text{лт}x_{1t}\, x_{1f}\, x_{2f} \ldots x_{Zf}}$ – the probability of the cycle ending at this stage with a false alarm. Then $T_{\text{ц}2N\ z_1 \ldots z_Z}$ – duration of a completed search cycle, $p_{\text{о}.2Nz_1 \ldots z_Z}$ – the probability that the search cycle ends in the final time-frequency interval, given a correct detection of the signal of interest (SIS), $p_{\text{р}.2Nz_1 \ldots z_Z}$ – the probability of missing a signal. It is evident that if, at the first stage, the number of frequency intervals analyzed in parallel is z_1, then the probability that the first stage of the search cycle will end in a false alarm during the analysis of the time interval x_1 is given by:

$$p_{\text{л}x_{1t}} = (1 - p_{\text{л}.i})^{(x_{1t}-1)z_1} (1 - (1 - p_{\text{л}.i})^{z_1}), \quad (9)$$

and at each of the subsequent stages

$$p_{\text{л}x_{if}} = (1 - p_{\text{л}.i})^{(x_{if}-1)} p_{\text{л}.i},\ i = 1, \ldots, Z. \quad (10)$$

When analyzing the latest time interval, where the number of frequency intervals being analyzed in parallel is z_1, the probability of a false alarm

$$p_{\text{Л}.2N} = (1 - p_{\text{л}.1})^{2Nz_1 - 1} \sum_{x_{1f}=1}^{z_1 - 1} (1 - p_{\text{л}.1})^{x_{1f}-1} p_{\text{л}.1}.$$

(11)

As a result

$$p_{\text{lт}x_{1t}\, x_{1f}\, x_{2f} \ldots x_{Zf}} = p_{\text{lт}x_{1t}} \prod_{i=2}^{Z} p_{\text{lт}x_{if}} + p_{\text{lт}.2N} \prod_{i=2}^{Z} p_{\text{lт}x_{if}},$$

that is

$$p_{\text{lт}x_{1t}\,x_{1f}\,x_{2f}\ldots x_{Zf}} = \Big\{(1-p_{\text{lт.1}})^{(x_{if}-1)Z}[1-(1-p_{\text{lт.1}})^{Z}](1-p_{\text{lт.1}})^{2NZ-1}(1-$$

$$-\,p_{\text{lт.1}})^{z_1-1}\Big\}\,[p_{\text{lт}}(1-p_{\text{lт.1}})\textstyle\sum_{i=2}^{Z}(x_{if}-1)]. \qquad (12)$$

In deriving formula (12), it was assumed that the false-alarm probabilities for the analysis of all time-frequency intervals, except for the first one, are identical and equal to$p_{\text{лт}}$, and at the first stage this probability in general differs from $p_{\text{lт}}$ and is equal to $p_{\text{lт.1}}$.

The probability of correctly detecting an SIS in the last frequency-time interval analyzed will be:

$$p_{\text{o.}2Nz_1\ldots z_Z} = (1-p_{\text{lт.1}})^{2NZ-1}p_{\text{o.1}}\cdot\textstyle\prod_{i=2}^{Z}(1-p_{\text{lт.}i})^{Z-1}p_{\text{o.}i}, \qquad (13)$$

and the probability of missing it –

$$p_{\text{p.}2Nz_1\ldots z_Z} = 1-p_{\text{o.}2Nz_1\ldots z_Z}, \qquad (14)$$

that is $p_{\text{p.}2Nz_1\ldots z_Z}+p_{\text{o.}2Nz_1\ldots z_Z}=1$. For the purpose of determining $\overline{T_c}$ need to substitute (9)-(14) in (7), where $\overline{N_{\text{ц}}}=1/p_{\text{ц}}$, $p_{\text{ц}}$ – the total probability of the search procedure concluding in a single cycle [5], where

$$p_c = \textstyle\sum_{x_{1t}=1}^{2N-1}\sum_{x_{1f}=1}^{z_1}\cdots\sum_{x_{Zf}=1}^{z_Z}p_{\text{o}x_{1t}\,x_{1f}\,x_{2f}\ldots x_{Zf}} + p_{\text{o.}2Nz_1\ldots z_Z}.$$

Selection of values $p_{\text{o.}i}$ and $p_{\text{lт.}i}$

In a multi-stage, cyclic, parallel-sequential procedure for the detection (search) and synchronization of a signal – where the signal is located in the final time-frequency interval – the probability of its correct detection during the *j*-th cycle is equal to the sum of the probabilities of the completed search cycles; that is,

$$P_{\text{o}} = \textstyle\sum_{j=1}^{\infty}p_{\text{o}}^{j}\ , \qquad (15)$$

where *j* – number of the completed search cycle, $p_{\text{o}}^{j}=\left(1-p_c^{j-1}\right)p_{\text{o.}2Nz_1\ldots z_Z}$ – the probability that the search concludes during the *j*-th cycle with the correct detection of the signal of interest (SIS). Analogously to (15), we obtain an expression for the probability that the *j*-th completed search cycle ends in a false alarm:

$$P_{\text{lт}} = \textstyle\sum_{j=1}^{\infty}p_{\text{lт}}^{j}, \qquad (16)$$

where $p_{\text{lт}}^{j}=(1-p_c^{j-1})\sum_{x_{1t}=1}^{2N-1}\sum_{x_{1f}=1}^{z_1}\cdots\sum_{x_{Zf}=1}^{z_Z}p_{\text{o}x_{1t}\,x_{1f}\,x_{2f}\ldots x_{Zf}}$.

We have examined the key characteristics of the multi-stage parallel-sequential procedure for estimating SIS parameters, which are as follows $\overline{T_{max}}$, P_{o} and $P_{\text{lт}}$. However, to calculate them using formulas (7), (15), and (16), it is necessary to select values $p_{\text{o.}i}$ and $p_{\text{lт.}i}$, $i=1,\ \ldots,Z$, given their relationship with P_{o} and $P_{\text{lт}}$.

By choosing a typical value for *N* on the order of several thousand, along with five stages in the search cycle – and noting that, from the second stage onward, the number of sequential analysis procedures at each stage is on the order of three to four – we find from the analysis in (15) and (16) that $P_{\text{о}} \approx 0.95$ when choosing $p_{\text{lт}.i} = 10^{-6}$. In this case, the probability of a false alarm $P_{\text{lт}} \approx 10^{-6}$, at $p_{\text{о}.i} \approx 0.99$. At the same time, the duration of the energy accumulation time for the SIS (signal-processing system) within any given time-frequency interval must be such that the following inequality is satisfied: $p_{\text{lт}.i} \leq 10^{-6}$, since otherwise $p_{\text{о}}$ it will be less 0.7.

An important conclusion that follows from the analysis of formulas (12) and (13) is that by increasing *Z* while simultaneously raising the threshold level in the sequential detection procedure (SDP) at each successive stage, it is possible to achieve stabilization $P_{\text{пт}}$, and it is even possible to achieve a reduction in it, but this increases the probability of missing an event (SIS). To stabilize the latter, it is necessary to reduce $p_{\text{lт}.i},\ i = 1, \dots, Z$ by increasing the energy accumulation duration of the signal-processing system (SIS) when analyzing each time-frequency interval, with a corresponding increase in the threshold level within the detection-processing system (SxP).

In light of the above, let us write down an approximate formula for the calculation $\overline{T_{max}}$. From (7) and (9), (10) it follows that in the case $p_{\text{о}.i} = 0.99, p_{\text{lт}.i} = 10^{-6},\ i = 1, \dots, Z$, $\overline{N_c} = 1$ the sought-after approximate value $\overline{T_{max}}$ составит:

$$\overline{T_{max}} = \overline{T_c} = T_1 + T_{c2Nz_1 \dots z_Z}, \tag{17}$$

where

$$T_{c2Nz_1 \dots z_Z} = \sum_{i=2}^{Z} T_i z_i. \tag{18}$$

Duration of the search and parameter synchronization time for the SIS

To analyze an MFSK (multiple-frequency-shift keying) communication system employing frequency hopping, with a receiver (demodulator) based on SAW (surface acoustic wave) matched filters, we shall determine $T_i,\ i = 1, \dots, Z$ under the influence of a combination of noise, mutual interference, and external interference from other radio systems. Mutual interference occurs when a certain number of subscribers $N_{\text{аб}}$ operates in the same frequency band as the target signal, whose frequency and time-delay parameters need to be determined. We will consider the sum of these interferences as additive white Gaussian noise at the input of the signal-detection/estimation unit. In this case

$$T_1 = T_e N_p S_c, \tag{19}$$

where $N_p = NN_f$ – the total number of elementary symbols (chips) over the duration of the repetition period T_s, accounting for frequency hopping; *N* – the number of such pulses within a single-frequency segment; N_f – the number of frequencies employed; S_c – the number of pulses with duration T_s whose energy is accumulated in the non-coherent integrator (NCI) to achieve the required values $p_{\text{о}.1}$ and $p_{\text{lт}.1}$.

It is obvious that

$$S_c = g_{v.\text{p}}/(g_{v.\text{MF}}/\xi_{\text{AD+NC}}), \quad (20)$$

где $g_{v.\text{p}}$ – othe signal-to-interference power ratio at the input of the processing unit in the detection system, required for detecting the target with specified $p_{\text{o.1}}$ and $p_{\text{lт.1}}$; $g_{\text{вых.СФ}}$ – signal-to-interference power ratio at the output of the matched filter, $\xi_{\text{AD+NC}}$ – power losses in the amplitude detector (AD) and during digital energy accumulation of the SLS. The issue of calculating the signal-to-noise gain when processing the SLS using a convolution unit or SF has been discussed in detail in the literature. In this case, it is necessary to take into account the losses arising from the mismatch of the frequency bands occupied by the received DFS-PSK SLS and SF, taking into account the number of these filters covering the uncertainty region of the SLS in frequency, losses due to technological inaccuracies in the manufacture of the SF, losses when summing signals from the outputs of different SF. Then, having determined $g_{v.\text{MF}}$ under known conditions N, p, N_c, $p_{\text{o.1}}$, $p_{\text{lт.1}}$ based on dependency graphs S_c from the power signal-to-noise ratio in the case of post-detection digital integration, we can then determine S_c.

It is obvious that

$$T_i = T_{\text{F}.i} + T_{\text{AC}.i},\ i = 1, \dots, Z, \quad (21)$$

where

$$T_{F.i} = 3{,}5/(0.5\Delta f_{\text{A}.i})\ - \quad (22)$$

the duration of the transient process in a PLL loop, given that the carrier frequency of the signal of interest (SOI) falls within its capture range (it is assumed that the bandwidth of the PLL system is equal to the frequency bandwidth of the SOI uncertainty interval under analysis, and that the bandwidth of the loop filter is less than the hold-in range of the PLL system),

$$T_{\text{AD}.i} = T_S g_{\text{v.AD.P}.i}/g_{v.\text{AD}.i}\ - \quad (23)$$

– the duration of the quasi-coherent energy accumulation of the SLS (signal-like sequences) in the LPF (low-pass filter) preceding the RU_{SP} (matched-filter-based detector) (Fig. 9) at the *i*-th stage of the search cycle $g_{\text{v.AD.P}.i}$ – input power signal-to-noise ratio РУ_{AD}, necessary for the detection of SIS with specified $p_{\text{o}.i}$ and $l, i = 1, \dots, Z$, $g_{\text{вх.СхП}.i}$ – signal-to-noise power ratio at the input of the signal-processing unit.

When analyzing the meaning $g_{\text{v.AD}.i}$ It is necessary to account for the mismatch in frequency and time delay between the reference signal and the received signal within the main peak of the correlation function. An expression has been derived for this scenario, assuming the signal synchronization unit (SSU) operates based on the information-bearing signal component (IBSC) and that 10% of the radio transmitter's power is allocated to the synchronization signal component (SSC):

$$\sqrt{g_{\text{v.AD}.i}} = \sqrt{1.8N/(N_{\text{a}} + 2/k_{sh})}\text{sinc}\Delta\varphi_i - 1/\sqrt{\mu_{\tau.i}}, \quad (24)$$

where

$$\Delta\varphi_i = \frac{1}{\sqrt{g_{\text{F.v}.i}}} = \sqrt{\Delta f_{\text{F.v}.i}/g_{\text{v.DD SIS}}NF_{\text{inf}}} \quad (25)$$

– root-mean-square deviation of the phase of the reference signal from the received signal, arising due to the influence of noise within the phase-locked loop (PLL); $g_{\text{F.v}.i}$ – signal-to-noise ratio in terms of power at the output of the PLL ring at the *i*-th stage of the search cycle, $g_{v.\text{DD SIS}}$ – signal-to-noise power ratio at the input of the optical communication system (OCS), $F_{inf} = 1/T_n$ – spectral width of the "compressed" SIS,

$$\mu_{\tau.i} = F_{\text{inf}}/\Delta f_{\text{ATA}.i}, \quad (26)$$

$\Delta f_{\text{ATA}.i}$ – bandwidth of the output filter of the automatic reclosing (AR) circuit (Fig. 9) at the i-th stage of the search cycle.

Example of an approximate calculation of search and synchronization characteristics for a communication link in a satellite radio system

Let us consider the use of a binary PSK spread-spectrum signal with a clock frequency $f_T = 1/T_e$ = 10 MHz and hopping across four frequencies $(N_c = 4)$, so the total occupied frequency bandwidth is approximately 40 MHz. Assume that each pair of matched filters (MFs), designed to detect a segment of the composite signal (CS) at one of the four frequencies, is matched to that segment – a segment generated based on a pseudorandom sequence (PRS) of a certain length $N = 2048$, that is, for each of the two SFs, the length of the pseudorandom sequence (PRS) is $N_{\text{cer}} = 1024$. In this configuration, each SAW-based matched filter (MF) consists of two series-connected substrates, each designed to process a segment of the composite synchronization signal (CSS) formed using a 512-chip pseudorandom sequence (PRS). Consequently, the total length of the PRS segment used to generate the CSS transmitted at a single frequency is 2048. As noted above, to simplify the detection device, the same binary PRS can be used to generate each segment of the synchronization signal (SS) transmitted at a given frequency. Thus, the length of the PRS over its repetition period, when accounting for the quaternary Welti E-sequence, is $N_{PS} = 512 \cdot 2 \cdot 2 \cdot 4 = 8192$.

Using the parameter values for the synchronization signal (SS) listed above, it is relatively straightforward to estimate the gain in the signal-to-noise ratio (SNR) at the output of an ideal receiver compared to its input. However, additional losses are inevitable due to various factors – some situational, arising from the operating conditions of the detection and synchronization equipment, and others technical in nature. For instance, if a satellite is in a geostationary orbit, the analysis of frequency mismatches must primarily account for instabilities in the master oscillators and the Doppler frequency shift caused by fluctuations in the satellite's orbital position.

In this scenario, the frequency uncertainty range for the SS is approximately 10 kHz. Given that z_1=3 in the case under consideration, the maximum frequency mismatch for each matched filter (MF) will be approximately 3.3 kHz.

Taking into account the shape of the cross-section at the frequency of the main peak of the composite frequency-modulated (FM) signal, the maximum reduction in its power level at the output of the matched filter (MF) is approximately 1.4 times (1.5 dB) compared to the ideal case where there is no frequency mismatch between that peak and the center frequency of the MF's amplitude-frequency characteristic. Another source of signal-to-noise ratio (SNR) loss arises from the pre-detection summation of the MF's responses to different frequencies; however, these segments of the composite signal – originally transmitted at different frequencies – arrive at the input of the signal processing unit (following the receiver's frequency converter) without any phase discontinuity in the high-frequency oscillation, as a single local oscillator is used for all carrier frequencies. Specifically, computer simulations have shown that if the arithmetic mean of the signal frequencies at the MF output is at least 4-5 times greater than the spectral width of the multi-frequency composite signal – a condition met in this instance – then the power-based SNR loss is no more than 2.5-3 dB, compared to the case of a single-frequency signal with a time-bandwidth product (base) of 8192.

Losses resulting from manufacturing inaccuracies in SAW filters typically do not exceed 0.7 dB, while the cascading of two such filters – due to the bandwidth limitations of the delay lines – leads to additional losses on the order of 2 dB.

Summing up the losses in the signal-to-noise ratio by power caused by the combination of the above factors, we obtain their value of approximately 7 dB, that is, the signal-to-noise ratio by power at the input of the NC will be approximately $\xi_{\Sigma\text{DSD}} = 7\ \text{dB}$ lower, compared to the case of ideal coherent energy accumulation in a communication system – specifically, given a certain number of simultaneously active users within a shared frequency band $N_\text{s} = 200$ and the signal-to-noise ratio at the receiver input $k_{sh} = 0.01$ will amount to $g_{v.\text{SF}} = \frac{1.8PS}{\left[\left(N_s+\frac{2}{sh}\right)\xi_{\Sigma\text{DSD}}\right]} = \frac{0{,}004\cdot 8192}{5} = 6.5$ times.

The required number of signal-plus-noise (S+N) periods to be accumulated at the detection center (post-amplitude detector) for a given detection reliability ($p_{\text{o.1}} = 0.99$, $p_{\text{lт.1}} = 10^{-6}$), will be drawn up in accordance with $c \approx 30$, and the total losses due to detection and digital accumulation will be on the order of 6 dB. Then $T_1 = N_{\text{PS}}\left(\frac{1}{f_T}\right)S_c \approx 12.2$ mc.

The dimensions of the cross-section of the DCF at the output frequency of the UOSLS will be $1/N_{\text{cer}}T_e = (1/1024)\cdot 10\text{MHz} \approx 10\text{kHz}$. Considering the shape of the main peak of the DCF, we will assume that using three SFs with a frequency spacing of 3.3 kHz will allow us to reduce the width of the frequency uncertainty region to this value. Further,

assuming that $F_2 = 3.3\ \text{kHz}$ and the dynamics of the change in the frequency of the SLS is such that $\Delta f_{\text{F}.i}$ cannot be less than 250 kHz, and since the loop filter bandwidth cannot be varied arbitrarily, we shall limit our consideration in this case to two stages: detection and synchronization of the slave system (SIS) using a PLL-based search mechanism that incorporates a loop filter with a specific bandwidth $\Delta f_{\text{F}.2} = 250$ кГц. Then $z_2 = \frac{F_2}{\Delta f_{\text{F}.2}} - 1 = 12$, and the duration of the time required to eliminate the frequency mismatch in a PLL will be $T_{\text{F}.2} = \frac{3{,}5}{0{,}5\Delta f_{\text{F}.2}} = 30$ mc.

In the event that the PLL circuit has entered the lock-in (tracking) mode, the root-mean-square deviation of the initial phase of the received signal from the initial phase of the signal at the output of the PLL's controlled oscillator (Fig. 9) is determined in accordance with (25), that is,$\Delta\varphi_2 = \sqrt{\Delta f_{\text{F}.2}/g_{\text{v.AD}}NF_{\text{inf}}} = \left(\frac{250}{0{,}01.20.10^6}\right)^{1/2} = 0{,}05$ rad. In this case, at the input of the СхП at $\mu_{\tau.2} = 200$, the power signal-to-noise ratio value has been calculated: $g_{v.\text{AD}.2} = \left[\sqrt{1{,}8N/(N_{\text{s}} + 2/k_{sh})}\text{sinc}\Delta\varphi_2 - 1/\sqrt{\mu_{\tau 2}}\right]^2 = \left[\sqrt{1{,}8.2040/(200 + 2/0{,}01)}\ \text{sinc}\ 0{,}05 - 1/\sqrt{200}\right]^2 = 11{,}6$. Then, according to (23), we obtain: $T_{\text{AD}.2} \approx 5$ mc.

Thus, the estimation of the approximate resultant value $\overline{T_{max}}$ in accordance with (17), is defined by the formula: $\overline{T_{max}} = \overline{T_c} = T_1 + \sum_{i=2}^{Z} T_i z_i = 12.2 + (30 + 5) \cdot 12 \approx 0.43(\text{c})$.

Of practical interest is an investigation into how the approximate estimate of the maximum time required for the detection and synchronization of a spread-spectrum signal (SSS) depends on a multi-stage parallel-sequential search procedure for its frequency and time-delay parameters, where the bandwidth of the phase-locked loop (PLL) filter varies from one stage to the next. The results of this investigation are presented in Figure 11. In calculating the plots, it was assumed that z_1=3 remains constant, and that for all other values of i, the values of z_i remain the same throughout all stages of the search cycle – with the exception of the final stage, where the value of z_Z is determined by the minimum allowable bandwidth of the loop filter, which is assumed to be 250 Hz. For example, if $z_2 = 3$, then the bandwidth of the loop filter at the second stage of the search cycle at the level of 0.7 will be 1100 Hz, at the third at $z_3 = 3$ this width will be equal to 367 Hz, and at the last stage of the search cycle z_4=2, and the last analyzed frequency band will be equal to (367-250) Hz = 117 Hz.

Figure 11 has an additional lower scale on the abscissa axis, which indicates the total number of stages of the search cycle when selecting the number of frequency intervals analyzed in the PLL at each stage. We emphasize that $\Delta f_{\text{ФАПЧ}.Z}$ in any case does not exceed 250 Hz. As a result, if z_i is changing from 3 to 11, the value of Z does not change and is equal to 3. Values $\overline{T_{max}}$, marked with asterisks in Figure 11, correspond $Z = 3$, $z_1 = 3$, $z_2 = 4$, $z_3 = 5$, that is, to different values of z_i, and they are not related to the curves shown in this figure. The straight horizontal line with asterisks in Figure 11 corresponds to

the case of a sequential correlation search for a given signal (SIS), involving the successive analysis of time-frequency intervals with a duration of $T_e/2$ and a frequency bandwidth of 250 Hz. In this scenario, the power loss of the signal at the input of the processing unit (RU) is due solely to the Doppler frequency shift. As in the case of the parallel-sequential search, it was assumed here that $N_a = 200$.

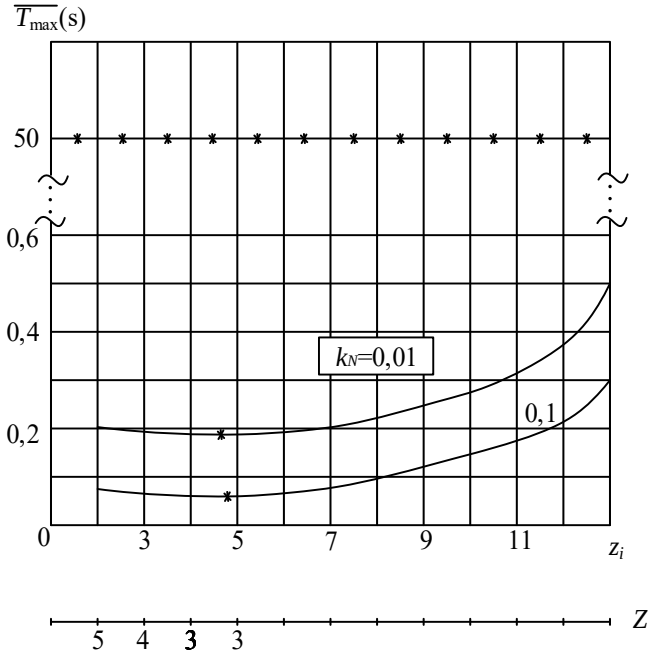


Fig. 11. Duration of the acquisition and synchronization process for a PSK-modulated frequency-hopping spread-spectrum (FHSS) signal – using a four-frequency hopping pattern and a multi-stage parallel-serial search – as a function of the number of frequency intervals analyzed at each stage of the cycle

Thus, as follows from the analysis of Figure 11, it is possible to optimize the duration of the SIS (slave system) detection and synchronization process by selecting the number of stages in its multi-stage parallel-sequential search procedure. For instance, this duration can be reduced to approximately 0.2 s by choosing $z_i = 4$. In case of using sequential correlation search the value $\overline{T_{max}}$ under the same initial conditions, they amount to several tens of seconds.

Conclusion

1. To address a wide range of challenges related to the acquisition and synchronization of low-power, noise-like signals (NLS) in various types of satellite radio systems, it is advisable to employ general principles for designing algorithms and corresponding hardware capable of estimating NLS frequency and time-delay parameters

with a specified level of accuracy and reliability.

2. It is advantageous to utilize a multi-stage, parallel-sequential procedure for NLS parameter acquisition. This procedure relies on the long-term integration of signal energy, implemented via digital convolution – using either dedicated digital convolution units or matched filters (MF) – between the received signals and their local references. Such an approach ensures the necessary performance for energy-based detectors, even in the presence of high-power interference, with subsequent refinement of the NLS parameters achieved through phase-locked loop (PLL) and delay-locked loop (DLL) acquisition schemes.

3. An acquisition system based on digital convolution is capable of processing pseudorandom sequences (PRS) of significant length and provides high resolution during the initial NLS detection phase. Consequently, it is well-suited for detecting multiple instances of the same NLS – or signals with different structures – that may be present simultaneously at the receiver input with varying frequency and time-delay offsets. Once all NLS have been detected, a dedicated tracking unit – comprising interconnected PLL and DLL systems – should be assigned to each signal. The initial acquisition procedure only needs to be re-initiated if tracking is lost for any of the detected signals.

4. The use of analog surface acoustic wave (SAW) matched filters for the initial accumulation of synchronization signal (SS) energy limits the duration of this accumulation process; consequently, a subsequent digital post-detection integrator plays a significant role. These factors result in lower resolution for this configuration compared to the previously discussed design for the primary SS detection unit. Therefore, its application is considered specifically for satellite communication systems employing direct-sequence spread-spectrum phase-shift keying (DSSS-PSK) synchronization signals – specifically for detecting a single, low-power synchronization signal shared by all system users.

5. Research indicates that a multi-stage, parallel-serial method – developed for satellite radio systems utilizing noise-like (spread-spectrum) synchronization signals – enables the simultaneous detection and parameter estimation of these signals. This approach reduces the time required for the processing equipment to achieve synchronization by several hundred times compared to a sequential correlation search. In particular, by optimally distributing transmitter power between the information-bearing signal and the synchronization signal – based on the criterion of minimizing the bit error rate for information symbols – the proposed method allows a ground-based receiver in a satellite communication system (using a geostationary transponder) to achieve synchronization in approximately 0.2 seconds, and in any case, no more than 0.5 seconds.

REFERENCES

[1] N.I. Smirnov, S.F. Gorgadze, “Duration of the Synchronization Acquisition Process for a Receiver of Complex Noise-Like Signals in an Asynchronous Satellite Information Transmission System,” *Foreign Radio Electronics*. 1997. No. 5, pp. 41-51.

[2] N.I. Smirnov, S.F. Gorgadze, “Accelerated Detection of Ultra-Long Pseudorandom Sequences in Satellite Personal Radio Communication Systems with Synchronous Code-Division Multiple Access,” *Elektrosvyaz*. 1998. No. 5, pp. 14-18.

[3] N.I. Smirnov, S.F. Gorgadze, “Accelerated Detection of Ultra-Long Synchronization Signals and Identification of Subscriber Stations in Satellite Personal Radio Communication Systems with Synchronous Code-Division Multiple Access,” *Radiotekhnika i Elektronika*. 1998. No. 12, pp. 1495-1504.

[4] N.I. Smirnov, S.F. Gorgadze, “Methods for Initial Synchronization in Third-Generation Mobile and Satellite Communication Systems with Code-Division Multiple Access (CDMA),” *Elektrosvyaz*. 2001. No. 6, pp. 37-39.

[5] S.F. Gorgadze, “Detection and Discrimination of Complex Address Signals in Code-Division Multiple Access Systems Using Fast Spectral Transforms,” *Radiotekhnika i Elektronika*. 2006. No. 4, pp. 428-436.

[6] S.F. Gorgadze, “Complex composite signals with a constant amplitude envelope for satellite radio navigation systems,” *Radiotekhnika i Elektronika*. 2017. Vol. 62. No. 4, pp. 317-331.

[7] Smirnov, N. I., & Karavayev, Yu. A. Comparison of implementations of microelectronic units for complex signal detection // Radioelectronics (Radioelektronika). 1982. No. 7, pp. 22-27.

[8] S. F. Gorgadze, V. V. Boykov, “Measurement signals with multi-position subcarriers for satellite radio navigation systems,” *Radiotekhnika i Elektronika*. 2014. Vol. 59. No. 3, p. 264.

[9] D. Morgan, “Surface Acoustic Wave (SAW) Signal Processing Devices,” Moscow: Radio i Svyaz, 1990. 416 p.

[10] S. F. Gorgadze, Sh. D. Vu, “Detection and synchronization of low-power noise-like signals in a satellite radio system,” *T-Comm*. 2023. Vol. 17. No. 8, pp. 4-20. DOI: 10.36724/2072-8735-2023-17-8-4-20

[11] N. I. Smirnov, S. F. Gorgadze, “Synchronization acquisition time for a receiver of complex noise-like signals in an asynchronous satellite information transmission system,” *Zarubezhnaya Radioelektronika*. 1997. No. 5, pp. 41-51.

[12] L. E. Varakin, “Communication Systems Using Noise-Like Signals,” Moscow: Radio i Svyaz, 1985. 384 p.

[13] Sh. D. Vu, S. F. Gorgadze, “Device for Accelerated Search of a Noise-Like Signal,” *Information Society Technologies. Proceedings of the XVI International Industry-Specific Scientific and Technical Conference*. Moscow, 2022, pp. 88-90.

[14] V. I. Tikhonov, “Optimal Signal Reception,” Moscow: Radio i Svyaz, 1983. 320 p.

[15] V. I. Kulakova, “Detection of Weak Signals via Cross-Correlation with Compensation for Phase Instabilities in the Radio Monitoring of Frequency Resources for Satellite Communication Systems,” *Control, Communication and Security Systems*. 2020. No. 1, pp. 33-48.

[16] Yu. S. Lezin, “Optimal Filters and Integrators for Pulse Signals,” Moscow: Sovetskoye Radio, 1963. 320 p.

[17] Sh. D. Vu, S. F. Gorgadze, “Probabilistic Characteristics of the Accelerated Search for Noise-Like Signals,” *Telecommunications and Information Technologies*, 2022. Vol. 9, No. 2, pp. 120–127.

[18] I. Zelenka, “Piezoelectric Resonators Based on Bulk and Surface Acoustic Waves,” Moscow: Mir, 1990. 584 p.

[19] M. Matthews, “Surface Acoustic Wave Filters,” Moscow: Radio i Svyaz, 1981. 472 p.

SYNCHROINFO JOURNAL

www.media-publisher.eu/synchroinfo-journal

ARTIFICIAL INTELLIGENCE IN THE URBAN ENVIRONMENT: EXAMPLES OF TECHNOLOGY APPLICATIONS. Part I

Angelina Bott [1]

[1] Institute of Radio and Information Systems (IRIS), Vienna, Austria;

iris@media-publisher.eu

Overview of report materials based on the Global Initiative on AI and Virtual Worlds – Disco ering the Citiverse [1-6]

ABSTRACT

This overview is based on the document "The AI-Enabled Citiverse: Use Cases for Cities in the Age of AI" and focuses on a critical phase in urban development. Across the globe, major cities are transitioning from pilot projects and proof-of-concept initiatives to the full-scale implementation of artificial intelligence, digital twins, and immersive technologies. These tools are reshaping approaches to urban planning and management, while also transforming how people interact with the urban environment. This process is examined through the lens of both existing and prospective use cases. The authors propose a methodology for identifying and evaluating AI applications within urban settings, providing an overview of the underlying approaches and specific examples of technology deployment. The review covers key domains, including urban planning, infrastructure, governance, economic development, education, tourism, transport, and mobility. Separate sections address public safety, healthcare, and disaster resilience. The overview presents AI use cases across five urban sectors and outlines the potential for scaling, the level of impact, feasibility, and the risks associated with integrating AI into the urban environment. The first part of the review examines the application of artificial intelligence in the urban environment within the scope of the "Services and Public Participation" area.

KEYWORDS: *Artificial intelligence, Strategic Blueprint, Digital twins, Urban planning, City administration services, Economic development, Transport and mobility.*

DOI: 10.36724/2664-066X-2026-12-4-68-91

Received: 12.05.2026
Accepted: 25.07.2026

Citation: Angelina Bott, "Artificial Intelligence in the Urban Environment: Examples of Technology Applications. Part I," *Synchroinfo Journal* **2026**, vol. 12, no. 4, pp. 68-91.

Licensee IRIS, Vienna, Austria.

This article is an open access article distributed under the terms and conditions of the Creative Commons Attribution (CC BY) license (https://creativecommons.org/licenses/by/4.0/).

Copyright: © 2026 by the authors.

Introduction



Cities that view the concept of an "AI-enabled citiverse" merely as a theoretical possibility risk finding themselves in a situation where their management systems have already been predetermined by someone else. The convergence of artificial intelligence, spatial computing, digital twins, and immersive environments has reached a level of maturity that allows for their integration into urban infrastructure. This overview outlines the methodology for identifying and evaluating examples of the "AI-enabled citiverse" concept being implemented around the world [1-6]. These examples are examined in detail across five thematic sections, compiled in the collection titled "The AI-Enabled Citiverse: Use Cases for Cities in the Age of Artificial Intelligence." The areas covered include:

• Urban planning, the creation of high-quality urban environments, and infrastructure: this area focuses on the use of AI technologies to transform approaches to developing livable spaces and urban environments.

• Urban overnance and public participation.

• Economic development, education, and tourism: focused on leveraging AI-driven digital urban environments to provide immersive, personalized learning, foster sustainable urban economic development, and promote sustainable tourism.

• Transport and mobility

• Public safety, healthcare, and disaster resilience.

The use cases presented were selected by an international working group of experts, including representatives from academia, municipal governments, NGOs, small and medium-sized enterprises (SMEs), and industry specialists. This is not merely a catalog of technological solutions, but a structured tool for assessing the opportunities, risks, and maturity levels of innovative technologies. It will help cities identify scenarios that are already implemented, solutions currently undergoing pilot testing, and concepts that are still in the exploratory phase.

These use cases are intended to:

• Identify innovative solutions based on technologies such as artificial intelligence (AI), augmented and virtual reality (AR/VR), digital twins, the Internet of Things (IoT), and the metaverse, while highlighting their vast potential across a wide range of sectors.

• Showc se international best practices.

• Establish a foundation for developing other aspects of this initiative – for instance, in areas such as emerging technologies, security and trust, as well as digital inclusion and accessibility.

The collection of examples presented here offers a snapshot of current innovations and serves as a cornerstone for future collaboration.

Methodology

The methodology combined literature review, expert assessments, stakeholder input, and prospective analysis to select and classify use cases across key thematic areas. During the initial phase of the work, the primary focus was on gathering a wide range of use cases for each thematic area from various sources.

A list of use cases covering five thematic areas was compiled. To create a shortlist for each area (consisting of approximately 10 cases), the working group evaluated them based on four key criteria approved by the "Global Initiative on AI and Virtual Worlds – Citiverse Concept Exploration" community: alignment with the Sustainable Development Goals (SDGs), scalability, significance of impact, and feasibility (Table 1).

Table 1

AI-Enabled Citiverse Use Case Scoring Criteria

Scoring Criteria	Key Questions
1. Alig ent with SDGs	To what extent does this use case contribute to one or more SDG targets?
2. Scal ility	How relevant is this use case for multiple cities and how easily can it be replicated and scaled?
3. Impa	How impactful will the case study be for social, economic and environmental outcomes?
4. Feasi lity	What are the long-term maintenance and resource requirements? What is the time to value?

Each expert assigned a score for each criterion on a scale from 1 to 10. The cases with the highest scores were included in the final shortlist for each thematic group, while also ensuring a diverse range of examples that cover key focus areas.

To illustrate the level of maturity and the implementation timelines for various use cases, each has been assigned to one of three horizons:

1: Mature solutions that are already being deployed in real-world urban environments.

2: Emerging use cases for which successful pilot projects or initial implementation phases already exist.

3: Conceptual or experimental use cases that hold significant long-term potential but are not yet ready for practical application. No specific implementation examples (case studies) are provided for this horizon, as these solutions are still in the "discovery" phase.

This classification enables cities to distinguish between opportunities for short-term implementation, projects that should be incorporated into innovation and pilot-testing roadmaps, and forward-looking innovations that require further research.

Each use case was also evaluated across four risk dimensions, helping cities identify implementation challenges and the measures required to mitigate them:

• Public safety.

• Stake older acceptance.

• Privacy a d data security.

• Fina cial and operational risks.

Risk levels were classified as low, medium, or high, based on available data and expert assessments. This analysis enables cities to proactively identify key issues that must be addressed prior to implementation.

For each use case, key technologies were also selected, and a preliminary list was compiled (Table 2).

Table 2

Definitions

Technology	Definition	Reference
Metaverse	An integrative ecosystem of virtual worlds offering immersive experiences to users, that modifies pre-existing and creates new value from economic, environmental, social and cultural perspectives. NOTE – A metaverse can be virtual, augmented, representative of, or associated with, the physical world.	FGMV-20
Digital twin	A digital twin network is a digital representation of an object of interest.	ITU-T Y.4600
Augmented reality (AR)	An environment containing real and virtual sensory components. The augmented reality continuum runs from virtual content that is clearly overlaid on a real environment (assisted reality) to virtual content that is seamlessly integrated and interacts with a real environment (mixed reality).	ITU-T P.1320
Virtual reality (VR)	An environment that is fully generated by digital means. To qualify as virtual reality, the virtual environment should differ from the local environment.	ITU-T P.1320
Mixed reality (MR)	An environment containing real and virtual components that are seamlessly integrated and interact with each other in a natural way (one end of the augmented reality continuum).	ITU-T P.1320
Internet of Things (IoT)	A global infrastructure for the information society, enabling advanced services by interconnecting (physical and virtual) things based on existing and evolving interoperable information and communication technologies.	ITU-T Y.4000
Artificial intelligence (AI)	Computerized system that uses cognition to understand information and solve problems.	ITU-T M.3080
Generative AI (GAI)	GAI refers to a broad field of research and development that focuses on creating intelligent systems that can generate new, original content such as images, videos, music, text and even entire conversations. These systems use machine learning algorithms to learn patterns and structures within the data they are trained on and then use this knowledge to generate new content that resembles the original data, but is not necessarily identical to it.	FGMV-22

Overall use cases for cities in the age of AI

This section provides an overview of practical examples covering five key topics relevant to municipal authorities and stakeholders.

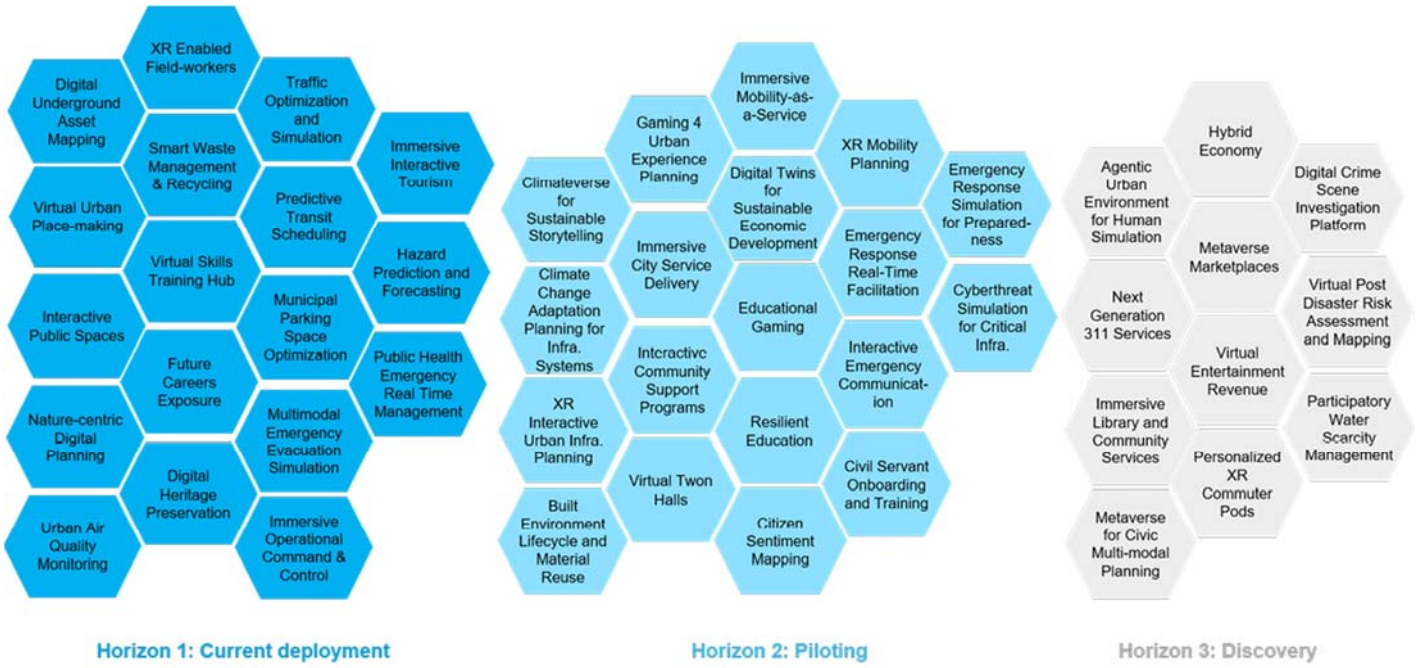


Fig. 1. Overall use case overview and horizon mapping [1]

Source: AI-enabled Citiverse: Use Cases for Cities in the Age of AI: Introduction, 2026

The "cityverse" concept enables cities to create immersive digital representations of their urban environments, bridging the physical and virtual worlds through technologies such as the metaverse, digital twins, augmented and virtual reality (AR/VR), artificial intelligence (AI), and the Internet of Things (IoT). AI – particularly generative AI – increasingly serves as a foundational technology that drives innovation, enhances user experience, and facilitates the creation of interactive, immersive virtual environments. As autonomous intelligent agents ("Agentic AI") continue to evolve, it is also essential to examine their impact on virtual-world technologies and their potential use cases.

Research indicates that AI-powered "cityverses" are not merely a technological novelty, but a fundamental infrastructure for managing cities in the 21st century. Cities that have implemented such solutions are already seeing tangible results: in Seoul, a digital-twin-based traffic management system has reduced emergency response times by 20%; the "Virtual Helsinki" project attracted over 1 million users during the COVID-19 lockdowns; and the UK's National Underground Asset Register now integrates data from 267 infrastructure owners, covering more than 40% of the entire national infrastructure network. These examples confirm that AI-enabled "cityverses" are a vital tool for addressing complex urban challenges on a large scale.

In every domain, AI-enabled Citiverse is used to address unique challenges – ranging from climate change adaptation and circular economy initiatives to citizen engagement and emergency management. The cross-sectoral nature of these applications demonstrates the versatility of AI-enabled Citiverse as a platform for problem-solving. For instance, digital twins serve urban planners in visualizing infrastructure, emergency responders in simulating natural disasters, and citizens in accessing immersive educational and cultural experiences.

Cities must balance risks and opportunities when implementing artificial intelligence use cases on a citywide scale. A systematic risk library – covering public safety, stakeholder acceptance, data privacy/security, and financial/operational risks – enables cities to prioritize use cases that strike a balance between innovation and manageable risk. This approach supports informed decision-making, ensuring that high-impact, scalable solutions are prioritized for early adoption, while more experimental or higher-risk concepts are piloted or studied in greater depth before being deployed across the entire city.

Research indicates that most risks to public safety are low to moderate; in fact, virtual environments often enhance rather than diminish safety by improving training, simulation, and coordination capabilities. However, data privacy and cybersecurity risks require ongoing attention, particularly for applications that process sensitive infrastructure-related, personal, or financial data.

Experience gained from various initiatives in the realm of digital urban spaces highlights several key success factors, including:

Implementing open standards and ensuring interoperability: The success of projects in this field depends on the development and adoption of unified data models, APIs, and semantic structures that enable seamless information exchange across different platforms. The UK's NUAR project clearly demonstrated the effectiveness of using a common international data model for underground infrastructure (MUDDI), which brought together 267 asset owners and numerous agencies into a single "digital twin." Focusing on open standards from the early stages helps cities avoid data silos, accelerates the replication of solutions, and reduces dependency on specific technology vendors. ITU-T Study Group 20 – which focuses on the Internet of Things, digital twins, and smart, sustainable cities and communities – is developing international standards for an AI-driven "cityverse." These standards serve as a global framework for ensuring interoperability, trust, and scalability for solutions across cities, industries, and government entities.

Establishing robust and flexible governance mechanisms: Beyond the technological aspects, it is essential to develop governance structures that effectively allocate roles, responsibilities, and risks throughout a project's entire lifecycle. The success of the digital twins within Copenhagen's "Street Lab" initiative stems from active collaboration among municipal services, private operators, and academic partners, who jointly make decisions and share responsibility for data management. Establishing clear governance rules – covering issues such as data ownership, quality control, and change management – Is fundamental to the long-term sustainability of such projects. Developing multilateral cooperation and engagement: No single organization can create a "cityverse" on its own. The success of the Metaverse Seoul project was made possible through the collaborative efforts of city authorities, public associations, technology companies, and civil society.

Phased implementation through pilot projects: a step-by-step rollout reduces risks and builds momentum. The CReDo project in the UK began with targeted pilot projects focused on addressing the impacts of flooding, later expanding to include resilience planning for various infrastructure assets.

Balancing technical infrastructure with organizational change management: technologies such as digital twins and immersive XR platforms may require significant infrastructure investment – including 3D modeling, cloud services, and sensor networks – but technology alone is not enough to achieve results. The Nottingham City Council's digital twin initiative integrated specialized organizational change management teams to help developers, planners, and the public adapt to new workflows. Dedicated resources

for change management – such as training, communication plans, and feedback channels – are j st as essential as servers and software.

Prioritizing security, privacy, and trust by design: several AI use cases within the "Citiverse" integrate personal data, infrastructure data, and Internet of Things (IoT) data. Embedding security and privacy at every level – through network segmentation, end-to-end encryption, consent-based data sharing, and role-based access control – ensures resilience against breaches.

Iterative improvement relies on real-time performance data and structured evaluations. Seoul's traffic digital twin reduced emergency response times by 20 percent by continuously refining its AI models based on feedback from real-time sensors. An inclusive and accessible approach to design: while an AI-enabled urban environment has the potential to democratize participation, it also risks excluding individuals with low digital literacy, limited access to devices, visual impairments, or neurodivergence. Implementing universal design principles – such as supporting multiple input methods, low-bandwidth modes, and multilingual interfaces, among other design considerations – can help mitigate these issues.

Virtual environments can democratize participation by removing the geographical, temporal, and accessibility constraints that have traditionally excluded vulnerable populations from urban planning processes. Seoul's "Metaverse Seoul" platform and initiatives in Barcelona focused on mapping citizen sentiment demonstrate how digital platforms can amplify the voices of previously marginalized groups within municipal decision-making.

Digital twins and AI-driven analytics are transforming maintenance from a reactive approach to predictive management, thereby reducing costs and enhancing service reliability.

Climate adaptation is emerging as a critical area of application; digital twins allow cities to simulate flood scenarios, optimize the placement of green infrastructure, and coordinate the responses of various departments to extreme weather events. The CReDo project in the United Kingdom illustrates how cross-sectoral data sharing via digital twins strengthens collective resilience to climate risks, while simultaneously facilitating more effective capital investment decisions.

Immersive educational platforms prove particularly effective in complex, high-risk, or costly learning environments. Such applications support formal education systems as well as the continuous professional development of municipal staff.

They foster economic diversification and cultural preservation; an AI-enabled urban environment opens new avenues for economic growth through virtual marketplaces, immersive tourism, digital heritage conservation, and support for creative industries. These use cases contribute to local economic resilience, cultural continuity, and global accessibility, while simultaneously reducing the environmental impact associated with physical tourism and commerce.

Virtual tourism platforms show significant potential for cultural sites facing the pressures of overtourism or climate-related threats. Digital heritage preservation projects create permanent records of vulnerable sites while generating new revenue streams through virtual experiences. Global digital heritage initiatives and various virtual museums demonstrate how cities can preserve cultural assets while expanding global access to local

heritage – creating sustainable tourism models that benefit communities without overburdening physical infrastructure.

They promote sustainable development across all facets of urban life: from nature-inclusive mapping and design, the advancement of a circular economy, and waste management, to the provision of educational opportunities – including the gamification of sustainable behaviors and the simulation of climate change adaptation strategies.

Educational gaming platforms, such as Scubaverse, illustrate how immersive experiences can enhance environmental awareness and drive behavioral change on a large scale. Digital twins support circular economy initiatives by tracking material flows, optimizing waste collection routes, and enabling collaborative planning to improve resource efficiency.

Art and culture programs in virtual environments enable the creation of new forms of creative self-expression while preserving traditional cultural practices. The integration of live musical performances in a virtual version of Helsinki – combined with interactive city exploration – and experiments in the virtual creation of public spaces at the Burning Man festival demonstrate how digital environments can complement, rather than replace, physical cultural experiences. These initiatives foster hybrid models that expand access while maintaining authentic community connections.

In the future, the convergence of an AI-powered virtual universe with emerging technologies – such as advanced artificial intelligence and quantum computing – will pave the way for even more sophisticated applications.

City Administration and Services

This section examines how an AI-enabled "citiverse" – and related technologies - can help cities deliver services more quickly, make them more accessible, and better tailor them to the needs of diverse population groups [2]. It provides a brief overview of solutions that leverage AI and allied technologies to improve public service delivery, enhance civic engagement, support the sustainable functioning of a city, and strengthen transparency and accountability.

Figures 2 and 3 illustrates the overall landscape of potential use cases and their future development. It highlights the interconnections between various sectors and demonstrates how advanced technologies can be applied across a wide range of aspects of urban life. Within this broad framework, this report focuses on thematic areas such as urban governance, service delivery, and public engagement. It examines key technologies that drive innovation, the implications of their implementation, and specific real-world examples.

Cities are increasingly adopting digital technologies to transform governance, improve public and municipal services, and expand citizen participation in urban life.



Fig. 2. Overall use case overview [2]

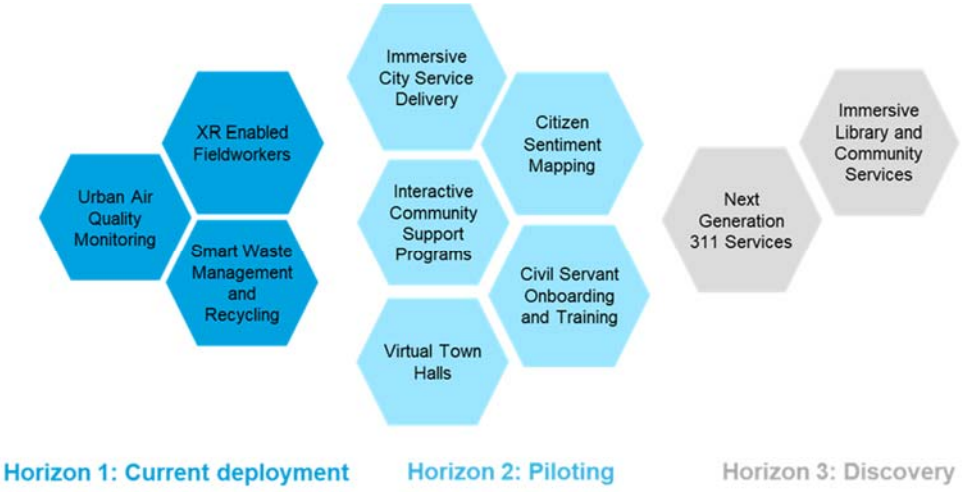


Fig. 3. City Administration, Services and Public Participation Use Case Overview and Horizon Mapping [2]

The thematic area of "Urban Governance, Services, and Citizen Participation" focuses on the use of digital technologies – such as artificial intelligence (AI), virtual reality (VR), augmented reality (AR), and digital twins – to reshape city management, enhance service quality, and foster active resident engagement. Practical applications include:

• Delivery of public and municipal services: increasing the accessibility and efficiency of processes such as tax administration, permit issuance, licensing, and social support.

• Citizen interaction, participation, and co-creation: establishing platforms for more inclusive, interactive, and meaningful resident involvement in city life.

• Sustainable urban functioning: initiatives to monitor and support the transition toward "net-zero" emissions, as well as promoting the efficient use of resources and the implementation of circular economy principles – for instance, measures to improve air quality and enhance waste management systems.

• Transparency and accountability.

City Administration, Services, and Public Participation

Case 1: Smart Waste Management and Recycling

AI-enabled urban environment technologies, such as digital twins, can be used to create an interactive digital platform for managing the collection and recycling of urban waste in residential and commercial areas.

Impact

1) Emission reduction: Optimizing waste collection routes and schedules using AI and real-time digital twin data significantly lowers fuel consumption for waste collection vehicles. More efficient waste collection leads to a cleaner, better-maintained urban environment, with fewer overflowing bins, less litter, and reduced unpleasant odors. This makes areas less attractive to pests and eases traffic congestion caused by collection vehicles, contributing to safer and more pleasant public spaces.

2) Biodiversity: Reducing illegal dumping and increasing recycling rates helps decrease pollution and the disruption of habitats within urban green spaces.

3) Pedestrian accessibility: Keeping sidewalks and public spaces clean, while minimizing the presence of waste collection vehicles through dynamic route planning, fosters a more pedestrian-friendly environment.

4) Health and well-being: Lowering the accumulation of waste reduces exposure to harmful bacteria, pests, and airborne pollutants.

5) Citizen engagement: Interactive digital twin platforms empower residents by providing real-time feedback on their recycling efforts, the status of waste containers, and available incentives.

Key Technologies

• GenAI: Generative AI can enhance smart waste management by simulating scenarios, optimizing collection routes, and developing targeted citizen engagement campaigns – even when direct data is limited or rapidly changing. It can also generate accessible, multilingual content and summaries within tools such as digital twins, improving understanding and participation among city staff and residents.

• AI: Artificial intelligence can be used to analyze waste generation patterns, predict peak collection times, optimize collection routes, and forecast whether containers are becoming overfilled or underutilized. Machine learning can automate scheduling, suggest resource allocation strategies, and continuously refine routing as urban conditions evolve.

• IoT: Fill-level sensors – utilizing ultrasonic, lidar, or optical technologies – can be embedded in containers to monitor volume, temperature, and tilt status in real time. This enables dynamic data collection on container usage, reduces the need for manual inspections, and provides waste management operators with immediate insights. These

sensors transmit data at frequent intervals and trigger automated alerts in the event of overfilling or unusual activity.

• Computer Vision: Cameras and computer vision systems can be integrated into advanced containers to automatically recognize and separate recyclable materials from general waste.

• Digital Twin: Digital twins offer a centralized, interactive visualization of all waste management assets. This fosters operational efficiency and cross-departmental urban planning by integrating waste streams with other urban infrastructure systems.

Implemented in:

Copenhagen, Denmark; Edinburgh, UK; Bratislava, Slovakia; Nicosia, Cyprus; Barcelona, Spain; Singapore; San Francisco, USA; Amsterdam, Netherlands

Case study: A digital twin including waste management in Copenhagen

Copenhagen (Denmark) is advancing its smart city strategy through a large-scale "digital twin" project, implemented in partnership with Cisco and TDC (Tele Danmark Communications).

As a European capital of "green" digitalization, Copenhagen has launched an ambitious initiative: the creation of an integrated digital platform that aggregates and manages data from various urban infrastructure systems – ranging from lighting and parking to air quality monitoring and waste management. Centered around the Danish Outdoor Living Lab (DOLL) and the Copenhagen Street Lab, the project spans an urban area of over 11 kilometers (7 miles) in the western part of Copenhagen.

This initiative brings together more than 40 different smart city solutions, deployed as a "living laboratory" for testing and demonstrating intelligent urban technologies. Copenhagen's goal of becoming the world's first carbon-neutral capital by 2025 has driven city authorities to adopt data-driven solutions. These enable the optimization of operational processes, cost reduction, and the improvement of public services, all while contributing to the achievement of ambitious climate targets.

The primary objective of the Copenhagen "digital twin" project was to develop a comprehensive, real-time digital model of the city's infrastructure.

The project aimed to deliver several key outcomes:

• Smart city innovation: Strengthening Copenhagen's position as a global leader in smart city technologies by establishing Europe's largest outdoor testing ground for intelligent urban solutions. • Support for carbon neutrality: development of digital tools and analytical capabilities for monitoring, measuring, and optimizing carbon emissions across various municipal services.

• Operational efficiency: implementation of data-driven decision-making processes across various municipal services.

• Economic growth and improved quality of life for residents: creation of new business models and investment opportunities, while simultaneously reducing operational costs. The broader "Copenhagen Connecting" initiative is projected to generate a socio-economic impact of €600 million over the course of its implementation.

The creation of a "digital twin" of Copenhagen was based on a multi-layered architecture that integrates advanced network infrastructure, Internet of Things (IoT) sensors, data analytics tools, and unified management platforms.

• Foundation of the digital infrastructure: The project established a robust digital framework, with the Cisco Smart+Connected Digital Platform serving as the central integration layer. This cloud-based system aggregated data streams from sensors and end-user devices across the city, forming an ecosystem of applications for managing the urban environment via open APIs. TDC provided carrier-grade Wi-Fi and cellular connectivity, ensuring stable data transmission throughout the seven-mile pilot zone.

• Deployment of a sensor network: The project involved the implementation of an extensive network of IoT sensors covering various urban systems. Specifically, for waste management purposes, ultrasonic fill-level sensors were installed in waste containers throughout the area; these monitor the volume, temperature, and orientation (tilt) of the containers in real time. Data from these devices were transmitted via energy-efficient, long-range networks (LoRaWAN, NB-IoT), which minimized power consumption while maintaining reliable connectivity.

• Integrated Analytical Platform: Data from all connected systems flowed into a centralized analytical platform capable of real-time monitoring and predictive analysis. The system integrated environmental monitoring (air quality, noise, temperature), traffic management, parking sensors, smart lighting control, and waste management data into a unified operational view.

• Waste Management Integration: The waste management component utilized smart bin sensors to monitor fill levels and optimize collection routes. When sensors revealed that only 30 percent of traditionally scheduled waste pickups actually involved full bins, the system enabled Copenhagen to shift from a fixed schedule to on-demand waste collection. This data-driven approach was designed to reduce unnecessary collection trips, lower fuel consumption, and decrease CO_2 emissions.

• Stakeholder Engagement: The project involved extensive collaboration among municipal authorities (Copenhagen, Frederikssund, and Albertslund), technology providers (Cisco, TDC), and research institutions. The DOLL Living Lab served as a neutral testing ground where various vendors could showcase their solutions side-by-side, facilitating informed procurement decisions.

Results

The implementation of a "digital twin" in Copenhagen has led to measurable improvements across various operational and environmental areas.

The integrated platform enabled real-time monitoring and management of urban infrastructure within a seven-mile (approximately 11 km) pilot zone. Through a unified dashboard, municipal services gained access to detailed data on lighting systems, parking space utilization, air quality, and the fill levels of waste containers. In practice, the system demonstrated the technical feasibility of consolidating diverse urban infrastructure systems onto a single digital platform.

Although detailed quantitative metrics from the sensors installed in Copenhagen's waste containers are not available, the overall outcomes in waste management indicate significant potential. Approximately 600 waste containers in the city center were equipped with sensors, facilitating predictive waste collection planning and route optimization. Similar projects utilizing Nordsense technology in other cities have resulted in an 80%

reduction in overflowing containers, a 66% decrease in street-cleaning service requests, and a 64% drop in illegal dumping.

The platform contributed to Copenhagen's broader environmental objectives, though specific CO_2 emission reductions attributable solely to the "digital twin" were not separately quantified. Between 2009 and 2022, Copenhagen succeeded in reducing its total CO_2 emissions by 80%. A significant role in this was played by the waste management system developed as part of the city's "Circular Copenhagen" program, which aims to reduce CO_2 emissions by 59,000 tonnes by 2024.

Lessons Learned

• Integration complexity necessitates strong partnerships: The success of Copenhagen's digital twin relied heavily on close collaboration between the municipal government, technology providers, and telecommunications companies. The partnership between Copenhagen, Cisco, and TDC demonstrated that complex "smart city" initiatives require an ongoing commitment from multiple stakeholders, with clearly defined roles and responsibilities.

• Pilot-scale implementation facilitates learning: A seven-mile test zone provided a sufficient scale for verifying technologies while remaining manageable for deployment and troubleshooting. This approach allowed the city to test and refine solutions prior to broader rollout, thereby mitigating the risks associated with a citywide implementation.

• Data quality and sensor maintenance: Maintaining sensor functionality and data quality within diverse urban environments requires constant attention. The success of waste management optimization depends on reliable sensor performance, regular calibration, and robust data management systems.

• Scalability considerations: While the pilot project demonstrated technical feasibility, scaling to larger urban areas requires significant infrastructure investment and organizational change management. The platform architecture developed for DOLL served as a foundation for expansion into other parts of Copenhagen; however, full-scale, citywide implementation remains a multi-year undertaking.

Copenhagen's initiative to create a "digital twin" of the city – focused on waste management and the monitoring of complex urban systems – demonstrates the transformative potential of integrating IoT sensors, data analytics, and cloud platforms into municipal governance. The project has laid a technical foundation for data-driven urban operations, while simultaneously supporting the achievement of Copenhagen's ambitious climate goals. A key strength of this initiative lies in its comprehensive approach.

Case 2: field staff supported by XR technologies

Extended reality (XR) technologies, such as augmented reality (AR) and virtual reality (VR), have the potential to significantly enhance the capabilities of government field personnel – for instance, building or environmental inspectors. Through XR, these staff members can receive real-time remote consultations from experts who are "virtually present" at the site via digital twins and data streams. XR headsets or smart glasses allow critical information – such as schematics, troubleshooting tips, or safety instructions – to be overlaid directly into the user's field of view, enabling them to perform tasks efficiently

while keeping their hands free. VR simulations facilitate staff training in a realistic, immersive environment, where high-risk tasks can be practiced without any actual danger. Furthermore, the integration of artificial intelligence (AI) provides professionals with access to real-time analytics and recommendations, which helps optimize workflows, improve safety, and boost productivity.

Benefits

1) Efficiency: Using augmented/mixed reality (XR) headsets allows field technicians to access equipment documentation – such as manuals for water pumps or valves – directly on-site. This documentation includes detailed repair or replacement instructions, as well as instructional videos. XR technology significantly reduces the time required for equipment repairs and replacements by minimizing the time spent traveling or working in the office.

2) Quality of Life: Implementing this technology improves the quality of life for both technicians and local residents. Staff spend less time commuting between the office and job sites, while residents benefit from faster restoration of services.

Furthermore, XR technology enables municipalities to onboard less experienced staff by providing hands-on, on-the-job training.

3) Increased Operational Readiness: The ability to instantly access essential information when encountering new or unforeseen issues facilitates faster repairs, thereby maximizing the uptime of critical infrastructure.

4) Knowledge Sharing: XR technology allows a more experienced specialist to virtually "join" colleagues working at various locations across the city, regardless of the specific nature of the task at hand.

Key Technologies

• Digital Twins: Infrastructure, along with its associated documentation and video materials, can be stored within a digital twin. This allows users to access precise information about the location of assets and all related data from any remote site.

• R/VR (Augmented and Virtual Reality): To effectively utilize these technologies, cities will require the necessary hardware – such as AR headsets and supporting systems – to ensure that field personnel have access to the data they need while performing tasks on-site.

• IoT (Internet of Things): By integrating IoT devices into critical infrastructure, personnel working on-site can receive real-time updates on the current status of that infrastructure.

Table 3

Risk level: XR-enabled fieldworkers

Risk attribute	Risk rating			Explanation
Public safety	Low	Medium	High	The use case presents a low impact on public safety. However, it can improve the outcomes for public safety due to lower disruption of infrastructure.
Stakeholder acceptance	Low	Medium	High	This use case will have newer training methods, which may reduce acceptance rates at first. Through training and champions, the technology has the potential to have a high acceptance.
Data privacy and security	Low	Medium	High	With the data being stored locally and consists of commonly found documents, and the AR glasses not connecting to a network, reduce the data privacy risks.
Financial/ operational	Low	Medium	High	With all new technologies, costs are still higher than more commonly available technologies on the market. However, adoption is growing which will reduce costs.

Implemented in: Vienna, Austria; Coral Gables, USA; Chandler, USA.

Case study: Vienna AR-enabled building permitting

Every year, more than 13,000 building permit applications are submitted in Vienna; however, due to an outdated, paper-based workflow, the average time to issue a single permit was twelve months. Approximately 200 tons of archived blueprints and a fragmented collection of regulatory requirements made the review process extremely labor-intensive for municipal authorities and opaque for citizens. To address rapid population growth – the number of residents increased by an average of 21,000 per year between 2012 and 2021 – city authorities launched a research project called BRISE Vienna (Building Regulations Information for Submission Envolvement). The project, which received €4.8 million in funding through the EU's "Urban Innovative Actions" program, aimed to create a fully digital, end-to-end permitting process that integrates Building Information Modeling (BIM), artificial intelligence (AI), and augmented reality (AR).

Objectives

The BRISE project pursues four strategic goals:

• To reduce approval times by at least 50% - from 6-12 months down to 3-6 months for standard residential projects.

• To automate regulatory compliance checks by comparing BIM models submitted by applicants against a 3D master model of the city, which incorporates all site-specific building codes and zoning regulations.

• To increase transparency and public trust through augmented reality (AR) visualizations, allowing residents to see exactly what a planned development will look like and how it will affect lighting (e.g., shadows cast) before construction begins.

• Enable regulatory authority specialists to use AR visualizations to gain a deeper understanding of the scale and impact of planned construction work.

• Adapt municipal workflows to future requirements and develop an open BIM data standard.

Approach to the Solution

• OpenBIM-based submission plugin: The municipal authorities provide an IFC plugin that allows architects to export a 3D model of a project – a "building permit application model" – ready for automated compliance checking against building regulations. This eliminates the need for professionals to learn new software tools.

• AI-driven verification system: Machine learning algorithms analyze the submitted model, compare it against Vienna's building codes, and identify non-compliance issues (such as violations regarding the length of evacuation routes or the required number of parking spaces).

• Reference 3D Model (REM): A "digital twin" is created for every cadastral plot within the system, containing data on height restrictions, protected heritage zones, and transport corridors. This enables the immediate detection of conflicts between design proposals and permitted development parameters.

• Augmented Reality (AR) module: Inspectors and local residents can use tablets or HoloLens headsets to overlay approved project volumes onto the actual construction site. This facilitates compliance verification and makes the project more accessible and understandable to the public.

• Pilot project implementation: Between June and December 2022, 13 architectural firms submitted 17 real-world projects through the new system. Concurrently, the relevant municipal department (MA 37) established a dedicated working group to expedite the review of applications and the preparation of feedback.

Results

• Time savings: The review process for digital applications – up to the point of a final decision – took 3-4 months, compared to approximately 8 months for equivalent paper-based submissions. Consequently, the goal of reducing processing time by 50% was achieved.

• Scaling the pilot project: positive feedback from participants prompted 13 additional companies to join the system, demonstrating clear demand for it.

• Scaling potential: internal estimates indicate that a full transition to this system – covering all 13,000 annual requests – would result in savings of 50,000 man-hours and 7 million euros per year.

BRISE Vienna demonstrates how BIM, AI, and augmented reality can be integrated into a unified digital workflow that cuts permit processing times in half, reduces errors, and simplifies planning-related decision-making for citizens. By digitizing applications, automating regulatory compliance checks, and using augmented reality to overlay approvals directly on-site, Vienna has transformed a bureaucratic hurdle that once took a year into a transparent, data-driven service.

Case 3: Next generation 311 Services

"311" services provide citizens with a way to interact with the municipal administration and report issues related to local services and infrastructure. Technologies from the virtual realm are enabling a new generation of "311" services. Digital twins – virtual replicas of the urban environment – are updated in real time using data from sensors, citizen reports, and other incoming information. Mixed reality (MR) technologies allow residents to use smartphones or augmented reality (AR) headsets to scan their surroundings and access information regarding submitted service requests, maintenance schedules, or the progress of repair work.

Key technologies: Digital twin, AR, GenAI and IoT.

Table 3

Risk level: Next generation 311 Services

Risk attribute	Risk rating			Explanation
Public safety	Low	Medium	High	This use case enhances public safety by enabling faster non-emergency response coordination (e.g., addressing potholes and waste accumulation) and proactive infrastructure monitoring, with minimal direct safety risks.
Stakeholder acceptance	Low	Medium	High	While citizens generally welcome improved services, some citizens may resist process/service changes. Many users will also be unfamiliar with MR technologies and require upskilling and public engagement to encourage adoption.
Data privacy and security	Low	Medium	High	Service requests contain location and personal data requiring robust protection. Integration with IoT sensors expands potential attack surfaces needing security measures.
Financial/ operational	Low	Medium	High	This solution requires up-front cost of creation of the front end and backend system but also ongoing maintenance of the solution and new workstreams to process a new channel of citizen engagement.

For this use-case, no relevant case study has been identified due to the horizon 3 level.

Case 4: Citizen sentiment mapping

"Digital city" (citiverse) technologies, including artificial intelligence and digital twins, can be used to collect and analyze the sentiments of city residents, enabling authorities to make informed decisions that take public opinion into account. AI algorithms are capable of processing this data to identify patterns, trends, and emerging issues, which are then visualized within dynamic models of the city.

Results

1) Resource Allocation: Using real-time data on public sentiment allows city authorities to prioritize the allocation of resources toward the neighborhoods or issues that are of greatest concern.

2) Quality of Life: Visualizing trends in public sentiment helps identify areas characterized by social tension, dissatisfaction, or unmet needs.

3) Effective Policymaking: Integrating the results of public sentiment analysis enables decision-making based on empirical data, citizens' preferences, and their current priorities.

4) Improvement of Urban Services: The feedback mechanism created by mapping public sentiment facilitates the continuous improvement of municipal services. By identifying the strengths and weaknesses of city services – from the perspective of the citizens themselves – authorities can adjust and refine their operations to better align with the public's expectations.

5) Citizen Engagement: Interactive visualization tools allow residents to see how their feedback influences the actions and policies of city authorities.

Key technologies: Digital twin, AR & VR, AI, GenAI, IoT.

Implemented in: Helsinki, Finland; New York, USA: Barcelona, Spain; Singapore; London, UK; Dublin, Republic of Ireland; Tallinn, Finland; Aachen; Germany Leicester, UK.

Case study: Citizen sentiment mapping and engagement platform in Patras, Greece

The city of Patras – Greece’s third-largest urban center and the administrative capital of the Western Greece region – has emerged as a leading example of integrating public opinion analysis tools into municipal governance through "digital twin" technology.

Home to approximately 214,000 residents, Patras faces challenges typical of mid-sized European cities: aging infrastructure, the need for environmental monitoring, complex traffic management issues, and an urgent requirement for meaningful citizen participation in decision-making processes. In 2020, building on experience gained through the EU’s "Intelligent Cities Challenge," the municipality of Patras began developing an "Urban Resilience Digital Twin." This solution fundamentally transforms how public opinion is gathered, analyzed, and incorporated into urban planning and the delivery of municipal services. The project represents a significant advancement over traditional management methods: it creates a dynamic, AI-driven digital model that continuously "learns" from interactions with citizens, providing real-time data on the needs and priorities of the local community.

The "Urban Resilience Digital Twin" project in Patras was aimed at transforming the city's governance system. At its core is a comprehensive, AI-driven platform that continuously collects, analyzes, and visualizes public sentiment, enabling data-informed decision-making and enhancing urban resilience. The primary objective was to create a dynamic system capable of converting fragmented citizen feedback into actionable insights for municipal authorities, facilitating a shift from reactive to proactive governance.

A key feature of the approach implemented in Patras is its granular, neighborhood-level focus. This allows city officials to understand how residents in different parts of the city perceive the quality of urban services and to identify localized issues that might otherwise go unnoticed when assessing the situation on a city-wide scale. The system serves as a tool for urban planning rooted in the actual priorities of citizens, rather than in assumptions about the needs of the public.

To implement this solution, the project utilized Sense.City – a versatile digital tool for citizen engagement, developed and maintained by the University of Patras. Sense.City establishes a direct link between residents and municipal services; through an intuitive mobile or web application, citizens can report urban issues in real time. The platform collects georeferenced data on a wide range of concerns – from malfunctioning streetlights and damaged traffic signals to abandoned vehicles and various environmental issues. Users can attach photographs to their reports, and each submission is categorized to ensure more efficient processing. This data is further supplemented by information gathered from social media.

Citizens have access to a citywide portal that allows them to track reported issues, monitor the progress of their resolution, and evaluate the performance of various municipal services. Municipal authorities use analytical dashboards that display trends in the emergence of issues, response times, and metrics regarding successful resolution.

To process and analyze citizen reports, the platform in Patras leverages the capabilities of modern smartphones – such as GPS, accelerometers, cameras, and microphones – effectively turning residents into "live sensors" of the urban environment. The system's backend manages data related to geofencing and critical infrastructure, providing municipal officials with a comprehensive overview of urban issues. The platform is open-source, which facilitates its adaptation and implementation in other cities worldwide; furthermore, it includes an open API for integration with other urban management systems.

Integrating real-time feedback from citizens with predictive analytics methods opens up significant opportunities for the proactive management of the urban environment, making it possible to address issues before they escalate into large-scale systemic failures.

Case 5: Virtual town halls

Virtual public meetings, based on metaverse and extended reality (XR) technologies, offer an innovative way for citizens to engage with local government authorities and community leaders. Such events create an immersive 3D environment where residents can participate in open discussions, ask questions, and share their opinions in real time – regardless of their physical location.

Key technologies: Metaverse, VR, AI, GenAI. Implemented in Seoul, Republic of Korea. Seoul's Metaverse Seoul initiative exemplifies how metaverse technology can be effectively utilized to enhance public service delivery and citizen engagement. By creating

an immersive and interactive virtual environment, the Seoul Metropolitan Government has paved the way for innovative digital governance, setting a benchmark for other cities to follow.

Case 6: Civil servant onboarding and training

Creating immersive learning environments allows new employees to interact with digital replicas of government buildings, enabling them to familiarize themselves with the work environment, internal policies, and procedures within a safe, virtual setting. In a space reminiscent of a metaverse, new hires can simulate real-world work scenarios – such as processing citizen inquiries, responding to emergencies, or collaborating with colleagues from other departments. AI-powered virtual assistants can guide employees through the training process, offering personalized learning paths and assessing their knowledge. This approach not only accelerates onboarding but also facilitates better information retention, boosts employee engagement, and enhances preparedness for job responsibilities, ultimately helping civil servants integrate into the workflow more effectively.

Key technologies: Metaverse platforms, VR, GenAI, Digital twins. Implemented in: San Diego County, USA; Sharjah, UAE; Dubai, UAE.

San Diego County determined that new staff members require more hands-on experience to conduct eligibility interviews and make informed decisions regarding the provision of benefits – decisions that determine families' access to food, healthcare, and housing support.

San Diego County, in collaboration with Accenture, has implemented the Accenture Virtual Experience Solution (AVEnueS) – a comprehensive VR training platform designed specifically for the needs of the public sector.

By leveraging immersive technologies and AI-driven interactive elements, the program has successfully addressed key challenges inherent in traditional training methods, while simultaneously enhancing staff readiness and the quality of services provided. As digital tools become increasingly accessible and sophisticated, this model offers a scalable framework for modernizing workforce development within the public sector across various jurisdictions and service areas.

Case 7: Immersive library and community services

The metaverse and XR have the potential to transform the delivery of library services by creating virtual libraries and public spaces. Libraries can develop immersive environments where users can explore various genres, attend author meet-and-greets, or join book clubs – all within a fully interactive setting. Through XR technologies, users can also engage with digital versions of books, interacting with multimedia content such as videos, audio, or interactive exhibits. Artificial intelligence can be integrated to provide personalized recommendations and support virtual librarians, who can guide users in navigating and utilizing resources. Furthermore, libraries can host virtual or XR-based educational sessions, facilitating easier access to workshops, research activities, and even remote study groups.

Key technologies: Digital twin, Metaverse, AR, VR, GenAI, IoT. For this use-case, no relevant case study has been identified due to the horizon 3 level.

Case 8: Interactive community support programmes

Virtual world technologies – including metaverses, combined with AI-powered chatbots and immersive environments – have the potential to transform community support programs by offering residents interactive and accessible platforms through which they can obtain assistance, guidance, and resources.

Key technologies: Metaverse, AR, VR, MR, GenAI, AI. Implemented in: Westminster, UK; Seoul, Republic of Korea; Manchester, UK.

Westminster Council, operating within one of London's most diverse and complex urban environments, has faced significant challenges in providing support to communities affected by youth violence. Traditional community engagement programs often failed to reach the most hard-to-engage groups of residents. High levels of youth violence, combined with low levels of trust between citizens and local authorities, created obstacles to the effective implementation of support measures. Community practitioners in Westminster concluded that innovative approaches were required – ones that could foster meaningful connections and deliver psychological support in a way that was both accessible and truly relevant to the affected populations.

Westminster Council partnered with The FRED Company to implement a comprehensive three-year programme (2021-2023) spanning eight distinct projects, each running 6-12 weeks.

The VR-RAW program, implemented in Westminster, demonstrates the significant potential of immersive technologies to transform public support systems – particularly for hard-to-reach populations facing social challenges. The success of this initiative led to the establishment of the Westminster VR Service, which has facilitated the broader integration of virtual reality technologies into public support strategies. This example illustrates how the thoughtful application of advanced technology can open new avenues for strengthening social ties, supporting mental health, and fostering social cohesion within complex urban environments.

Case 9: Immersive city service delivery

Creating virtual spaces and experiences that digitally recreate the real world will allow citizens to interact more freely with the government and members of their communities – leveraging technologies such as the metaverse, augmented/mixed/virtual reality, and blockchain – to submit applications and access comprehensive services and benefits. Government services, including permit applications, the receipt of benefits, and non-emergency services, can be delivered through these environments.

Key technologies: Metaverse, AR, VR, MR, GenAI/AI, IoT. Implemented in Seoul, Republic of Korea.

The Seoul Metropolitan Government serves approximately 10 million people within a complex urban environment, a task that entails thousands of daily administrative operations – ranging from processing permit applications to managing social welfare assistance. Traditional service centers face several challenges, including limited capacity, long wait times, and accessibility issues – particularly for the elderly, individuals with disabilities, and those who work shifts.

In November 2022, Seoul launched "Metaverse Seoul" – the world's first government-run metaverse – designed to transition municipal administrative functions, public consultations, and economic services into a digital format, delivered through an immersive 3D environment.

The Seoul Metropolitan Government, in partnership with leading technology companies, launched a phased pilot project involving 3,200 users, including municipal employees, youth groups, and governance experts. Key elements included:

• Virtual City Hall and Plazas: 3D reconstructions of Seoul City Hall and Gwanghwamun Plaza, recreated within the metaverse, allowing users to navigate to information points via avatars.

• Integrati n of AI-powered chatbots and the "Seoul Wallet" service.

• C nsultation rooms for young people.

• Blockchain-based identification and documentation: Distributed ledger technology serves as the foundation for user authentication and the issuance of digital certificates, minimizing fraud and streamlining record-keeping.

• Metaverse Startup Zone: A dedicated area featuring virtual booths for fintech startups and small-to-medium-sized enterprises, enabling them to present projects to investors, attend workshops, and conduct real-time product demonstrations.

Results

• Service Usage: 85% of pilot project participants completed at least one municipal transaction (such as renewing a permit or applying for social assistance) via the metaverse platform.

• Engagement: Attendance at virtual city meetings was twice as high as that of comparable in-person events; furthermore, 78% of participants actively took part in real-time polls and Q&A sessions.

• Operational Efficiency: AI-powered chatbots handled 72% of standard inquiries, reducing the workload on staff (operators) by an average of 55%.

• Economic Impact: Over 150 virtual startup pitches attracted the interest of 20 international investors, leading to the initiation of funding negotiations totaling approximately 2 million USD.

• User Satisfaction: Pilot project participants rated their experience 4.6 out of 5, highlighting convenience and reduced wait times as the primary benefits.

The Metaverse Seoul project demonstrates that immersive virtual platforms can significantly enhance the delivery of municipal services, civic engagement, and local economic development. Seoul has created a scalable model for other cities looking to modernize their public services. Future plans include deepening integration with smart city IoT networks, launching multilingual virtual support services, and incorporating environmental monitoring data to bolster sustainability initiatives.

Case 10: Urban air quality monitoring

Cities are increasingly adopting "digital twin" technologies to visualize and monitor air pollution in real time. By integrating data from IoT sensor networks, meteorological information, and details on traffic flow and land use into a unified 3D model, stakeholders can identify pollution hotspots, evaluate the effectiveness of implemented measures, and engage the public in initiatives to improve air quality. Machine learning algorithms make it

possible to forecast the dispersion of pollutants under various weather conditions and traffic intensity levels, while generative artificial intelligence enables users to query the data using natural language.

Key technologies: Digital twin, Mixed reality (MR), AI, GenAI, IoT. Implemented in: Jakarta, Indonesia; Shenzhen, China; London, UK.

Rapid urbanization and an increasing number of vehicles in Jakarta have led to a serious air pollution problem. The city is home to over 11.6 million people. According to research, air pollution in Jakarta causes more than 10,000 deaths and 5,000 hospitalizations annually due to cardiovascular and respiratory diseases, in addition to resulting in over 7,000 adverse health outcomes for children. The economic damage from this exceeds 2.9 billion USD per year (equivalent to 2.2% of Jakarta's gross regional product).

Traditional air quality monitoring relies on a limited network of stationary observation stations. Such a system fails to track local fluctuations in pollution levels across specific neighborhoods or short-term emission spikes near busy thoroughfares, making it difficult to develop effective interventions tailored to particular urban areas.

An initiative by BINUS University aims to overcome the primary shortcomings of traditional air quality monitoring in Jakarta by creating a "digital twin" (DT) of the city, integrated with mixed reality (MR) technologies.

The project's key objectives are to:

• D velop a comprehensive, data-rich 3D model of Jakarta's urban environment.

• Incorporate real-time data from air quality sensors, meteorological information, traffic flow data, and infrastructure characteristics into this virtual model.

• Enable decision-makers and stakeholders to visualize air pollution within a spatiotemporal context, identify "hotspots," and test various intervention measures within an interactive, immersive environment.

• Increase the transparency of processes, foster public engagement, and ensure support for science-based urban policy aimed at sustainable development and the protection of public health.

Results

The digital twin prototype provided city authorities and stakeholders with a comprehensive, real-time view of air quality in Jakarta. Key initial outcomes include:

• Precise identification of persistent pollution hotspots in densely built-up urban areas and near major transport hubs, enabling the prioritization of interventions.

• Robust scenario-modeling capabilities, demonstrating the potential impact of changes in transport policy, industrial restrictions, or the creation of new green spaces on local air quality.

• More effective decision-making: data visualization supported the allocation of resources for pollution control, the planning of traffic management measures, and the development of targeted public health recommendations.

• Engagement with a diverse range of stakeholders, which fostered greater transparency and strengthened trust in the city government's efforts to manage air quality.

The "digital twin" air quality system developed by BINUS University represents a significant advancement in the toolkit for environmental management in Jakarta. By integrating real-time sensor data, AI-driven analytics, immersive 3D visualization, and user interaction mechanisms powered by mixed reality (MR) technology, this project demonstrates how cities can develop adaptive, data-informed strategies to address complex urban challenges – such as air pollution. This approach serves as a replicable model for other megacities seeking to improve environmental conditions, bolster public health, and enhance stakeholder engagement in the governance of "smart" cities.

Conclusion

The concept of a "citiverse" – an urban ecosystem powered by artificial intelligence – should not be viewed as a single technological platform, but rather as a long-term development trajectory for cities. It serves as a framework for enhancing urban management, planning, operations, and civic engagement. The true value of this approach lies not in the mere accumulation of digital tools, but in the opportunities they create to deliver outcomes that are meaningful to residents.

A governance transformation for impactful civic outcomes achieving real public value. Not a technology project.

The AI-enabled citiverse is the convergence of artificial intelligence, digital twins, spatial computing and immersive environments into a coherent, sovereign urban intelligence platform designed to serve human potential, not replace it. It is not a future scenario. It is an emerging reality. Cities that treat it as speculative will find themselves governing systems already shaped by others.

Before a city can meaningfully build, four foundations must be in place. These are non-negotiable prerequisites.

- Vision: A formally endorsed strategy with at least one use case.
- Governance: Legal review + ethical and AI governance principles formally adopted.
- Data oundation: A funded plan for data collection, storage, and city sovereignty.
- C alition: Named champions.

AI capabilities and spatial computing are advancing exponentially. The rules of the new digital urban economy are being written today by cities that act, not by cities that wait.

Abbreviations and acronyms

AI	Artificial intelligence
API	Application programming interface
AR	Augmented reality
BIM	Building information modelling
GenAI	Generative artificial intelligence
GPS	Global positioning system
ICT	Information and communication technology
IoT	Internet of Things
MR	Mixed reality
NIS2	EU Directive on Security of Network and Information Systems 2
ROI	Return on investment
SDG	Sustainable Development Goal
SSC	Smart sustainable city
VR	Virtual reality
XR	Extended reality

REFERENCES

[1] AI-Enabled Citiverse: Use Cases for Cities in the Age of AI. https://www.itu.int/epublications/en/publication/citiverse-use-case-taxonomy-global-insights-and-implementation-pathways

[2] City Administration, Services and Public Participation. https://www.itu.int/epublications/en/publication/citiverse-use-case-taxonomy-city-administration-services-and-public-participation

[3] Urban planning, place making and infrastructure. https://www.itu.int/epublications/en/publication/citiverse-use-case-taxonomy-urban-planning-placemaking-and-infrastructure

[4] Economic development, education and tourism. https://www.itu.int/epublications/en/publication/citiverse-use-case-taxonomy-economic-development-education-and-tourism

[5] Public safety, health and disaster resilience. https://www.itu.int/epublications/en/publication/citiverse-use-case-taxonomy-public-safety-health-and-disaster-resilience

[6] Transport and mobility. https://www.itu.int/epublications/en/publication/citiverse-use-case-taxonomy-transport-and-mobility/en